Fast aeroservoelastic models for load simulation

Linear wind turbine response model based on the BHawC code

Master's Thesis

Joana Cardiff Aleu

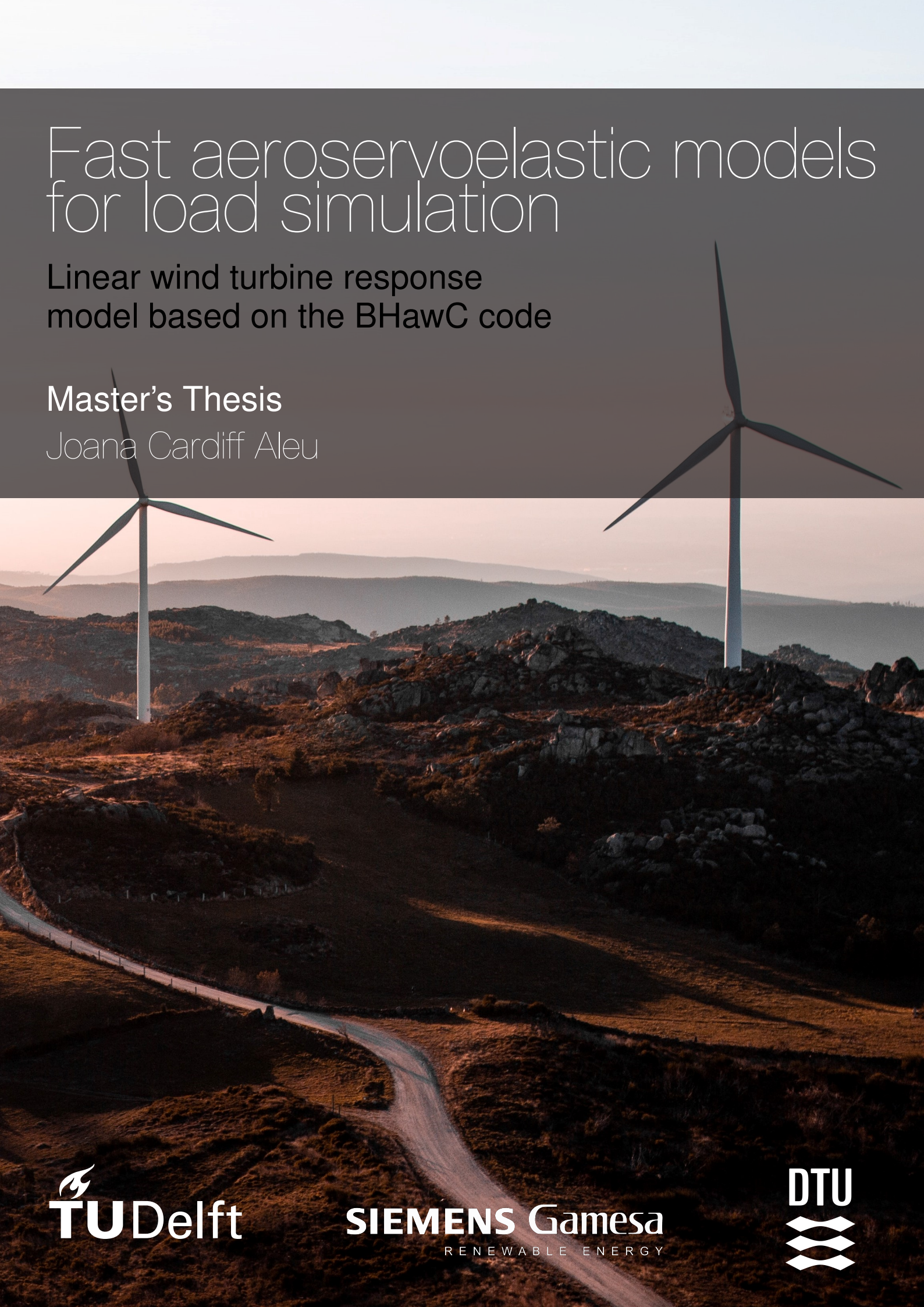

TU Delft

SIEMENS Gamesa RENEWABLE ENERGY

DTU

Fast aeroservoelastic models for load simulation

Linear wind turbine response model based on the BHawC code

by

Joana Cardiff Aleu

to obtain the degrees

Master of Science
in Aerospace Engineering
at Delft University of Technology

&

Master of Science
in European Wind Energy
at Technical University of Denmark

to be defended on 23rd August 2022

Thesis committee:	B. Giovanardi, Ph.D.		TU Delft
	R. Riva, Ph.D.		DTU
	P. F. Skjoldan, Ph.D.		SGRE
Master programme:	European Wind Energy Master		
Specialisation:	Rotor Design, Aerodynamics		
Institution:	TU Delft		DTU
Faculty:	Aerospace Engineering		Wind Energy
Student number:	5287464		s203259
Thesis project duration:	November 1st, 2021	until	July 31st, 2022

An electronic version of this thesis is available at https://repository.tudelft.nl/

Cover Image: Aerial photograph of wind turbines in Caramulinho (Portugal) by Afonso Coutinho.
Source: https://unsplash.com/photos/hdHy6055jAA

TU Delft

SIEMENS Gamesa
RENEWABLE ENERGY

DTU

Abstract

The design of wind turbines is an iterative process in which load calculations and system performance analyses are done under various environmental conditions. Due to the complexity of wind turbine systems, fully coupled aero-hydro-servo-elastic codes are indispensable to represent the nonlinear behaviour of the system. However, nonlinear codes are known to be costly and time-consuming. In consequence, fast methods of assessing the loads on the system are required to speed up the wind turbine design process, especially in its early stages. This research comprehends a linearised version of the BHawC model and provides fast methods of evaluating wind turbine loads under turbulent inflow conditions. For wind turbines in isotropic conditions and low turbulence intensity, the model is studied as a linear time-invariant (LTI) system through the Coleman transformation, which describes the rotor degrees of freedom in the inertial frame. The dynamic response of the system is obtained through a frequency-domain procedure based on computing the system's transfer function and using the fast Fourier transform (FFT) algorithm. In addition, model-order reduction (MOR) techniques are used to lower the run times of the simulations.

The verification of the fast model is accomplished by comparing the response of the linear model with that of the Siemens in-house aeroelastic simulation tool, BHawC. The comparison is made both in the time domain and the frequency domain through the power spectra of the time series. Results of the tower-top displacements and the tower-bottom loads are presented at three operating points. From the time-domain responses, the maximum root-mean-square error of the tower-base loads related to the fore-aft and the vertical motion of the turbine is around 10%. Besides, the tower-base lateral force and moment present large discrepancies of around 20% with respect to BHawC. The fatigue side-side moment is greatly overpredicted, whereas the differences for the other load channels are less than 20%.

For isotropic conditions and high turbulence intensity, the dependency on the variations in the controller is considered by modelling the system as a linear parameter-varying (LPV) system. In this case, a discrete-time approach is used together with model-order reduction techniques to reduce the computational requirements in terms of memory and run time. The methodology requires knowledge of the state at the steady-state equilibrium. Nevertheless, the linearised BHawC model describes the rotational degrees of freedom differently to the linearised model. Therefore, the implemented methodology is instead used in an analytical wind turbine model. There, the LPV system is able to capture the variability in the system while greatly reducing the computational expense of the simulations.

Preface

This thesis marks the end of my two-year education programme in the Rotor Design track as part of the European Wind Energy Master (EWEM). This programme has offered me the opportunity to study at two leading universities in the wind energy field, DTU (Denmark) and TU Delft (the Netherlands), together with the outcome of a double diploma in European Wind Energy and Aerospace Engineering. As a result, over the last two years, I have acquired a deep understanding of wind turbine technology and aerodynamics, which was only possible with the help of dedicated staff and professors from both institutions.

Embarking on this journey during the midst of a global pandemic was challenging. Nevertheless, being surrounded by smart, like-minded colleagues with a passion for this field has made every step of the way a memorable and unique experience. Most importantly, it has been a time of substantial personal growth, in which my friends and the EWEM cohort have been my home away from home -the many travels, parties, and long study hours will never be forgotten.

I would like to express my sincere gratitude to all thesis committee members. Riccardo, thank you very much for guiding this project and helping me develop my methodology. Your positive involvement and genuine feedback have been invaluable in keeping this project going. Bianca, thank you for your discussion and for providing ideas filled with enthusiasm and dynamism. Your help on this project is much appreciated. Peter, thank you for your patience and supervision during the project and for giving me a warm welcome into the SGRE team. It has been a remarkable opportunity to work with you. To all, our weekly meetings and your technical suggestions have helped steer this project. Finally, I would also like to extend my gratitude to Simon Watson, Xuerui Wang, and Carlo Tibaldi for taking part in the assessment committee and making of my defence a rewarding and enjoyable experience.

Finally, I would like to thank my family, Gordon, Menchu, and Jordi, for their constant support and encouragement throughout my thesis and my life as a whole. I feel blessed and honoured for the outstanding people who have always been here with me and those I have met along the way.

Joana Cardiff Aleu
Copenhagen, July 2022

Contents

List of Figures

List of Tables

Acronyms

BEM Blade Element Momentum.

BHawC Bonus Horizontal Axis Wind turbine simulation Code.

BT balanced truncation.

CT Continuous time.

DLL Dynamic Link Library.

DOF Degree of freedom.

DT Discrete time.

DTU Technical University of Denmark.

EMP Exponentially modulated periodic.

FEM Finite Element Method.

FFT fast Fourier transform.

FOM Full-order model.

HSV Hankel singular value.

IFFT inverse fast Fourier transform.

LPV Linear parameter-varying.

LTI Linear time-invariant.

LTP Linear time-periodic.

MBC Multi-Blade Coordinates.

MIMO Multiple-Input Multiple-Output.

MOR Model order reduction.

PCHIP piecewise cubic hermite interpolating polynomial.

PSD power spectral density.

RMSE root mean square error.

ROM Reduced-order model.

SGRE Siemens Gamesa Renewable Energy.

TU Delft Delft University of Technology.

ZOH Zero-order hold.

Nomenclature

Aerodynamic model

α	Angle of attack
$\mathbf{f}_{(\cdot),\text{aero}}$	Vector of aerodynamic forces and moments
$\mathbf{T}_{\text{AE}}$	Mapping between unit length loads at the aerodynamic sections and global loads at the structural nodes
$\mathbf{T}_{\text{A}}$	Aerodynamic section orientation matrix
$\mathbf{V}_0$	Free wind speed
$\mathbf{W}_{\text{A}}$	Relative inflow wind speed
C_d	Aerodynamic drag coefficient
C_l	Aerodynamic lift coefficient
C_m	Aerodynamic pitching moment coefficient
d	Drag force
l	Lift force
m_0	Aerodynamic pitching moment about the reference point
$m_{c/4}$	Quarter-chord aerodynamic pitching moment
p_n	Aerodynamic normal force
p_t	Aerodynamic tangential force
x_{ac}, y_{ac}	Distance to the aerodynamic center

Coordinate systems

$(\cdot)_A$	Local aerodynamic coordinate system
$(\cdot)_E$	Structural beam element coordinate system
$(\cdot)_G$	Global coordinate system
a_0, a_1, b_1	Multi-blade coordinates

BHawC wind turbine model

$\boldsymbol{\gamma}$	System response
$\boldsymbol{\nu}$	System inputs
$\boldsymbol{\rho}$	Nodal positions
$\boldsymbol{\theta}$	Nodal orientations
$\boldsymbol{\xi}$	Nodal degrees of freedom, generalized displacements
$\mathbf{C}$	Damping/gyroscopic matrix
$\mathbf{F}$	External forcing vector
$\mathbf{H}$	Relation between displacements and outputs
$\mathbf{K}$	Stiffness matrix
$\mathbf{M}$	Mass matrix
$\mathbf{q}$	Perturbation to the generalized displacements
$\mathbf{T}$	Substructure transformation matrix
$\mathbf{u}$	Perturbation to the inputs
$\mathbf{y}$	Perturbation to the outputs

Other symbols

Ω	Rotor speed
ω	Angular frequency
Ψ	Azimuth angle
$\mathbf{p}$	Scheduling parameter
f	Linear frequency
s	Laplace operator

T	Rotor period
t	Time
T_d	Discretisation time step

Model order reduction

$\boldsymbol{\sigma}$	Hankel Singular Values
$\mathbf{T}$	State transformation matrix of the balanced system
$\mathbf{V}, \mathbf{W}$	Projection matrices of the balanced truncation method
$\mathbf{W}_c, \mathbf{W}_o$	Controlability and observability Gramians
r	Order of the reduced-order model

State-space formulation

$\mathbf{A}$	State matrix
$\mathbf{B}$	Input matrix
$\mathbf{B}_\mathrm{q}$	Coleman transformation matrix
$\mathbf{C}$	Output matrix
$\mathbf{D}$	Feedforward matrix
$\mathbf{G}$	Transfer function
$\mathbf{I}$	Identity matrix
$\mathbf{u}$	Inputs
$\mathbf{x}$	State variables
$\mathbf{y}$	Outputs
n	Number of states, order of the full state-space model
n_i	Number of inputs
n_o	Number of outputs

Structural model

$(\cdot)_\mathrm{eq}$	Equilibrium format
$(\cdot)_\mathrm{f}$	Full format
ℓ_0	Beam element length
$\mathbf{f}_\mathrm{E,int}$	Internal structural loads
$\mathbf{K}_\mathrm{E,const}$	Constitutive stiffness matrix
$\mathbf{K}_\mathrm{E,geom}$	Geometric stiffness matrix
$\mathbf{S}$	Transformation matrix between full and equilibrium format
$\mathbf{T}_\mathrm{E}$	Element orientation matrix
f	Structural nodal force
m	Structural nodal moment

1 Introduction

The wind is an essential source of power that has been used throughout several millennia. Among the first applications are using sails to propel ships and building wind-powered machines to grind grain and pump water [23]. In the nineteenth century, windmills started to be used to extract energy from the wind. However, they became of little interest with the arrival of the First Industrial Revolution and the introduction of fossil fuels, which allowed for an efficient way to generate energy on a large scale. This was until the early 1970s, when the oil crisis triggered the funding of research programmes and the development of renewable energy sources [23].

Since then, the growing threats of global warming and climate change and the rising energy demand have led to a transition away from fossil fuels and towards renewable forms of energy: wind, solar, geothermal, and hydroelectric. Following the first developments in the 1980s, the evolution of wind turbine technology has seen a rapid growth —the rated output power of modern wind turbines has increased from roughly 50kW to today's over 10MW [29]. As a result, wind turbines have proven to be a mature technology for generating electricity from renewable sources. Nevertheless, there is an ongoing effort to minimize their cost of energy, achieved through increasing the efficiency of the rotor, reducing drive train losses, and developing more intelligent controllers, among others.

The design of wind turbines is a multidisciplinary optimization process, meaning each possible combination of design variables makes a potential design [26]. To evaluate the loads on the system, each candidate design has to be simulated under a wide range of environmental conditions. These simulations are usually performed using time-domain numerical tools [20], which allow to model the physical phenomena of wind turbines and also capture their nonlinear behaviour. While detailed aero-servo-elastic simulation codes are available, their accuracy comes at the expense of high computational costs. Therefore, methods to quickly evaluate the loads on wind turbines while maintaining a high enough level of fidelity are of interest. The early stages of wind turbine design are those that can particularly benefit from a reduction in the computational effort of these analyses. Subsequently, more refined and advanced models must be used for a complete design load basis evaluation in the mature design and certification stages.

This research is thus aimed at reducing the computational expense of load prediction, bringing down the time required for the conceptual stage of wind turbine design. On that account, the primary goal of this project is to develop and explore the performance of fast linear state-space models for wind turbines operating in isotropic environmental (wind) conditions. The performance of the models is determined based on the accuracy with which loads are predicted with respect to those obtained from BHawC, the full aero-servo-elastic load simulator from Siemens Gamesa Renewable Energy (SGRE).

1.1. Structure of the report

The report is structured as follows:

First, Chapter 2 reviews the existing literature, specifically on methods of evaluating the wind turbine loads using linear models. Also, the underlying theory used throughout this work is touched upon, including theoretical background on state-space models, linear time-invariant (LTI) systems, linear parameter-varying (LPV) systems, and linear time-periodic (LTP) systems. Besides, the research questions and objectives are formulated. Second, Chapter 3 describes the wind turbine models used throughout this project: the analytical wind turbine developed by Riva et al. [24] and BHawC, the nonlinear aero-servo-elastic wind turbine model from SGRE. Next, Chapter 4 explains the derivation of the state-space matrices of the developed linear model and depicts its state-space representation. The model order reduction (MOR) methods used to reduce the complexity of the system are also described. Then, Chapter 5 addresses the scenario in which the wind turbine is an isotropic system subject to a low turbulence wind inflow. In such conditions, the system is modelled as a linear time-invariant (LTI) system. It also presents the frequency-domain approach used to obtain the system's response as well as some applications of the method. Moreover, Chapter 6 explains the time-domain approach used to get the response of the isotropic wind turbine subject to a high turbulence wind inflow, where the system is modelled as a linear parameter-varying (LPV) system. For both study cases, the response of the linear model is validated against the nonlinear BHawC model. Finally, the conclusions and recommendations for future work are discussed in Chapter 7.

2

Theory, methods, and research questions

This chapter focuses on reviewing the existing literature (Section 2.1) to understand the motive behind the research questions and the objectives of this work, which are stated in Section 2.3. In addition, Section 2.2 presents the theoretical background of the research project.

2.1. Literature review

Wind turbines are complex, nonlinear systems. In their design process, nonlinear time-domain analysis tools are necessary to evaluate the loads on the system. The disadvantage of these load estimation methods is that they require long computational times to perform the simulations. Therefore, developing fast models for load evaluation in the preliminary design stages is an ongoing research topic.

Shortening the necessary simulation times becomes central for offshore wind applications, where the hydrodynamic loads must also be considered for various sea states. Specifically, if the wind turbine under consideration is a floating wind turbine, the different floater designs must also be studied. In that case, the hydrodynamic and mooring loads must be included in the analysis, leading to more computationally expensive time-domain simulations. As part of the WEIS toolset, NREL [2, 11] developed RAFT, a frequency-domain tool that provides quick computations of floating wind turbines. The model accounts for aerodynamics on the blades and structure, hydrodynamic loads acting on the platform, quasi-static loads on the mooring system, and includes a linearised controller. On the other hand, to improve the early design stages, Pegalajar-Jurado et al. [20] introduced QuLAF, a tool to quickly evaluate the loads on floating wind turbines and hence, establish the conceptual floater design. It uses a linear, frequency-domain model with four planar degrees of freedom and gets the aerodynamic, hydrodynamic, and mooring loads from state-of-the-art tools [16]. Despite being a simplified model, it predicts the loads and response of floating offshore wind turbines with reasonable accuracy.

Tibaldi et al. [26] presented a fast method of evaluating the fatigue loads on wind turbines, which uses a high-order linear aero-servo-elastic model to compute the frequency-domain response of a wind turbine system in turbulent wind. Then, it uses a spectral method from the power spectral density of the responses of several load sensors to predict the fatigue loads and damage [26]. The analysis assumes isotropic conditions in which gravity, wind shear and tower shadow are not considered. However, gravity effects can be modelled as deterministic contributions when evaluating the blade edgewise loads [26]. Also, to include the controller dependency, the open-loop matrices are exported, the controller modelled, and the closed-loop transfer function computed. This leads to good results for operating conditions with low turbulence intensity. However, if the turbulence is high, the variability of the con-

troller is not fully addressed, and the predicted loads lose continuity around the rated wind speed.

Furthermore, the motion of the tower-nacelle subsystem in a wind turbine is coupled to the motion of the rotor subsystem. While the dynamics of wind turbine blades are commonly expressed in the blade-fixed (or rotating) reference frame, the tower's motion is represented in the ground-fixed (non-rotating) coordinate system. Therefore, describing the rotor degrees of freedom in the ground-fixed frame is often interesting. This can be achieved through the Coleman transformation (also called the multi-blade coordinate transformation, MBC), which was first presented in the helicopter field by Coleman [51]. Then, due to its benefits, it started to receive the attention of the wind energy field, where Bir [37, 33] went on to develop the MBC3, a MATLAB®-based script to perform the Coleman transformation of the system matrices for three-bladed WTs. It has since been studied in detail by, amongst others, Skjoldan [32] during his thesis project, which introduces a modal analysis tool based on the BHawC aero-servo-elastic load simulation code. The results from the latter's work showed that any isotropic wind turbine system can be transformed into a time-invariant system through the Coleman transformation as the periodic coefficients are eliminated in the equations of motion, leading to a set of equations of motion with constant coefficients.

Anisotropic conditions can be caused either by (a) rotor anisotropy due to blade-to-blade manufacturing variations, pitch misalignment, and material accumulation on the blades, or (b) anisotropic environmental conditions, which arise from gravitational forces or wind flow asymmetry. Under such conditions, wind turbines must be modelled as linear time-periodic (LTP) systems. The work of Allen et al. [30] presents a system identification methodology for linear time-periodic systems where the input forces are unmeasured and random. It extends the operational modal analysis to LTP systems and accordingly, applies the harmonic transfer function to create an output-only system identification method. Wereley and Hall [45, 46] introduce the concept of the harmonic transfer function (HTF) as an extension of the frequency transfer function for LTP systems. Hence, the HTF describes the input-output relationship of linear time-periodic systems. Bringing together the many contributions regarding LTP systems done over the years, Bittanti and Colaneri [36] provide the theoretical framework for analysing, modelling, filtering and controlling periodically-varying systems. Furthermore, Skjoldan [32] uses the implicit Floquet analysis approach to provide the modal decomposition of a wind turbine in anisotropic conditions.

The present study builds on the linearised version of the BHawC model developed by Skjoldan [32] to provide the loads on a wind turbine given a turbulent wind input. The solution space between the fast linear model and the nonlinear aero-servo-elastic model is explored. The work is in line with the work of Tibaldi et al. [26] but expands it to study wind turbines in isotropic environmental conditions with both low and high turbulence. For wind turbines in isotropic conditions and low turbulence intensity, the system is treated as a linear time-invariant (LTI) system through the Coleman transformation, which allows for frequency-domain analysis of the system. For isotropic conditions and high turbulence intensity, the dependency on the variations in the controller is accounted for by exporting the matrices for several wind speeds and creating a linear parameter-varying (LPV) system. The dynamical response of the wind turbine system is studied in the discrete-time domain.

2.2. Theoretical background

This section contains the theoretical background of the research project. Particularly, an overview of the different types of state-space models is given based on their time-dependency. First, Section 2.2.1 gives a general introduction to the state-space representation of linear models, while Section 2.2.2 presents the theory behind linear time-invariant (LTI) systems. Then, Sections 2.2.3 to 2.2.4 give insight into linear parameter-varying (LPV) systems and their conversion from the continuous-time domain to their discrete-time formulations. Last, Section 2.2.5 introduce the concept of linear time-periodic (LTP) systems.

2.2.1. State-space models

Expressing complex physical systems through differential equations can become cumbersome, especially if the system is a multiple-input multiple-output (MIMO) system. Therefore, state-space models are often used, as they replace the nth-order differential equations with first-order differential equations [31] to describe the system's dynamics.

First, the general structure of an nth-order state-space model is expressed through two equations as:

$$\dot{\boldsymbol{\xi}}(t) = \boldsymbol{f}\left(\boldsymbol{\xi}(t), \boldsymbol{\nu}(t), t\right) \quad \text{(state evolution equation)} \tag{2.1a}$$

$$\boldsymbol{\gamma}(t) = \boldsymbol{g}\left(\boldsymbol{\xi}(t), \boldsymbol{\nu}(t), t\right) \quad \text{(instantaneous output equation)} \tag{2.1b}$$

where the n_i system inputs, n_o outputs, and n states are defined, respectively, as

$$\boldsymbol{\nu}(t) = \begin{bmatrix} \nu_1(t) \\ \vdots \\ \nu_{n_i}(t) \end{bmatrix}, \quad \boldsymbol{\gamma}(t) = \begin{bmatrix} \gamma_1(t) \\ \vdots \\ \gamma_{n_o}(t) \end{bmatrix}, \quad \boldsymbol{\xi}(t) = \begin{bmatrix} \xi_1(t) \\ \vdots \\ \xi_n(t) \end{bmatrix} \tag{2.2}$$

while for continuous-time (CT) systems, we interpret

$$\dot{\boldsymbol{\xi}}(t) = \frac{d\boldsymbol{\xi}(t)}{dt}, \quad t \in \mathbb{R} \text{ or } \mathbb{R}^+ \tag{2.3}$$

for discrete-time (DT) systems, the state update vector is

$$\dot{\boldsymbol{\xi}}(t) = \dot{\boldsymbol{\xi}}(t+1), \quad t \in \mathbb{Z} \text{ or } \mathbb{Z}^+. \tag{2.4}$$

Consequently, if the current state and input vector at a time t are known, the current output can be computed through Eq. (2.1b), and the following state (DT case) or the derivative of the state (CT case) can be obtained through Eq. (2.1a).

Linearisation

Much attention has been focused on *linear* models. In the study of dynamical systems, linear models arise as descriptions of small perturbations away from a nominal solution of the system (perturbation theory). Considering the general structure of a state-space model in Eq. (2.1), the equilibrium trajectory of the system (denoted as o) consists of $\tilde{\boldsymbol{\xi}}(t)$, $\tilde{\boldsymbol{\gamma}}(t)$, and $\tilde{\boldsymbol{\nu}}(t)$, which jointly satisfy the state-space equations [31].

Then, assume the input signal and the initial conditions are perturbed away from their nominal values by $\mathbf{u}(t) = \boldsymbol{\nu}(t) - \tilde{\boldsymbol{\nu}}(t)$ and $\mathbf{q}(0) = \boldsymbol{\xi}(0) - \tilde{\boldsymbol{\xi}}(0)$, respectively. In the same line, the state trajectory is perturbed by $\mathbf{q}(t) = \boldsymbol{\xi}(t) - \tilde{\boldsymbol{\xi}}(t)$, and similarly for the outputs $\mathbf{y}(t) = \boldsymbol{\gamma}(t) - \tilde{\boldsymbol{\gamma}}(t)$. Substituting these new values and performing a multivariable Taylor series expansion to first-order terms [31], the state-space equations read:

$$\dot{\mathbf{q}}(t) \approx \left[\frac{\partial \boldsymbol{f}}{\partial \boldsymbol{\xi}}\right]_o \mathbf{q}(t) + \left[\frac{\partial \boldsymbol{f}}{\partial \boldsymbol{\nu}}\right]_o \mathbf{u}(t) \tag{2.5a}$$

$$\mathbf{y}(t) \approx \left[\frac{\partial \boldsymbol{g}}{\partial \boldsymbol{\xi}}\right]_o \mathbf{q}(t) + \left[\frac{\partial \boldsymbol{g}}{\partial \boldsymbol{\nu}}\right]_o \mathbf{u}(t) \tag{2.5b}$$

where $\left[\partial \boldsymbol{f}/\partial \boldsymbol{\xi}\right]_o$ is the $n \times n$ Jacobian matrix of $\boldsymbol{f}$ with respect to $\boldsymbol{\xi}$ evaluated along the nominal solution, and similarly for the other Jacobian matrices defined in Eq. (2.5). Therefore, the state-space description of the linearised model can be rewritten in matrix form as:

$$\dot{\mathbf{q}}(t) = \mathbf{A}(t)\mathbf{q}(t) + \mathbf{B}(t)\mathbf{u}(t) \tag{2.6a}$$

$$\mathbf{y}(t) = \mathbf{C}(t)\mathbf{q}(t) + \mathbf{D}(t)\mathbf{u}(t) \tag{2.6b}$$

where the first equation, Eq. (2.6a), is known as the state equation, and the second equation, Eq. (2.6b), is called the output equation, and the tensors of rank 2 of the state-space model are defined as:

- $\mathbf{A}$ is the $n \times n$ state (or system) matrix,
- $\mathbf{B}$ is the $n \times n_i$ input matrix,
- $\mathbf{C}$ is the $n_o \times n$ output matrix, and
- $\mathbf{D}$ is the $n_o \times n_i$ feedforward (or feedthrough) matrix.

Physical dynamic systems

Generally, linear physical systems are modelled as second-order differential equations. In the case of structural dynamics, these describe the system's dynamics about the equilibrium configuration as:

$$\mathbf{M}(t)\ddot{\mathbf{q}}(t) + \mathbf{C}(t)\dot{\mathbf{q}}(t) + \mathbf{K}(t)\mathbf{q}(t) = \mathbf{F}(t)\mathbf{u}(t) \tag{2.7}$$

where $\mathbf{M}$, $\mathbf{C}$ and $\mathbf{K}$ are the mass, damping, and stiffness matrices, respectively, $\mathbf{q}$ is the vector of generalised displacements. The forcing matrix $\mathbf{F}$ is in charge of distributing the input $\mathbf{u}$ to the correct degrees of freedom.

Moreover, the measured output $\mathbf{y}$ is related to the displacements $\mathbf{q}$ by

$$\mathbf{y}(t) = \mathbf{H}(t)\mathbf{q}(t)\,. \tag{2.8}$$

The standard second-order form of the equations of motion in Eq. (2.7) can be described in the state-space formulation by rearranging the equations to form the $n \times 1$ state vector $\mathbf{x}$:

$$\mathbf{x} = \begin{bmatrix}\mathbf{q}^\top & \dot{\mathbf{q}}^\top\end{bmatrix}^\top, \quad \dot{\mathbf{x}} = \begin{bmatrix}\dot{\mathbf{q}}^\top & \ddot{\mathbf{q}}^\top\end{bmatrix}^\top \tag{2.9}$$

which leads to the following state-space representation:

$$\dot{\mathbf{x}}(t) = \mathbf{A}(t)\mathbf{x}(t) + \mathbf{B}(t)\mathbf{u}(t) \tag{2.10a}$$

$$\mathbf{y}(t) = \mathbf{C}(t)\mathbf{x}(t) + \mathbf{D}(t)\mathbf{u}(t) \tag{2.10b}$$

where the state, input, output, and feedback matrices are:

$$\mathbf{A} = \begin{bmatrix}\mathbf{0} & \mathbf{I} \\ -\mathbf{M}^{-1}\mathbf{K} & -\mathbf{M}^{-1}\mathbf{C}\end{bmatrix}, \quad \mathbf{B} = \begin{bmatrix}\mathbf{0} \\ \mathbf{M}^{-1}\mathbf{F}\end{bmatrix} \tag{2.11a}$$

$$\mathbf{C} = \begin{bmatrix}\mathbf{H} & \mathbf{0}\end{bmatrix}, \qquad \mathbf{D} = \mathbf{0}\,. \tag{2.11b}$$

and

- $\mathbf{x}$ is the $n \times 1$ state vector,
- $\mathbf{u}$ is the $n_i \times 1$ input vector, and
- $\mathbf{y}$ is the $n_o \times 1$ output vector.

Time dependency

If the original nonlinear model is time-invariant and the nominal solution is constant, the linearised model will also result in a time-invariant system [31]. Hence, the state-space model can be represented as a linear time-invariant (LTI) system, and its description is simplified to:

$$\dot{\mathbf{x}}(t) = \mathbf{A}\mathbf{x}(t) + \mathbf{B}\mathbf{u}(t) \tag{2.12a}$$

$$\mathbf{y}(t) = \mathbf{C}\mathbf{x}(t) + \mathbf{D}\mathbf{u}(t) \tag{2.12b}$$

where $\mathbf{A}$, $\mathbf{B}$, $\mathbf{C}$, and $\mathbf{D}$ are constant matrices.

Furthermore, the linearised model may be a linear time-varying (LTV) model if the nominal solution is time-varying, or a linear time-periodic (LTP) model if the nominal solution is periodic, which corresponds to a system operating in a cyclic or periodic steady-state. For LTP models, the matrices describing the state-space system have periodically varying coefficients as $\mathbf{A}(t) = \mathbf{A}(t+T)$, $\mathbf{B}(t) = \mathbf{B}(t+T)$, $\mathbf{C}(t) = \mathbf{C}(t+T)$, $\mathbf{D}(t) = \mathbf{D}(t+T)$, where T denotes the system's period. This is the case for wind turbine systems, where the set of equations of motion have periodic coefficients caused by the rotation of the rotor [32].

2.2.2. Linear time-invariant (LTI) models

As described above, linear time-invariant (LTI) systems can be described by linear differential equations with constant coefficients. Particularly, if the model is represented in the state-space form, the state and output equations are characterised by having constant matrices **A**, **B**, **C** and **D**, as seen above in Eq. (2.12b). For wind turbines, the steady-state is time-periodic due to the rotation of the rotor. To deal with such periodicity, wind turbine systems can be converted into time-invariant systems through a coordinate transformation, the a priori known Coleman or multi-blade coordinate (MBC) transformation.

Transfer function

The idea behind the transfer function comes from looking at the frequency response of a system [50]. For a linear system, the transfer function describes how an incoming signal is modified when going through a system. In other words, it depicts the input-output relation of the system. Hence, it is widely used to characterise the stability and performance of linear systems.

Taking the Laplace transform of the general state-space model under the assumption that all initial values are zero reads,

$$s\mathbf{X}(s) = \mathbf{A}\mathbf{X}(s) + \mathbf{B}\mathbf{U}(s) \tag{2.13a}$$

$$\mathbf{Y}(s) = \mathbf{C}\mathbf{X}(s) + \mathbf{D}\mathbf{U}(s) \tag{2.13b}$$

where the Laplace transform variable s is thought of as a complex frequency. When the transfer function is evaluated at $s = j\omega$ with $j := \sqrt{-1}$ being the imaginary unit, it is also known as the frequency response function of the system.

As the general form of the transfer function is the ratio of the output to the input, the above equations can be rewritten as:

$$\mathbf{X}(s) = (s\mathbf{I} - \mathbf{A})^{-1}\mathbf{B}\mathbf{U}(s) \tag{2.14}$$

which, substituting into the output equation, gives:

$$\mathbf{G}(s) = \mathbf{C}(s\mathbf{I} - \mathbf{A})^{-1}\mathbf{B} + \mathbf{D}\ . \tag{2.15}$$

The roots of the numerator and the denominator are the so-called zeros and poles of the system, respectively. The transfer function poles correspond to the eigenvalues of the system matrix **A**, meaning they only depend on the intrinsic dynamics of the system [50]. On the other hand, the zeros depend on how the inputs and outputs are coupled to the states and hence, they depend on matrices **A**, **B**, **C** and **D** of the state-space formulation.

Finally, the response or output of the model yields from joining the transfer function $\mathbf{G}(s)$ with the Laplace-transformed input $\mathbf{U}(s)$ as:

$$\mathbf{Y}(s) = \mathbf{G}(s)\mathbf{U}(s)\ . \tag{2.16}$$

Coleman transformation

The use of multi-blade coordinates (MBC) is a method of describing the motion of the rotor in the inertial frame of reference [24, 32]. For three-bladed isotropic wind turbines in isotropic external condi-

tions, this approach can be used to transform a time-periodic and, therefore, time-varying system into a time-invariant one. The transformation of the blade coordinates into the ground-fixed frame is done via the multi-blade coordinate transformation as:

$$a_0 = \frac{1}{3}\sum_{j=1}^{3}\xi_j\,, \quad a_1 = \frac{2}{3}\sum_{j=1}^{3}\cos(\psi_j)\xi_j\,, \quad b_1 = \frac{2}{3}\sum_{j=1}^{3}\sin(\psi_j)\xi_j \tag{2.17}$$

where $\psi_j = \psi_1 + 2\pi(j-1)/3$ is the azimuth angle for blade number j and ξ_j are a set of blade coordinate, and $\psi_1 = \Omega t$ with Ω being the rotational speed of the wind turbine rotor.

The new multi-blade coordinates a_0, a_1 and b_1, designate the collective, the cosine-cyclic mode, and the sine-cyclic modes, respectively. Together, these three modes couple the rotor to the rest of the turbine. For the flapwise degrees of freedom, a_0 is the rotor coning, and a_1 and b_1 are the rotor tilt and yaw, respectively. Whereas for the edgewise DOFs, a_0 represents the collective (or symmetric) deflections, and a_1 and b_1 are the horizontal and vertical motions, respectively.

The vector of new state variables ($\mathbf{x}_\mathrm{B}$) represented in the non-rotating frame is:

$$\mathbf{x} = \mathbf{B}_\mathrm{x}\mathbf{x}_\mathrm{B} \tag{2.18}$$

whereby the transformation assembled in matrix form is known as the *Coleman [51] transformation*, and reads [43]:

$$\mathbf{B}_\mathrm{x}(t) = \begin{bmatrix} 1 & \cos(\psi_1(t)) & \sin(\psi_1(t)) \\ 1 & \cos(\psi_2(t)) & \sin(\psi_2(t)) \\ 1 & \cos(\psi_3(t)) & \sin(\psi_3(t)) \end{bmatrix}. \tag{2.19}$$

Under the assumption of isotropic rotors in isotropic conditions, transforming the blade coordinates into MBCs eliminates the periodic terms in the governing equations [43]. Consequently, a wind turbine system in isotropic conditions can be modelled as a linear time-invariant (LTI) system.

2.2.3. Linear parameter-varying (LPV) models

Linear parameter-varying (LPV) systems are linear state-space models whose dynamics vary as a function of certain time-varying signals $\mathbf{p}$ [14]. Accordingly, the LPV representation allows to describe the nonstationary behaviour of nonlinear systems [8]. In general, the state-space representation of LPV models in the scheduling space reads:

$$\dot{\mathbf{x}}(t) = \mathbf{A}(\mathbf{p})\mathbf{x}(t) + \mathbf{B}(\mathbf{p})\mathbf{u}(t) \tag{2.20a}$$

$$\mathbf{y}(t) = \mathbf{C}(\mathbf{p})\mathbf{x}(t) + \mathbf{D}(\mathbf{p})\mathbf{u}(t) \tag{2.20b}$$

where $\dot{\mathbf{x}}(t)$ are the states, $\mathbf{u}(t)$ are the inputs, $\mathbf{y}(t)$ are the outputs, and the state-space matrices are parametrised by the scheduling parameters $\mathbf{p} = \mathbf{p}(t)$. Note that for discrete-time systems, the state update vector becomes $\mathbf{x}(t+T_\mathrm{d})$, where T_d is the sample time.

Grid-based representation

A typical representation of LPV systems is the so-called *grid-based representation*, which consists of a collection of system linearisations on a gridded domain of parameter values $\mathbf{p}$ [28]. First, a series of linear time-invariant (LTI) models are generated by evaluating the LPV model for several values of the scheduling parameter(s). Then, the system is stored as a finite state-space array defined on a gridded domain, in which each grid point corresponds to a local LTI model [14]. For example, Fig. 2.1 illustrates a grid-based LPV system that models a wind turbine system, where the time-varying parameters are the free wind speed and the rotor azimuthal position at a collection of operating points (OPs).

An extension of the LPV representation to account for offsets in the state vector, its derivate, and in the input and output vectors [14], is the *affine form* of the LPV model. These offsets correspond to the values at the operating points at which the model is linearised. On that account, the state-space set of

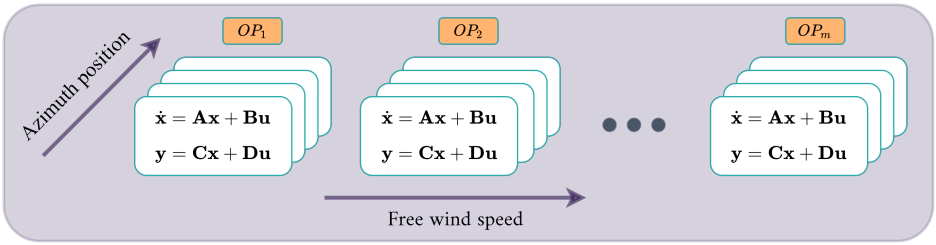

Figure 2.1: Wind turbine LPV model defined on a rectangular grid

equations is expressed in the continuous-time domain as:

$$\dot{\mathbf{x}}(t) = \mathbf{A}(\mathbf{p})\mathbf{x}(t) + \mathbf{B}(\mathbf{p})\mathbf{u}(t) - (\mathbf{A}(\mathbf{p})\tilde{\mathbf{x}}(\mathbf{p}) + \mathbf{B}(\mathbf{p})\tilde{\mathbf{u}}(\mathbf{p})) \tag{2.21a}$$

$$\mathbf{y}(t) = \mathbf{C}(\mathbf{p})\mathbf{x}(t) + \mathbf{D}(\mathbf{p})\mathbf{u}(t) - (\mathbf{C}(\mathbf{p})\tilde{\mathbf{x}}(\mathbf{p}) + \mathbf{D}(\mathbf{p})\tilde{\mathbf{u}}(\mathbf{p})) + \tilde{\mathbf{y}}(\mathbf{p}) \tag{2.21b}$$

and the linear model in the scheduling space in a compact formulation reads:

$$\dot{\hat{\mathbf{x}}}(t;\mathbf{p}) = \mathbf{A}(\mathbf{p})\hat{\mathbf{x}}(t;\mathbf{p}) + \mathbf{B}(\mathbf{p})\hat{\mathbf{u}}(t;\mathbf{p}) \tag{2.22a}$$

$$\hat{\mathbf{y}}(t;\mathbf{p}) = \mathbf{C}(\mathbf{p})\hat{\mathbf{x}}(t;\mathbf{p}) + \mathbf{D}(\mathbf{p})\hat{\mathbf{u}}(t;\mathbf{p}) \tag{2.22b}$$

where the state variables of the linear model are related to the states of the overall LPV model as $\hat{\mathbf{x}}(t;\mathbf{p}) = \mathbf{x}(t) - \tilde{\mathbf{x}}(\mathbf{p})$, and similarly for the state derivatives, inputs and outputs.

2.2.4. Discretisation of LPV models

Transforming the representation of a state-space system in continuous-time (CT) to the discrete-time (DT) domain is motivated by the simplification of its mathematical description. For discrete-time systems, the integrals of the continuous-time signals are replaced by summations, leading to faster algorithms with a lower computational expense. The state-space matrices must be discretised to convert the equations of a continuous-time system to their discrete-time formulation. In short, matrices ($\mathbf{A}$, $\mathbf{B}$, $\mathbf{C}$, $\mathbf{D}$) are converted to ($\mathbf{A}_\mathrm{d}$, $\mathbf{B}_\mathrm{d}$, $\mathbf{C}_\mathrm{d}$, $\mathbf{D}_\mathrm{d}$).

First, consider the general continuous-time state-space formulation of an LPV model with static scheduling dependence as:

$$\dot{\mathbf{x}}(t;\mathbf{p}) = \mathbf{A}(\mathbf{p})\mathbf{x}(t;\mathbf{p}) + \mathbf{B}(\mathbf{p})\mathbf{u}(t;\mathbf{p}) \tag{2.23a}$$

$$\mathbf{y}(t;\mathbf{p}) = \mathbf{C}(\mathbf{p})\mathbf{x}(t;\mathbf{p}) + \mathbf{D}(\mathbf{p})\mathbf{u}(t;\mathbf{p}) \tag{2.23b}$$

Using a zero-order hold (ZOH) setting, the DT signals can be obtained from the CT signals by assuming the latter remain constant inside each sampling interval [36], such that

$$\begin{aligned} \mathbf{u}(t) &= \mathbf{u}_\mathrm{d}(k)\,, \quad \forall t \in [kT_\mathrm{d}, (k+1)T_\mathrm{d}) \\ \mathbf{p}(t) &= \mathbf{p}_\mathrm{d}(k)\,, \quad \forall t \in [kT_\mathrm{d}, (k+1)T_\mathrm{d}) \\ \mathbf{y}_\mathrm{d}(k) &= \mathbf{y}(kT_\mathrm{d})\,. \end{aligned} \tag{2.24}$$

Then, the LPV state-space model can be described in discrete-time as the representation of an underlying sampled continuous-time LPV system [35]:

$$\mathbf{x}(k+1) = \mathbf{A}_\mathrm{d}(\mathbf{p}_\mathrm{d})\,\mathbf{x}_\mathrm{d}(k) + \mathbf{B}_\mathrm{d}(\mathbf{p}_\mathrm{d})\,\mathbf{u}_\mathrm{d}(k) \tag{2.25a}$$

$$\mathbf{y}(k) = \mathbf{C}_\mathrm{d}(\mathbf{p}_\mathrm{d})\,\mathbf{x}_\mathrm{d}(k) + \mathbf{D}_\mathrm{d}(\mathbf{p}_\mathrm{d})\,\mathbf{u}_\mathrm{d}(k) \tag{2.25b}$$

where the subscript "d" denotes the discrete-time (DT) domain, and the signals $\mathbf{u}_\mathrm{d}$ and $\mathbf{p}_\mathrm{d}$ are sampled signals of the input signal $\mathbf{u}$ and the scheduling signal $\mathbf{p}$, respectively, with a sampling period $T_\mathrm{d} > 0$.

Complete form

The complete signal evolution approach for the discretisation of LTI systems can be extended to LPV systems, where the state-space representation of the system becomes

$$\dot{\mathbf{x}}(t;\mathbf{p}) = \mathbf{A}(\mathbf{p}(kT_\mathrm{d}))\,\mathbf{x}(t) + \mathbf{B}(\mathbf{p}(kT_\mathrm{d}))\,\mathbf{u}(kT_\mathrm{d}) \tag{2.26a}$$

$$\mathbf{y}(t;\mathbf{p}) = \mathbf{C}(\mathbf{p}(kT_\mathrm{d}))\,\mathbf{x}(t) + \mathbf{D}(\mathbf{p}(kT_\mathrm{d}))\,\mathbf{u}(kT_\mathrm{d})\,. \tag{2.26b}$$

Given that the state evolution equation in Eq. (2.26a) is an Ordinary Differential Equation (ODE) and assuming the state matrix $\mathbf{A}$ is invertible, the solution is composed of a homogeneous solution and a forcing term. The DT state-space matrices of the complete method discretisation become [35]:

$$\mathbf{A}_\mathrm{d}(\mathbf{p}_\mathrm{d}(k)) = e^{\mathbf{A}(\mathbf{p}(kT_\mathrm{d}))T_\mathrm{d}} \tag{2.27a}$$

$$\mathbf{B}_\mathrm{d}(\mathbf{p}_\mathrm{d}(k)) = \mathbf{A}^{-1}(\mathbf{p}(kT_\mathrm{d}))\left(e^{\mathbf{A}(\mathbf{p}(kT_\mathrm{d}))T_\mathrm{d}} - \mathbf{I}\right)\mathbf{B}(\mathbf{p}(kT_\mathrm{d})) \tag{2.27b}$$

$$\mathbf{C}_\mathrm{d}(\mathbf{p}_\mathrm{d}(k)) = \mathbf{C}(\mathbf{p}(kT_\mathrm{d})) \tag{2.27c}$$

$$\mathbf{D}_\mathrm{d}(\mathbf{p}_\mathrm{d}(k)) = \mathbf{D}(\mathbf{p}(kT_\mathrm{d}))\,. \tag{2.27d}$$

As described by Tóth [35], the complete discretisation method contains a heavy nonlinear dependence on the scheduling parameter $\mathbf{p}_\mathrm{d}$. To deal with the nonlinearities whilst still representing the original behaviour of the system, approximative discretisation methods have been developed, containing a lower complexity of coefficient dependence. These methods approximate the integral that describes the state-evolution inside the sample interval by assuming a linear, polynomial, or rational dependence on $\mathbf{p}_\mathrm{d}$. Next, an overview of three approximate discretisation methods (the rectangular, polynomial and trapezoidal methods), is given.

Rectangular method

The rectangular (or Euler's forward) method applies a first-order approximation to the matrix exponential term, which becomes:

$$e^{T_\mathrm{d}\mathbf{A}(\mathbf{p}(kT_\mathrm{d}))} \approx \mathbf{I} + T_\mathrm{d}\mathbf{A}(\mathbf{p}(kT_\mathrm{d}))\,.$$

Substituting the conversion rule above into Eq. (2.27), the discrete-time system matrices of the rectangular discretisation approach are:

$$\mathbf{A}_\mathrm{d}(\mathbf{p}_\mathrm{d}(k)) = \mathbf{I} + T_\mathrm{d}\mathbf{A}(\mathbf{p}(kT_\mathrm{d})) \tag{2.28a}$$

$$\mathbf{B}_\mathrm{d}(\mathbf{p}_\mathrm{d}(k)) = T_\mathrm{d}\mathbf{B}(\mathbf{p}(kT_\mathrm{d})) \tag{2.28b}$$

$$\mathbf{C}_\mathrm{d}(\mathbf{p}_\mathrm{d}(k)) = \mathbf{C}(\mathbf{p}(kT_\mathrm{d})) \tag{2.28c}$$

$$\mathbf{D}_\mathrm{d}(\mathbf{p}_\mathrm{d}(k)) = \mathbf{D}(\mathbf{p}(kT_\mathrm{d}))\,. \tag{2.28d}$$

Polynomial method

The polynomial (or Hanselmann) discretisation method approximates the matrix exponential term through a higher-order Taylor expansion. Hence,

$$e^{\mathbf{A}(\mathbf{p}(kT_\mathrm{d}))T_\mathrm{d}} \approx \mathbf{I} + \sum_{l=1}^{n} \frac{T_\mathrm{d}^l}{l!}\mathbf{A}^l\left(\mathbf{p}(kT_\mathrm{d})\right)\,. \tag{2.29}$$

While it better approximates the complete method, it also introduces a higher complexity [35]. Then, substituting this approximation into Eq. (2.27), the DT system matrices of the polynomial discretisation method read:

$$\mathbf{A}_\mathrm{d}(\mathbf{p}_\mathrm{d}(k)) = \mathbf{I} + \sum_{l=1}^{n} \frac{T_\mathrm{d}^l}{l!}\mathbf{A}^l(\mathbf{p}(kT_\mathrm{d})) \tag{2.30a}$$

$$\mathbf{B}_\mathrm{d}(\mathbf{p}_\mathrm{d}(k)) = T_\mathrm{d}\left(\mathbf{I} + \sum_{l=1}^{n-1} \frac{T_\mathrm{d}^l}{l+1!}\mathbf{A}^l(\mathbf{p}(kT_\mathrm{d}))\right)\mathbf{B}(\mathbf{p}(kT_\mathrm{d})) \tag{2.30b}$$

$$\mathbf{C}_\mathrm{d}(\mathbf{p}_\mathrm{d}(k)) = \mathbf{C}(\mathbf{p}(kT_\mathrm{d})) \tag{2.30c}$$

$$\mathbf{D}_\mathrm{d}(\mathbf{p}_\mathrm{d}(k)) = \mathbf{D}(\mathbf{p}(kT_\mathrm{d}))\,. \tag{2.30d}$$

Trapezoidal method

The trapezoidal (or Tustin) method uses a trapezoidal evaluation of the state-evolution integral, providing a better approximation than the rectangular method [35]. The discretised matrices of the state-space formulation using the trapezoidal discretisation method are:

$$\mathbf{A}_\mathrm{d}(\mathbf{p}_\mathrm{d}(k)) = \left(\mathbf{I} + \frac{T_\mathrm{d}}{2}\mathbf{A}(\mathbf{p}(kT_\mathrm{d}))\right)\mathbf{E}^{-1} \tag{2.31a}$$

$$\mathbf{B}_\mathrm{d}(\mathbf{p}_\mathrm{d}(k)) = \sqrt{T_\mathrm{d}}\mathbf{E}^{-1}\mathbf{B}(\mathbf{p}(kT_\mathrm{d})) \tag{2.31b}$$

$$\mathbf{C}_\mathrm{d}(\mathbf{p}_\mathrm{d}(k)) = \sqrt{T_\mathrm{d}}\mathbf{C}(\mathbf{p}(kT_\mathrm{d}))\mathbf{E}^{-1} \tag{2.31c}$$

$$\mathbf{D}_\mathrm{d}(\mathbf{p}_\mathrm{d}(k)) = \frac{T_\mathrm{d}}{2}\mathbf{C}(\mathbf{p}(kT_\mathrm{d}))\mathbf{E}^{-1}\mathbf{B}(\mathbf{p}(kT_\mathrm{d})) + \mathbf{D}(\mathbf{p}(kT_\mathrm{d})) \tag{2.31d}$$

where, for simplicity, $\mathbf{E} = \mathbf{I} - \frac{T_\mathrm{d}}{2}\mathbf{A}(\mathbf{p}(kT_\mathrm{d}))$.

Furthermore, the grid-based representation of LPV systems in affine form can be combined with a discretised description of the system to account for the offsets in the inputs and state variables. In that case, the model can be evaluated in the discrete-time domain, where the state update vector and response of the system at each time are calculated as:

$$\mathbf{x}(k+1) = \mathbf{A}_\mathrm{d}(\mathbf{p}_\mathrm{d})\,(\mathbf{x}(k) - \tilde{\mathbf{x}}(\mathbf{p}_\mathrm{d})) + \mathbf{B}_\mathrm{d}(\mathbf{p}_\mathrm{d})\,(\mathbf{u}(k) - \tilde{\mathbf{u}}(\mathbf{p}_\mathrm{d})) + \tilde{\mathbf{x}}(\mathbf{p}_\mathrm{d}) \tag{2.32a}$$

$$\mathbf{y}(k) = \mathbf{C}_\mathrm{d}(\mathbf{p}_\mathrm{d})\,(\mathbf{x}(k) - \tilde{\mathbf{x}}(\mathbf{p}_\mathrm{d})) + \mathbf{D}_\mathrm{d}(\mathbf{p}_\mathrm{d})\,(\mathbf{u}(k) - \tilde{\mathbf{u}}(\mathbf{p}_\mathrm{d})) + \tilde{\mathbf{y}}(\mathbf{p}_\mathrm{d})\,. \tag{2.32b}$$

2.2.5. Linear time-periodic (LTP) models

To include the periodicity introduced in the wind turbine due to anisotropic conditions such as gravity forcing or wind shear and yaw, the system can be modelled as a linear time-periodic (LTP) system. First, recall that a linear time-periodic dynamical system can be described in the state-space form as [13]:

$$\dot{\mathbf{x}} = \mathbf{A}(t)\mathbf{x}(t) + \mathbf{B}(t)\mathbf{u}(t) \tag{2.33a}$$

$$\mathbf{y} = \mathbf{C}(t)\mathbf{x}(t) + \mathbf{D}(t)\mathbf{u}(t) \tag{2.33b}$$

where the periodicity of the system manifests itself in the periodicity of the matrices of the state-space model $\mathbf{A}(t+T) = \mathbf{A}(t)$, $\mathbf{B}(t+T) = \mathbf{B}(t)$, $\mathbf{C}(t+T) = \mathbf{C}(t)$, and $\mathbf{D}(t+T) = \mathbf{D}(t)$, being T the period of the system.

On the other hand, a generalisation of the class of T-periodic signals is the so-called exponentially modulated periodic (EMP) signal. Following the descriptions presented by both Bittanti and Colaneri [36] and Riva [36], "an LTP system of period T subject to an EMP input with period T admits an EMP regime with the same period". In such a regime, the state vectors can be expanded as EMP signals:

$$\mathbf{x}(t) = \sum_{n=-\infty}^{+\infty} \mathbf{x}_n e^{s_n t}, \quad \dot{\mathbf{x}}(t) = \sum_{n=-\infty}^{+\infty} s_n \mathbf{x}_n e^{s_n t}, \quad \mathbf{y}(t) = \sum_{n=-\infty}^{+\infty} \mathbf{y}_n e^{s_n t} \tag{2.34}$$

where $s_n = s + jn\Omega t$, being s a complex number.

Moreover, the state-space matrices of periodic coefficients can be expanded in Fourier series as:

$$\mathbf{A}(t) = \sum_{n=-\infty}^{+\infty} \mathbf{A}_n e^{jn\Omega t}, \text{ and similarly for } \mathbf{B}(t), \mathbf{C}(t) \text{ and } \mathbf{D}(t). \tag{2.35}$$

Subsequently, the harmonics of the vectors and the matrices can be assembled as doubly infinite vectors, and doubly infinite Toeplitz matrices [36] in the following fashion:

$$\begin{aligned} \boldsymbol{x} &= \left(\ldots, \mathbf{x}_{-1}^{\mathrm{T}}, \mathbf{x}_{0}^{\mathrm{T}}, \mathbf{x}_{+1}^{\mathrm{T}}, \ldots\right)^{\mathrm{T}}, \text{ and similarly with } \boldsymbol{u} \text{ and } \boldsymbol{y} \\ \mathcal{A} &= \begin{bmatrix} \ddots & \vdots & \vdots & \vdots & \iddots \\ \cdots & \mathbf{A}_0 & \mathbf{A}_{-1} & \mathbf{A}_{-2} & \cdots \\ \cdots & \mathbf{A}_1 & \mathbf{A}_0 & \mathbf{A}_{-1} & \cdots \\ \cdots & \mathbf{A}_2 & \mathbf{A}_1 & \mathbf{A}_0 & \cdots \\ \iddots & \vdots & \vdots & \vdots & \ddots \end{bmatrix}, \text{ and similarly with } \mathcal{B}, C \text{ and } \mathcal{D}. \end{aligned} \tag{2.36}$$

By substituting Eq. (2.36) into the state-space equations in Eq. (2.33), the system yields an infinite-dimensional system:

$$s\boldsymbol{x} = (\mathcal{A} - \mathcal{N})\boldsymbol{x} + \mathcal{B}\boldsymbol{u} \tag{2.37a}$$

$$\boldsymbol{y} = C\boldsymbol{x} + \mathcal{D}\boldsymbol{u} \tag{2.37b}$$

where $\mathcal{N} = \text{blkdiag}(jn\Omega\mathbf{I}, n \in \mathbb{Z})$ is a block diagonal matrix.

Harmonic transfer function

Similarly as for LTI models, the transfer function for linear time-periodic systems establishes the relationship between the inputs and outputs of a system. Accordingly, the harmonic transfer function $\mathcal{G}(s)$ yields from equating the state and output equations of the state-space formulation as [24]:

$$\mathcal{G}(s) = C(s\mathbf{I} - (\mathcal{A} - \mathcal{N}))^{-1}\mathcal{B} + \mathcal{D}. \tag{2.38}$$

For periodic systems, $\mathcal{G}(s)$ corresponds to an infinite-dimensional operator. The infinite-dimensional system can be replaced with a finite-dimensional approximation obtained by truncation of the Toeplitz matrices $\mathcal{A}$, $\mathcal{B}$, C and $\mathcal{D}$ [36], which helps reduce the computational time and the required resources.

2.3. Research questions

This section consists of two parts: formulating the main research question and the corresponding sub-questions into which it is split and presenting the research objective.

2.3.1. Research questions

From the preliminary literature review, the following main research question has been formulated:

> How does evaluating the design loads of a wind turbine in turbulent wind and isotropic conditions by using a linearised state-space response model affect the accuracy and computational expense of the simulations in comparison to the BHawC aero-servo-elastic load simulator?

The research question is decomposed into the sub-questions below, which answer the above high-level question.

Q1 How does modelling a wind turbine in isotropic environmental conditions with low turbulence

intensity as a frequency-domain linear time-invariant system perform compared to the BHawC simulations?

Q2 Can modelling a wind turbine in isotropic environmental conditions with high turbulence intensity as a linear parameter-varying system address the variability in the wind turbine operating region?

2.3.2. Research objective

On the other hand, the following main research objective of this thesis has been established:

> The purpose of this MSc. thesis project is to contribute to the reduction of the computational expense of the conceptual design phase of wind turbines by implementing a fast linear state-space response model based on the nonlinear aero-servo-elastic BHawC code to estimate the design loads of wind turbines in isotropic environmental conditions.

Similarly, the main research objective is divided into the two sub-goals below, each related to a task block (work package).

The equations of motion of a wind turbine in operating conditions are characterised as being time-periodic systems due to the rotation of the rotor [24]. Nevertheless, if the system is isotropic (isotropic rotor and isotropic environment conditions), the Coleman transformation can be used to remove the periodic content of the equations of motion. Hence, the system can be studied as an LTI system, which brings about the first research sub-goal:

- Estimate the design loads of a wind turbine in isotropic environmental conditions with low turbulence intensity by modelling the system as a linear time-invariant system based on the nonlinear BHawC code.

If, however, the wind turbine in isotropic conditions has a wind input with high turbulence intensity, the time-varying stochastic component of the wind will cause the controller to quickly shift between operating regions, mainly for wind speeds around rated. This time-varying behaviour cannot be modelled by using an LTI system; thus, to capture the variability of the control law, the system can be modelled as a linear parameter-varying system, which leads to the second sub-goal:

- Estimate the design loads of a wind turbine in isotropic environmental conditions with high turbulence intensity by modelling the system as a linear parameter-varying system based on the nonlinear BHawC code.

3

Wind turbine models

This chapter presents the wind turbine models used in this thesis. First, Section 3.1 explains the analytical wind turbine model used as a testbed for the implemented methods. Besides, Section 3.2 explains the fundamentals of the BHawC aeroelastic wind turbine simulation tool and describes its structural and aerodynamic models. Finally, Section 3.3 introduces the wind turbine model used for this work.

3.1. Analytical wind turbine model

The work in this thesis has been first verified with the simplified analytical model from Riva et al. [24], developed to study the periodic stability of wind turbines operating in turbulent wind conditions. This simple model helps test different solution methods with minimum implementation efforts and low computational time. The model represents an upwind, horizontal-axis wind turbine. By considering the coupled motion of the tower and blades subjected to aerodynamic forces, it accounts for the essential dynamics of a wind turbine. The motion of the tower and the blades is described by eight degrees of freedom (DOFs). Fig. 3.1 [24] displays a schema of the structural model of the analytical wind turbine model.

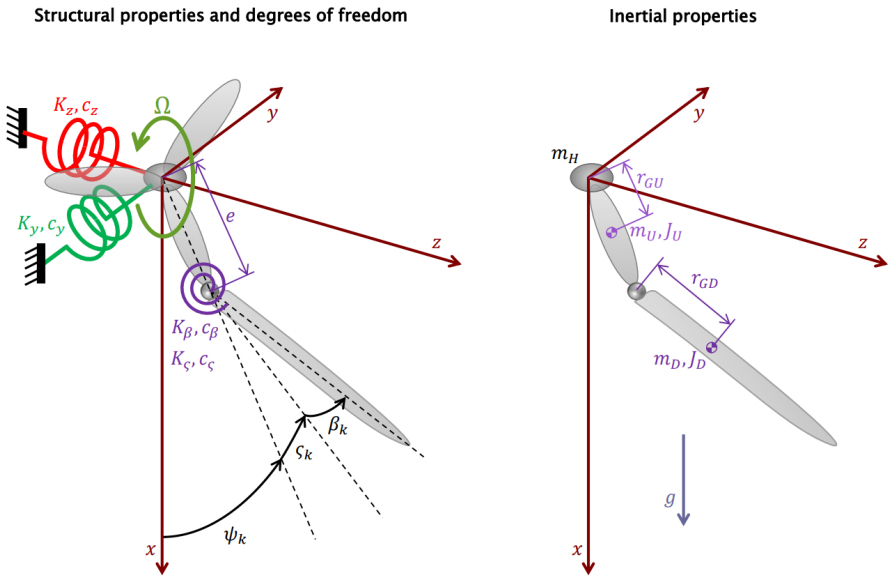

Figure 3.1: Sketch of the wind turbine analytical model with eight DOFs: tower-top fore-aft and side-side displacements, z_H and y_H, flapwise blade deflections β_1, β_2, and β_3, and edgewise blade deflections ζ_1,ζ_2, and ζ_3. From Riva et al. [24]

As seen, the hub can translate in the two horizontal directions, the fore-aft and side-side displacements. In addition, the motion of the blades is described by the in-plane and out-of-plane angles of the equivalent hinge [24].

The structural model represents the tower-top fore-aft and side-side flexibility using "two equivalent linear springs and dampers" [24]. The model assumes an isotropic rotor, in which each blade is described as two rigid bodies connected through two hinges to allow for the blade flapwise and edgewise motions [24]. Each joint is related to a rotational spring and damper. Finally, the inner part of the blades is rigidly connected to the hub [24].

3.1.1. Nonlinear equations of motion

As presented by Riva et al. [24], the Lagrangian equations of motion are derived from the Lagrangian $L = T - V$, where T and V are the kinetic and potential energies of the system, respectively. First, the system's kinetic energy is composed of the kinetic energy of the hub and that of the blade. Hence, the energy of the blade's fixed and movable parts is considered. In addition, the potential energy of the system is contributed by the springs and gravity. Appendix A presents the nonlinear EoM derived in Riva et al. [24].

On the other hand, the aerodynamic forces and moments on the blade joints are calculated based on a linearised BEM approach developed by Eggleston and Stoddard [47], which assumes constant aerodynamic properties along the blades [24]. Furthermore, the model is extended to include the aerodynamic loads due to the tower motion. The aerodynamic forces and moments are: the hub shear force in the fore-aft direction, the hinge out-of-plane moment, the hub shear force in the direction parallel to the chord of the blade and pointing towards the leading edge, and the hinge moment in the edgewise direction.

The Lagrangian equations of the analytical wind turbine model are included in Appendix A. The second-order nonlinear model is obtained by reassembling the Lagrangian equations of motion and expressing them as a system linear in $\ddot{\boldsymbol{\xi}}$:

$$\mathbf{M}_{NL}(\dot{\boldsymbol{\xi}}, \boldsymbol{\xi}, t)\, \ddot{\boldsymbol{\xi}} + \boldsymbol{f}_{NL}(\boldsymbol{\xi}, \dot{\boldsymbol{\xi}}, \boldsymbol{\nu}, t) = \mathbf{0} \tag{3.1}$$

where $\mathbf{M}_{NL}$ is the nonlinear mass matrix, $\boldsymbol{f}_{NL}$ is the nonlinear forcing vector, $\boldsymbol{\nu}$ are the system inputs, i.e, the hub-height axial wind speed, and the blade and tower coordinates are collected in the displacement vector $\boldsymbol{\xi}$.

Isotropic steady-state configuration

The equilibrium configuration of the system $\tilde{\boldsymbol{\xi}}$ is found by computing the steady-state response of the nonlinear model. Correspondingly, isotropic conditions are assumed, and the expression in Eq. (3.1) is left-multiplied by the Coleman transformation, which allows to describe the rotating DOFs in the fixed frame of reference. By doing so, the system yields a time-invariant system. In a steady-state, the derivatives of the state variables with respect to time are zero ($\ddot{\tilde{\boldsymbol{\xi}}}, \dot{\tilde{\boldsymbol{\xi}}} = \mathbf{0}$). Thus, the system reduces to a nonlinear system of algebraic equations that can be solved for $\boldsymbol{\xi}$. Hence,

$$\boldsymbol{f}_{NL}(\tilde{\boldsymbol{\xi}}, \mathbf{0}, \tilde{\boldsymbol{\nu}}) = \mathbf{0}\,. \tag{3.2}$$

In an isotropic steady-state, the sine and cosine cyclic DOFs are zero. The remaining degrees of freedom are tower fore-aft, side-side, and flapwise and edgewise collective.

3.1.2. Linearised equations of motion

The linearised time-periodic equations of motion are derived by performing a first-order Taylor series expansion of the nonlinear system about the periodic equilibrium trajectory $\tilde{\boldsymbol{\xi}}(t)$ with inputs $\tilde{\boldsymbol{\nu}}(t)$. The second-order linear model reads:

$$\mathbf{M}(t)\ddot{\mathbf{q}}(t) + \mathbf{C}(t)\dot{\mathbf{q}}(t) + \mathbf{K}(t)\mathbf{q}(t) + \mathbf{F}(t)\mathbf{u}(t) = \mathbf{0} \tag{3.3}$$

where the perturbations to the inputs and the states about the equilibrium solution are expressed as $\mathbf{u}(t) = \boldsymbol{\nu}(t) - \tilde{\boldsymbol{\nu}}(t)$ and $\mathbf{q}(t) = \boldsymbol{\xi}(t) - \tilde{\boldsymbol{\xi}}(t)$, respectively. Also, $\mathbf{M}$, $\mathbf{C}$, $\mathbf{K}$ and $\mathbf{F}$ are the time-periodic linear mass, damping/gyroscopic, stiffness matrices and force vector, respectively.

Multi-blade coordinate transformation

To remove the periodic terms in the equations of motion, the simple wind turbine model is assumed to have an *isotropic* rotor with identically pitched blades ($\theta_{p,j} = \theta_p$) symmetrically mounted on the hub [43]. Also, the external (wind) conditions are assumed to be isotropic. Hence, the gravity force, cross-wind, and vertical wind shear terms are neglected. As described by Hansen [43], the linear time-periodic system in Eq. (3.3) can be then transformed into multi-blade coordinates (MBCs) through the Coleman transformation matrix $\mathbf{B}_\mathrm{q}$. The equations of the linear system expressed in the ground-fixed reference frame are:

$$\mathbf{M}_\mathrm{B}\ddot{\mathbf{q}}_\mathrm{B}(t) + \mathbf{C}_\mathrm{B}\dot{\mathbf{q}}_\mathrm{B}(t) + \mathbf{K}_\mathrm{B}\mathbf{q}_\mathrm{B}(t) + \mathbf{F}_\mathrm{B}\mathbf{u}_\mathrm{B}(t) = \mathbf{0} \tag{3.4}$$

where the vector of state variables is transformed as $\mathbf{q} = \mathbf{B}_\mathrm{q}\mathbf{q}_\mathrm{B}$, and the Coleman-transformed mass, damping/gyroscopic, and stiffness matrices, and force vector of the system read [43]:

$$\mathbf{M}_\mathrm{B} = \mathbf{B}_\mathrm{q}^{-1}\mathbf{M}\mathbf{B}_\mathrm{q} \tag{3.5a}$$

$$\mathbf{C}_\mathrm{B} = \mathbf{B}_\mathrm{q}^{-1}(2\mathbf{M}\mathbf{B}_\mathrm{q}\mathbf{R} + \mathbf{C}\mathbf{B}_\mathrm{q}) \tag{3.5b}$$

$$\mathbf{K}_\mathrm{B} = \mathbf{B}_\mathrm{q}^{-1}(\mathbf{M}\mathbf{B}_\mathrm{q}\mathbf{R}^2 + \mathbf{C}\mathbf{B}_\mathrm{q}\mathbf{R} + \mathbf{K}\mathbf{B}_\mathrm{q}) \tag{3.5c}$$

$$\mathbf{F}_\mathrm{B} = \mathbf{B}_\mathrm{q}^{-1}\mathbf{F} \tag{3.5d}$$

where $\mathbf{R} = \mathbf{B}_\mathrm{q}^{-1}\dot{\mathbf{B}}_\mathrm{q}$, and $\mathbf{B}_\mathrm{q}^{-1}$ is the inverse Coleman transformation matrix of the system.

Appendix A contains the Coleman-transformed mass, damping/gyroscopic, and stiffness matrices, as well as the force vector of the linear analytical wind turbine model derived by Riva et al. [24].

3.2. Aeroelastic BHawC model

The Bonus Horizontal Axis Wind turbine simulation Code (BHawC) tool is a nonlinear aero-hydro-servo-elastic code used to model and simulate wind turbines, first developed at Bonus Energy and then at Siemens Wind Power, both predecessors of Siemens Gamesa Renewable Energy (SGRE). BHawC serves as a design and certification tool for modern wind turbines [19] as it can calculate the dynamic response and the loads on three-bladed wind turbines. The modelling of the structure is done through a geometrically-nonlinear finite element model, which ensures a detailed representation of geometrical nonlinearities [32] and allows to resolve the large structural deflections of the model accurately. The aerodynamic loads on the turbine are calculated using a method based on the blade element momentum (BEM) theory [40]. Furthermore, the code is coupled to controllers to monitor the wind turbine conditions during its operation.

3.2.1. Structural model

The structural part of the BHawC aeroelastic code is based on a structural finite element model (FEM) using a co-rotational formulation. As shown in Fig. 3.2, the model is subdivided into various wind turbine substructures: foundation, tower, nacelle, drivetrain, shaft, hub, and blades [32], all connected through a predefined, direct kinematic coupling.

The substructures are modelled through two-node equilibrium formulation beam elements [19, 22] with 12 degrees of freedom, where the displacement vector at each node is defined by six degrees of freedom (DOFs), three translations and three rotations [32]. The structural degrees of freedom are described with respect to a turbine-base fixed frame of reference. The configuration of the system is given by the nodal positions $\boldsymbol{\rho}$ and the nodal orientations $\boldsymbol{\theta}$. The latter are expressed as quaternions [34], four-parameter representations of the rotation (or orientation) matrices. The nodal velocities and ac-

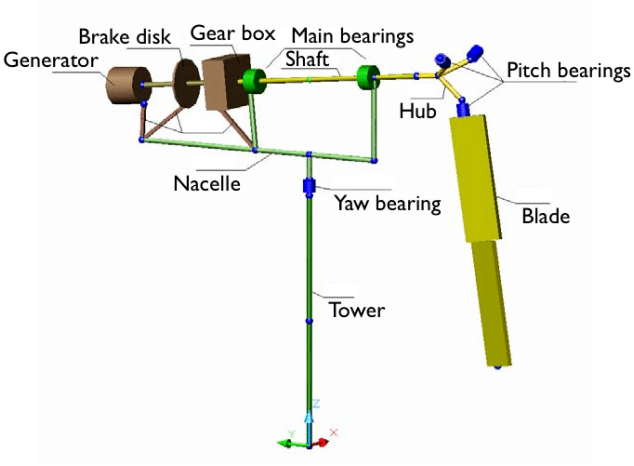

Figure 3.2: Substructures and components of the BHawC model. From Skjoldan [32]

celerations are collected in vectors $\dot{\boldsymbol{\xi}}$ and $\ddot{\boldsymbol{\xi}}$, respectively.

As described by Skjoldan [32], the equilibrium equation in the global coordinate system is

$$\mathbf{f}_{\text{iner}}(\boldsymbol{\rho}, \boldsymbol{\theta}, \dot{\boldsymbol{\xi}}, \ddot{\boldsymbol{\xi}}) + \mathbf{f}_{\text{damp}}(\boldsymbol{\theta}, \dot{\boldsymbol{\xi}}) + \mathbf{f}_{\text{int}}(\boldsymbol{\rho}, \boldsymbol{\theta}) = \mathbf{f}_{\text{ext}}(\boldsymbol{\rho}, \boldsymbol{\theta}, \dot{\boldsymbol{\xi}}, \ddot{\boldsymbol{\xi}}) \tag{3.6}$$

where $\mathbf{f}_{\text{iner}}$ is the inertial force vector, $\mathbf{f}_{\text{damp}}$ is the structural viscous damping force vector, $\mathbf{f}_{\text{int}}$ is the internal force vector corresponding to elastic deformation, and $\mathbf{f}_{\text{ext}}$ is the external force vector.

To find the equilibrium that satisfies Eq. (3.6) for a certain configuration and external force, the increments of the positions and orientations, $\mathbf{q}$ velocities $\dot{\mathbf{q}}$ and accelerations $\ddot{\mathbf{q}}$ are found by means of the tangent relation [32]:

$$\mathbf{M}(\boldsymbol{\theta})\ddot{\mathbf{q}} + \mathbf{C}(\boldsymbol{\theta}, \dot{\boldsymbol{\xi}})\dot{\mathbf{q}} + \mathbf{K}(\boldsymbol{\rho}, \boldsymbol{\theta}, \dot{\boldsymbol{\xi}}, \ddot{\boldsymbol{\xi}})\mathbf{q} = \mathbf{r} \tag{3.7}$$

where $\mathbf{M}$, $\mathbf{C}$, and $\mathbf{K}$ are the tangent mass, damping/gyroscopic forces, and stiffness matrices, respectively; the previous are periodic matrices with the rotor period $T = 2\pi/\Omega$, being Ω the rotor speed. Besides, the residual of the equations is expressed as $\mathbf{r} = \mathbf{f}_{\text{ext}} - \mathbf{f}_{\text{iner}} - \mathbf{f}_{\text{damp}} - \mathbf{f}_{\text{int}}$. As reported by Skjoldan [32], to get the increments in velocities and accelerations, a Newton-Raphson iteration method is used together with a suitable solution procedure until equilibrium is sufficiently satisfied ($\mathbf{r} \approx \mathbf{0}$).

3.2.2. Aerodynamic model

The aerodynamic part of the BHawC code is based on the principles of the blade element momentum (BEM) theory developed by Glauert [52], a widely-used method for simulating the aerodynamic rotor characteristics and computing the performance of wind turbines. Moreover, the model is extended to account for corrections for a finite number of blades (Prantl's tip correction), thrust at high induction values (Glauert's correction), skewed or unsteady inflow, tower shadow, dynamic stall, and swirl conditions [32]. The model also computes the aerodynamic forces on the nacelle and tower [44]. Next, the theoretical basis of the BEM theory is described.

Blade element momentum (BEM) theory

The blade element momentum (BEM) theory is the result of combining two independent methods: the *momentum theory*—based on the conservation of the linear and the angular momenta— and the *blade element theory*, which analyses the forces at a section of the blade as a function of the blade's geometry. The BEM theory uses the assumptions of (1) radial independence of the conditions in different stream tubes and (2) a purely two-dimensional axial and tangential flow, meaning that the two-dimensional airfoil properties determine the loading on the blades [44]. Next, the principles of the BEM method are described.

Momentum theory The one-dimensional momentum theory considers an axial free stream flow of speed U_0 past an actuator disc of area A with constant axial loading T [25]. The model uses the control volume shown in Fig. 3.3, where the stream tube encloses the rotor (actuator) disc. Also, it assumes that the pressure in the ultimate wake (far downstream) is equal to the undisturbed (upstream) pressure.

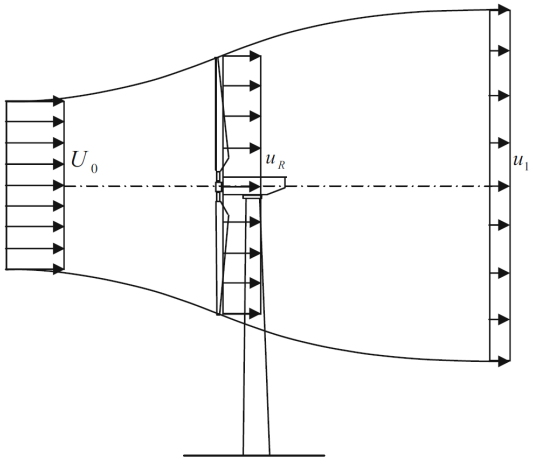

Figure 3.3: Control volume for one-dimensional actuator disc. From [25]

Applying the conservation of mass, particularly the continuity equation, yields

$$\dot{m} = \int \rho u \, \mathrm{d}A = \rho U_0 A_0 = \rho u_R A = \rho u_1 A_1 \tag{3.8}$$

where ρ is the air density, u_R is the axial velocity at the rotor, u_1 is the axial velocity in the ultimate wake, and A_0 and A_1 are the cross-sectional areas far upstream and far downstream of the actuator, respectively.

Furthermore, from the conservation of linear momentum, the thrust or loading on the rotor is expressed as:

$$T = \dot{m}\,(U_0 - u_1) = \rho u_R A\,(U_0 - u_1)\ . \tag{3.9}$$

Through Bernoulli's equation, the pressure drop in front of and behind the rotor leads to the definition of the axial induction factor:

$$a = (U_0 - u_R)\,/U_0\,. \tag{3.10}$$

Introducing Eq. (3.10) into the axial momentum balance in Eq. (3.9) results in the following expressions for the thrust and the extracted power:

$$T = 2\rho A U_0^2 a(1-a)\,, \quad P = u_R T = 2\rho A U_0^3 a(1-a)^2\,. \tag{3.11}$$

In turn, the non-dimensional thrust and power coefficient are $C_T = 4a(1-a)$ and $C_P = 4a(1-a)^2$, respectively.

Blade element theory The blade-element theory discretises each blade into N elements, which allows expressing the forces on the blades as a function of the two-dimensional aerodynamic coefficients (C_l and C_d) and the angle of attack α [25]. As seen in Fig. 3.4, the relative inflow velocity consists of the vector sum of the free wind speed $\mathbf{V}_0 = (0, U_0)$, the velocity due the to rotation of the blade $\mathbf{V}_\mathrm{r} = (\Omega r, 0)$, and the induced velocity $\mathbf{V}_\mathrm{ind} = (a'\Omega r, -aU_0)$. Hence, the inflow angle reads

$$\tan\Phi = \frac{U_0(1-a)}{\Omega r\,(1+a')} = \frac{1-a}{(1+a')\,\lambda_r} \tag{3.12}$$

where Ω is the rotor speed, $\lambda_r = \Omega r/U_0$ is the local tip speed ratio, and a and a' are the axial and tangential induction factors, respectively.

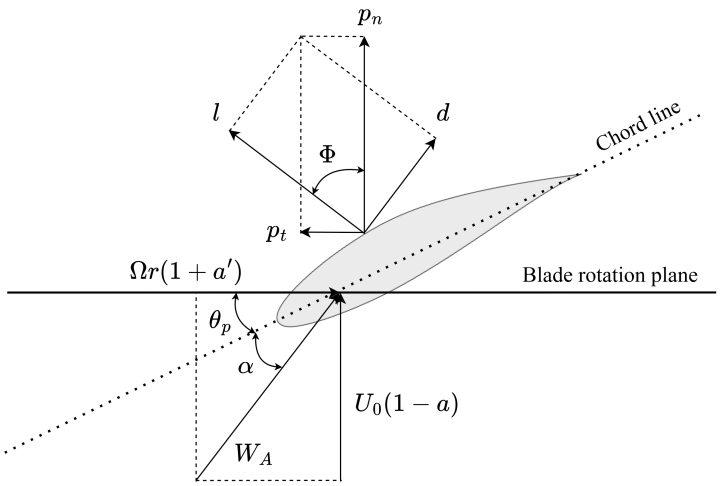

Figure 3.4: Velocity and force triangles for a blade section of a rotating wind turbine blade

Besides, the angle of attack α can be computed from the angle of the relative wind Φ and the section pitch angle θ_p, defined as the angle between the chord line and the plane of rotation as [27]:

$$\alpha = \Phi - \theta_p \tag{3.13}$$

where the section pitch θ_p is defined as the sum of the blade twist angle θ_T and the pitch at the blade tip $\theta_{p,0}$.

Then, the differential thrust $\mathrm{d}T$ in a control volume of radius r and thickness $\mathrm{d}r$ is derived by considering a finite number of blades B [25]. Similarly, for the differential torque $\mathrm{d}Q$ due to the tangential force operating at a radial distance r. Hence,

$$\mathrm{d}T = Bp_n = B\frac{1}{2}\rho W_A^2 C_n c\mathrm{d}r \tag{3.14a}$$

$$\mathrm{d}Q = Brp_t = B\frac{1}{2}\rho W_A^2 C_t c r\mathrm{d}r \tag{3.14b}$$

where c is the blade chord, p_n and p_t denote the force normal to the plane of rotation and tangential to the circle swept by the rotor, respectively, and C_n and C_t are the corresponding two-dimensional force coefficients, defined as:

$$C_n = C_l \cos\Phi + C_d \sin\Phi \tag{3.15a}$$

$$C_t = C_l \sin\Phi - C_d \cos\Phi \tag{3.15b}$$

where lift and drag aerodynamic coefficients at a given local angle of attack, $C_l = C_l(\alpha)$ and $C_d = C_d(\alpha)$, respectively, are obtained from tabulated airfoil data.

By now introducing the *local solidity* $\sigma = Bc(r)/2\pi r$, described as the "fraction of the annular area in the control volume which is covered by blades"[27], Eqs. (3.14a) and (3.14b) can be rewritten as:

$$\mathrm{d}T = \sigma\pi\rho\frac{U_0^2(1-a)^2}{\sin^2\Phi}C_n r\mathrm{d}r \tag{3.16a}$$

$$\mathrm{d}Q = \sigma\pi\rho\frac{U_0^2(1-a)^2}{\sin^2\Phi}C_t r^2\mathrm{d}r\,. \tag{3.16b}$$

Blade element momentum (BEM) theory Furthermore, the thrust on an annular element $\mathrm{d}T$ and the differential torque imparted to the blades $\mathrm{d}Q$ are a result of applying the conservation of axial and angular momenta, respectively. Hence,

$$\mathrm{d}T = 4a(1-a)\rho U_0^2 \pi r \mathrm{d}r \tag{3.17a}$$

$$\mathrm{d}Q = 4a'(1-a)\rho U_0 \pi r^3 \Omega \mathrm{d}r\,. \tag{3.17b}$$

Note that $u_R = U_0\,(1-a)$ is the axial velocity at the rotor, $u_1 = U_0\,(1-2a)$ is the axial velocity in the ultimate wake, and $u_\theta = 2\Omega r a'$ is the induced tangential velocity downstream of the rotor.

Therefore, the torque obtained in Eqs. (3.16b) and (3.17b) and the normal force in Eq. (3.17a) and (3.16a) can be equated. By also adding some algebraic relationships, the following expressions of the axial and tangential induction factors are obtained [25]:

$$a = \frac{1}{\frac{4\sin^2\Phi}{\sigma C_n} + 1} \tag{3.18a}$$

$$a' = \frac{1}{\frac{4\sin\Phi\cos\Phi}{\sigma C_t} - 1}\,. \tag{3.18b}$$

Once the induction factors are known, the total thrust and power can be computed as

$$T = B\int_0^R p_n\,\mathrm{d}r, \quad P = B\Omega\int_0^R r p_t\,\mathrm{d}r\,. \tag{3.19}$$

Among the drawbacks of the BEM theory are that it does not account for wake expansion, tip losses, and yaw. Consequently, to get acceptable results, the BEM model must include two corrections: the tip correction and the correction for heavily loaded rotors.

- Prandtl's tip loss factor:

  According to Hansen [27], the first correction addresses the assumption of an infinite number of blades, and it applies the following correction factor F to the forces derived from momentum theory:

  $$F = \frac{2}{\pi}\arccos\left(e^{-f}\right) \quad , \quad f = \frac{B}{2}\frac{R-r}{r\sin\Phi}\,. \tag{3.20}$$

  The result of modifying Eqs. (3.17a) and (3.17b) with the correction factor F is:

  $$\mathrm{d}T = 4\pi F r \rho U^2 a(1-a)\mathrm{d}r \quad , \quad \mathrm{d}Q = 4\pi F r^3 \rho U \Omega a'(1-a)\mathrm{d}r\,. \tag{3.21}$$

  While the induction factors in Eqs. (3.18a) and (3.18b) are also altered to:

  $$a = \frac{1}{\frac{4F\sin^2\Phi}{\sigma C_n} + 1} \quad , \quad a' = \frac{1}{\frac{4F\sin\Phi\cos\Phi}{\sigma C_t} - 1}\,. \tag{3.22}$$

- Glauert's correction for high values of a:

  The second correction relates the thrust coefficient C_T and the axial induction factor for heavily loaded rotors. As mentioned by Hansen [27], for high values of induction factor, $a > 0.4$ or $C_T > 0.96$, the one-dimensional momentum theory is no longer applicable due to the turbulent wake state that occurs in high winds. Consequently, Glauert [52] developed an empirical relationship between the axial induction factor and the thrust coefficient, including tip losses:

  $$a = \frac{1}{F}\left[0.143 + \sqrt{0.0203 - 0.6427\,(0.889 - C_T)}\right]\,. \tag{3.23}$$

  By introducing this relationship into the normal force derived from the blade element theory, the

local thrust coefficient for each annular rotor section can be expressed as:

$$C_{T_r} = \frac{\mathrm{d}F_N}{\frac{1}{2}\rho U^2 2\pi r \mathrm{d}r} = \sigma(1-a)^2 \left(C_l \cos\Phi + C_d \sin\Phi\right) / \sin^2\Phi \,. \tag{3.24}$$

Nowadays, most aeroelastic models use methods based on the BEM model to predict the aerodynamic loading on wind turbine blades. The computations usually use a uniform, constant inflow over the rotor disk in the rotor's design stages. However, detailed aeroelastic simulations are needed to assess the loads under various environmental and operating conditions, which are the requirements in the certification process. These include extreme inflow conditions such as strong shear and gusts and fault modes of the turbines, i.e., a large yaw error [16]. On that account, the BEM model is often extended with submodels for yawed conditions, dynamic inflow, and dynamic stall, as is the case of the BHawC aeroelastic model.

3.3. Reference wind turbine

The wind turbine model used for the preliminary comparison of the linear state-space model with the BHawC simulation tool is a direct-drive, multi-megawatt, three-bladed wind turbine developed at Siemens Gamesa Renewable Energy (SGRE). As explained in Section 3.2, the model is subdivided into substructures to represent the wind turbine's foundation, tower, nacelle, drivetrain, shaft, hub, and blades. The finite element model consists of 84 elements corresponding to 475 degrees of freedom. The degrees of freedom of the first tower node, located at the tower base or foundation, are constrained to avoid translations or rotations. Meanwhile, the aerodynamic loads are computed at the aerodynamic calculation points along the blades. Each blade has 60 aerodynamic sections, which yields a total of 180 aerodynamic state variables. The polars of the aerodynamic coefficients are also provided for angles of attack from $-180°$ to $180°$.

4

State-space formulation

Wind turbines (WTs) are complex, dynamic systems, as they cover multiple physical domains and have system states that evolve over time as a function of other independent variables. Therefore, a convenient way to represent WTs is through linear state-space models since they provide the system response to a given input while accounting for its dynamic behaviour. In this study, a state-space model is used to assess the loads acting on a wind turbine subject to a (turbulent) wind inflow. The linear model builds on the model developed by Skjoldan [32] to perform modal analysis, which corresponds to a linearised representation of the nonlinear BHawC model around a steady-state equilibrium. First, Section 4.1 discusses the linearisation of the BHawC aeroelastic code. Second, presents the derivation of the matrices of the linear system in the state-space formulation. Last, Sections 4.2 and 4.3 explain the model order reduction techniques used to lower the complexity of the large dynamic system.

4.1. Model linearisation

The linearisation process consists of two steps: (1) computing a periodic steady-state operating point for the states and (2) linearising the equations of motion about the steady-state to form the time-periodic state matrices. The approach in Skjoldan [32] is used to get the nominal state of the system, where a standard time simulation is performed until a sufficient approximation to the steady-state is reached. The operating point for a wind turbine system is periodic with the rotor azimuth position. Hence, the set of equations of motion also becomes periodic. Once the steady-state is found, the nonlinear aeroelastic model is linearised about the equilibrium configuration. To do so, the nonlinear model to describe the dynamics of the wind turbine is first expressed as a second-order system through a nonlinear function [24]:

$$\ddot{\boldsymbol{\xi}} = \boldsymbol{f}(\boldsymbol{\xi}, \dot{\boldsymbol{\xi}}, \boldsymbol{\nu}, t) \tag{4.1}$$

where $\boldsymbol{\xi}$ are the translational and rotational degrees of freedom, $\boldsymbol{\nu}$ are the inputs, and t refers to time.

The aeroelastic BHawC model can be described by linearised second-order equations of motion by making a first-order Taylor series expansion of $\boldsymbol{f}$ about the steady-state configuration. Introducing the perturbations to the states and inputs, $\mathbf{q}$ and $\mathbf{u}$, the equations of motion in terms of the new variables are given by:

$$\mathbf{M}(t)\ddot{\mathbf{q}} + \mathbf{C}(t)\dot{\mathbf{q}} + \mathbf{K}(t)\mathbf{q} = \mathbf{F}(t)\mathbf{u} \tag{4.2}$$

where the actual displacements $\boldsymbol{\xi}(t)$ are defined as the sum of the steady-state solution $\tilde{\boldsymbol{\xi}}$ and the small perturbations about the steady-state $\mathbf{q}$, and similarly for the inputs $\boldsymbol{\nu}(t)$ [31]:

$$\mathbf{q}(t) = \boldsymbol{\xi}(t) - \tilde{\boldsymbol{\xi}}(t)\ , \quad \mathbf{u}(t) = \boldsymbol{\nu}(t) - \tilde{\boldsymbol{\nu}}(t) \tag{4.3}$$

and the periodic mass $\mathbf{M}$, damping $\mathbf{C}$, stiffness $\mathbf{K}$, and input $\mathbf{F}$ matrices are defined as

$$\begin{aligned} \mathbf{M}(t) &= \left.\frac{\partial \boldsymbol{f}}{\partial \ddot{\boldsymbol{\xi}}}\right|_o , \qquad \mathbf{C}(t) = \left.\frac{\partial \boldsymbol{f}}{\partial \dot{\boldsymbol{\xi}}}\right|_o , \\ \mathbf{K}(t) &= \left.\frac{\partial \boldsymbol{f}}{\partial \boldsymbol{\xi}}\right|_o , \qquad \mathbf{F}(t) = \left.\frac{\partial \boldsymbol{f}}{\partial \boldsymbol{\nu}}\right|_o . \end{aligned} \tag{4.4}$$

where o refers to the equilibrium configuration $(\tilde{\boldsymbol{\xi}}, \dot{\tilde{\boldsymbol{\xi}}}, \ddot{\tilde{\boldsymbol{\xi}}}, \tilde{\boldsymbol{\nu}})$.

On the other hand, the output of the nonlinear wind turbine system $\boldsymbol{\gamma}$ satisfies a nonlinear algebraic equation as:

$$\boldsymbol{\gamma} = \boldsymbol{g}(\boldsymbol{\xi}, \dot{\boldsymbol{\xi}}, \ddot{\boldsymbol{\xi}}, \boldsymbol{\nu}, t) \, . \tag{4.5}$$

For this study, the outputs of interest correspond to the internal loads on the structural nodes in the global frame of reference. On that account, the loads on the wind turbine are determined through the force-displacement relationship. Consequently, it is assumed that the output only depends on the system's degrees of freedom and is therefore independent of the nodal velocities, the nodal accelerations, and the wind input. Hence, $\boldsymbol{\gamma} = \mathbf{f}^G_{\mathrm{E,int}} = \boldsymbol{g}(\boldsymbol{\xi}, t)$. Under the previous assumption, the linearised output equation is obtained by expanding its right-hand side into a first-order Taylor series about the nominal solution as:

$$\mathbf{y} = \left.\frac{\partial \boldsymbol{g}}{\partial \boldsymbol{\xi}}\right|_o \mathbf{q} = \mathbf{H}(t)\mathbf{q} \tag{4.6}$$

where $\mathbf{y} = \boldsymbol{\gamma}(t) - \tilde{\boldsymbol{\gamma}}(t)$ are the perturbations to the output and $\mathbf{H}$ is a matrix relating the system displacement and the internal loads.

In summary, Eqs. (4.3) and (4.6) are the linearised equations of motion around the equilibrium point that describe the dynamics of the nonlinear system "near" the steady-state.

4.2. State-space representation

Wind turbines are complex systems. In consequence, rather than describing the system using the second-order differential equation in Eq. (4.3), the system can be represented in state-space form through a set of first-order differential equations. The aeroelastic state-space formulation is obtained by considering a rearrangement of two systems of equations [9]. Although an obvious statement, the first equation reads $\dot{\mathbf{q}} = \dot{\mathbf{q}}$. On the other hand, the second system of equations is obtained by isolating the second derivative of the states in Eq. (4.2). The resulting state-space system of equations is expressed as:

$$\dot{\mathbf{x}}(t) = \mathbf{A}(t)\mathbf{x}(t) + \mathbf{B}(t)\mathbf{u}(t) \tag{4.7a}$$

$$\mathbf{y}(t) = \mathbf{C}(t)\mathbf{x}(t) + \mathbf{D}(t)\mathbf{u}(t) \tag{4.7b}$$

In the first-order representation of the system, the perturbations to the nodal displacements, velocities, and accelerations are replaced with the first-order $n \times 1$ state and state derivative vectors, $\mathbf{x}$ and $\dot{\mathbf{x}}$, respectively:

$$\mathbf{x} = \begin{bmatrix} \mathbf{q} \\ \dot{\mathbf{q}} \end{bmatrix}, \quad \dot{\mathbf{x}} = \begin{bmatrix} \dot{\mathbf{q}} \\ \ddot{\mathbf{q}} \end{bmatrix} \tag{4.8}$$

while $\mathbf{u}$ denotes the $n_i \times 1$ input vector, $\mathbf{y}$ the $n_o \times 1$ output vector, $\mathbf{A}$ the $n \times n$ state (system) matrix, $\mathbf{B}$ the $n \times n_i$ input matrix, $\mathbf{C}$ the $n_o \times n$ output matrix, and $\mathbf{D}$ the $n_i \times n_o$ feedforward matrix (usually zero). In this form, the first-order system matrices are related to their second-order counterparts as follows:

$$\mathbf{A} = \left.\frac{\partial \boldsymbol{f}}{\partial \mathbf{x}}\right|_o = \begin{bmatrix} \mathbf{0} & \mathbf{I} \\ -\mathbf{M}^{-1}\mathbf{K} & -\mathbf{M}^{-1}\mathbf{C} \end{bmatrix} \tag{4.9a}$$

$$\mathbf{B} = \left.\frac{\partial \boldsymbol{f}}{\partial \mathbf{u}}\right|_o = \begin{bmatrix} \mathbf{0} \\ \mathbf{M}^{-1}\mathbf{F} \end{bmatrix} \tag{4.9b}$$

$$\mathbf{C} = \left.\frac{\partial \boldsymbol{g}}{\partial \mathbf{x}}\right|_o = \begin{bmatrix} \mathbf{H} & \mathbf{0} \end{bmatrix} \tag{4.9c}$$

$$\mathbf{D} = \left.\frac{\partial \boldsymbol{g}}{\partial \mathbf{u}}\right|_o = \mathbf{0}\,. \tag{4.9d}$$

Next, the derivation of the matrices in the state-space formulation of the linear model is explained in detail. For this work, the tangent matrices of the linearised model are extracted from BHawC. Then, the state-space form of the linear model is developed in MATLAB®.

4.2.1. System matrix

The system matrix **A** of the linear model corresponds to the matrix developed by Skjoldan [32] to perform modal analysis in BHawC. The linearised equations of motion contain both a structural and an aerodynamic part. The linear structural model is extracted directly from BHawC using the tangent system matrices in Eq. (3.7) when the turbine is in a steady-state [32]. In contrast, the linear aerodynamic model is obtained through the numerical linearisation of the aerodynamic force. In this study, however, the unsteady aerodynamic equations are not included since they introduce a complex dependence between the aerodynamic force and the state variables. The effects of dynamic inflow and pitch or speed control are currently also excluded from the analysis [32]. Combining the linearised structural and aerodynamic matrices and assembling them into state-space form leads to the system matrix described above in Eq. (4.9a).

4.2.2. Input matrix

The input matrix of the state-space model is defined from the linearised equations of motion as seen in Eq. (4.9b). For the wind turbine system, the input signal $\boldsymbol{\nu}$ corresponds to the free wind speed in the global frame of reference $\mathbf{V}_0^G$. The external force vector is the vector of aerodynamic loads represented in global coordinates $\mathbf{f}_{\text{E,aero}}^G$. Thereby, the input matrix in Eq. (4.9b) relating the system inputs to its state variables can be rewritten as:

$$\mathbf{B} = \begin{bmatrix} \mathbf{0} \\ \mathbf{M}^{-1}\mathbf{F} \end{bmatrix}, \quad \mathbf{F} = \left.\frac{\partial \boldsymbol{f}}{\partial \boldsymbol{\nu}}\right|_o = \left.\frac{\partial \mathbf{f}_{\text{E,aero}}^G}{\partial \mathbf{V}_0^G}\right|_o \tag{4.10}$$

where o denotes the steady-state solution, and the subscript G denotes the global frame of reference of the system.

As mentioned above in Section 3.2.2, the aerodynamic loads in the BHawC code are calculated using a method based on the blade element momentum (BEM) theory. The code also uses corrections for dynamic inflow effects, inclined (yawed or tilted) flow to the rotor disc, and unsteady blade aerodynamics [40]. Nevertheless, for this research, only the aerodynamic forces acting on the rotor blades are examined, while those acting on the other substructures (tower and nacelle) are neglected. Also, the linearisation does not consider neither dynamic stall nor dynamic inflow models.

The forcing vector of the state-space model is linearised analytically, which allows getting an exact solution and so avoiding the approximation error of numerical approaches. As a consequence, the partial derivative of the aerodynamic forces applied on the structural nodes (external forces) with respect to the free wind at the aerodynamic calculation points (inputs) in Eq. (4.10) is obtained by analytical equations. The results are cross-checked with the symbolic differentiation tool in MATLAB®.

For simplicity, rather than computing the partial derivatives on the whole system, they are separated into the three elementary blocks in Eq. (4.11). First, block 'B1' relates the free wind speed in the global frame $\mathbf{V}_0^G$ to the relative wind speed in the aerodynamic frame $\mathbf{W}_{\text{A}}^A$. Recall that the aerodynamic loads in BHawC are calculated at several *aerodynamic calculation points* along the wind turbine and positioned

independently of the structural nodes [32]. On that account, block 'B2' derives the aerodynamic loads (forces and moments) at the aerodynamic calculation points in the local coordinate aerodynamic system $\mathbf{f}^A_{\mathrm{A,aero}}$ with respect to the relative wind speed $\mathbf{W}^A_{\mathrm{A}}$. Last, block 'B3' relates the global aerodynamic loads on the wind turbine structure $\mathbf{f}^G_{\mathrm{E,aero}}$ to those in the local aerodynamic frame. The partial derivative in Eq. (4.10) is assembled via the chain rule as:

$$\frac{\partial \mathbf{f}^G_{\mathrm{E,aero}}}{\partial \mathbf{V}^G_0} = \underbrace{\frac{\partial \mathbf{W}^A_{\mathrm{A}}}{\partial \mathbf{V}^G_0}}_{\mathrm{B1}} \underbrace{\frac{\partial \mathbf{f}^A_{\mathrm{A,aero}}}{\partial \mathbf{W}^A_{\mathrm{A}}}}_{\mathrm{B2}} \underbrace{\frac{\partial \mathbf{f}^G_{\mathrm{E,aero}}}{\partial \mathbf{f}^A_{\mathrm{A,aero}}}}_{\mathrm{B3}} \tag{4.11}$$

where A denotes the local aerodynamic coordinate system, E is the structural element system, and G refers to the global frame.

Next, the analytical derivation of the elementary blocks in Eq. (4.11) is examined in detail:

B1 For an operating wind turbine, the inflow wind speed in the global coordinate system $\mathbf{W}^G_{\mathrm{A}}$ is composed as the sum of the free wind $\mathbf{V}^G_0$, the induced velocities $\mathbf{V}^G_{\mathrm{ind}}$, and the blade motion (translational and rotational velocities of the blade nodes) $\dot{\mathbf{V}}^G$ [44]:

$$\mathbf{W}^G_{\mathrm{A}} = \mathbf{V}^G_0 + \mathbf{V}^G_{\mathrm{ind}} + \dot{\mathbf{V}}^G \ . \tag{4.12}$$

The induced velocities are assumed to be constant since their variation would require using a new state variable and integrating dynamic wake models in the linearised BHawC model. Besides, the local relative wind speed at the aerodynamic calculation points $\mathbf{W}^A_{\mathrm{A}}$ is related to $\mathbf{W}^G_{\mathrm{A}}$ through the three-by-three matrix rotation matrices of the aerodynamic sections $\mathbf{T}_{\mathrm{A}}$ defining their spatial orientation as:

$$\mathbf{W}^A_{\mathrm{A}} = \mathbf{T}_{\mathrm{A}} \mathbf{W}^G_{\mathrm{A}} \ . \tag{4.13}$$

The aerodynamic orientation matrices are independent of the free wind speed. Consequently, applying the chain rule, the partial derivative of block 'B1' in Eq. (4.11) reads

$$\frac{\partial \mathbf{W}^A_{\mathrm{A}}}{\partial \mathbf{V}^G_0} = \underbrace{\frac{\partial \mathbf{T}_{\mathrm{A}}}{\partial \mathbf{V}^G_0}}_{=0} \mathbf{W}^G_{\mathrm{A}} + \mathbf{T}_{\mathrm{A}} \frac{\partial \mathbf{W}^G_{\mathrm{A}}}{\partial \mathbf{V}^G_0} = \mathbf{T}_{\mathrm{A}} \ . \tag{4.14}$$

Thus, block 'B1' simplifies to the orientation matrices of the aerodynamic calculation points, positioned along the blades.

B2 As mentioned above, BHawC uses methods based on the BEM theory to compute the aerodynamic loads on the wind turbine blades. These methods determine the tangential and axial induced velocities at the aerodynamic calculation points [44], and include various corrections such as the Prandtl tip loss factor and a correction for the thrust at high induction values.

Mainly, the aerodynamic loads are due to the inflow wind speed described in the local aerodynamic frame $\mathbf{W}^A_{\mathrm{A}}$ at a given incidence angle α. Besides, for wind turbines, the spanwise velocity component is much lower than the streamwise component. Therefore, the flow at a given point can be considered two-dimensional. According to the 2-D aerodynamics assumption, the force in the z_{A}-axis (perpendicular to the aerodynamic section) and the moments about the x_{A} and y_{A} directions (in the plane of the profile) are neglected. That being the case, $\mathbf{f}^A_{\mathrm{A}}$ consists of the lift and drag forces and the pitching moment, which are calculated at each aerodynamic point along the wind turbine blades. Fig. 4.1 illustrates the relative velocity triangle and the aerodynamic forces acting on a blade section. As seen, the aerodynamic coordinate system has the positive x_{A}-axis from the airfoil trailing edge to the leading edge, and the y_{A}-axis is defined as positive from the pressure side to the suction side.

In line with the BEM theory explained in Section 3.2.2 and using the velocity triangle at a blade

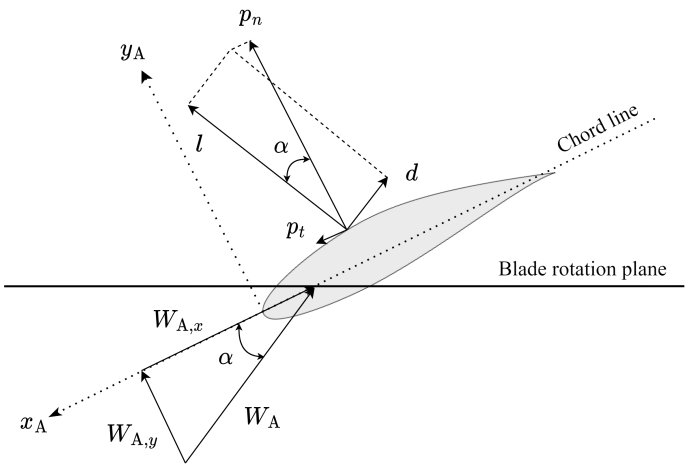

Figure 4.1: Velocity triangle and aerodynamic loads acting on an aerodynamic calculation point in the BHawC model

section (see Fig. 4.1), the angle of incidence is defined as the angle between the airfoil chordline and the relative inflow direction. In addition, note that the relative wind speed $\mathbf{W}_A^A$ is the disturbed wind velocity, meaning it accounts for the free wind speed, the rotor speed, and the velocity induced by the rotor. Thus, the angle of attack can be written in terms of the components of the relative wind speed as:

$$\alpha = \text{atan2}\left(\frac{W_{A,y}}{-W_{A,x}}\right) \quad , \quad W_A = |\mathbf{W}_A^A| = \sqrt{W_{A,x}^2 + W_{A,y}^2} \, . \tag{4.15}$$

According to the two-dimensional aerodynamic theory, the lift force l is, by definition, perpendicular to the relative wind speed seen by the airfoil, while the drag force d is parallel to said velocity. On that account, the aerodynamic forces are modelled as:

$$l = \frac{1}{2}\rho W_A^2 c C_l(\alpha) \tag{4.16a}$$

$$d = \frac{1}{2}\rho W_A^2 c C_d(\alpha) \tag{4.16b}$$

and the aerodynamic pitching moment about the aerodynamic centre, located at the airfoil quarter-chord point, reads

$$m_{c/4} = \frac{1}{2}\rho W_A^2 c^2 C_m(\alpha) \tag{4.16c}$$

where ρ is the density, c is the chord length at the blade section, and C_l, C_d, and C_m are the airfoil lift, drag, and pitching moment coefficients, respectively.

The aerodynamic profile coefficients are determined at a given angle of attack from the airfoil polars. While 3-D corrections are considered, the dynamic stall effects are neglected [32]. The spacing between the fixed angles of attack is 1° between −180° and 180°. A shape-preserving spline is used to interpolate between the values at fixed angles of attack while getting a faithful representation of the slopes. Specifically, the monotone piecewise cubic interpolation (PCHIP) described by Fritsch and Carlson [48] is used. This way, the flat regions can be connected accurately, and overshoots avoided [6].

Given that the local aerodynamic frame of reference has its x_A-axis aligned with the airfoil's chord line, the lift and drag forces can be re-expressed in the local x_A and y_A directions as the normal and tangential forces (see Fig. 4.1):

$$p_n = l\cos\alpha + d\sin\alpha \tag{4.17a}$$

$$p_t = l \sin\alpha - d \cos\alpha \tag{4.17b}$$

Similarly, the moment about the reference point o reads

$$m_o = m_{c/4} - x_{ac}\, p_n - y_{ac}\, p_t \tag{4.17c}$$

where x_{ac} and y_{ac} are the distance from the aerodynamic center to the reference point along the x_A and y_A directions, respectively.

Assembling the forces and moment derived above, the 3D aerodynamic loads at the aerodynamic calculation points are

$$\mathbf{f}^A_{\mathrm{A,aero}} = \begin{bmatrix} p_t & p_n & 0 & 0 & 0 & m_o \end{bmatrix}^\top . \tag{4.18}$$

As mentioned above, the aerodynamic loads $\mathbf{f}^A_{\mathrm{A,aero}}$ are a function of two variables: the relative wind speed $\mathbf{W}^A_\mathrm{A}$ and the incidence angle α. Consequently, the partial derivative of block 'B2' in Eq. (4.11) is obtained by applying the chain rule for multivariable functions as:

$$\frac{\partial \mathbf{f}^A_{\mathrm{A,aero}}}{\partial \mathbf{W}^A_\mathrm{A}} = \frac{\partial \mathbf{f}^A_{\mathrm{A,aero}}}{\partial W_\mathrm{A}} \frac{\partial W_\mathrm{A}}{\partial \mathbf{W}^A_\mathrm{A}} + \frac{\partial \mathbf{f}^A_{\mathrm{A,aero}}}{\partial \alpha} \frac{\partial \alpha}{\partial \mathbf{W}^A_\mathrm{A}} . \tag{4.19}$$

In short, the partial derivative in Eq. (4.19) yields from deriving the aerodynamic force vector in Eq. (4.18) with respect to the angle of attack and relative wind speed vector at the aerodynamic sections. Following, the analytical expressions of the obtained partial derivatives are displayed in Eqs. (4.20a) to (4.20d):

$$\frac{\partial \mathbf{f}^A_{\mathrm{A,aero}}}{\partial W_\mathrm{A}} = \frac{1}{2}\rho W_\mathrm{A} c \begin{bmatrix} C_l \sin\alpha - C_d \cos\alpha \\ C_l \cos\alpha + C_d \sin\alpha \\ 0 \\ 0 \\ 0 \\ C_m\, c - x_{ac} \frac{\partial p_n}{\partial W_\mathrm{A}} - y_{ac} \frac{\partial p_t}{\partial W_\mathrm{A}} \end{bmatrix} \tag{4.20a}$$

$$\frac{\partial W_\mathrm{A}}{\partial \mathbf{W}^A_\mathrm{A}} = \frac{1}{W_\mathrm{A}} \begin{bmatrix} W_{\mathrm{A},x} & W_{\mathrm{A},y} & 0 \end{bmatrix} \tag{4.20b}$$

$$\frac{\partial \mathbf{f}^A_{\mathrm{A,aero}}}{\partial \alpha} = \frac{1}{2}\rho W_\mathrm{A}^2 c \begin{bmatrix} (C_{l\alpha} + C_d)\sin\alpha + (C_l - C_{d\alpha})\cos\alpha \\ (C_{d\alpha} - C_l)\sin\alpha + (C_{l\alpha} + C_d)\cos\alpha \\ 0 \\ 0 \\ 0 \\ C_{m\alpha}\, c - x_{ac} \frac{\partial p_n}{\partial \alpha} - y_{ac} \frac{\partial p_t}{\partial \alpha} \end{bmatrix} \tag{4.20c}$$

$$\frac{\partial \alpha}{\partial \mathbf{W}^A_\mathrm{A}} = \frac{1}{W_\mathrm{A}^2} \begin{bmatrix} W_{\mathrm{A},y} & -W_{\mathrm{A},x} & 0 \end{bmatrix} \tag{4.20d}$$

where $C_{l\alpha} = \frac{\partial C_l}{\partial \alpha}$ and $C_{d\alpha} = \frac{\partial C_d}{\partial \alpha}$ are the lift and drag coefficient derivatives with respect to the angle of attack.

B3 The aerodynamic loads at the structural nodes in global coordinates are obtained through the transformation matrix $\mathbf{T}_\mathrm{AE}$, which maps the aerodynamic point forces per unit length in aerodynamic coordinates to forces at the full system degrees of freedom in global coordinates:

$$\mathbf{f}^G_{\mathrm{E,aero}} = \mathbf{T}_\mathrm{AE}\, \mathbf{f}^A_{\mathrm{A,aero}} . \tag{4.21}$$

Note that the $\mathbf{T}_\mathrm{AE}$ matrix consists of the aeroelastic transformation matrix together with matrices containing the weights for the integration of the distributed forces at the aerodynamic points onto the structural elements (with two nodes) both in global coordinates. As it is a constant mapping

matrix, block 'B3' in Eq. (4.11) reads

$$\frac{\partial \mathbf{f}^G_{\mathrm{E,aero}}}{\partial \mathbf{f}^A_{\mathrm{A,aero}}} = \mathbf{T}_{\mathrm{AE}} \,. \tag{4.22}$$

Finally, the partial derivative of the loads on the structural nodes with respect to the free wind speed in Eq. (4.11) yields from assembling blocks 'B1' to 'B3' in Eqs. (4.14), (4.19) and (4.22). Hence,

$$\frac{\partial \mathbf{f}^G_{\mathrm{E,aero}}}{\partial \mathbf{V}^G_0} = \frac{\partial \mathbf{f}^G_{\mathrm{E,aero}}}{\partial \mathbf{f}^A_{\mathrm{A,aero}}} \frac{\partial \mathbf{f}^A_{\mathrm{A,aero}}}{\partial \mathbf{W}^A_{\mathrm{A}}} \frac{\partial \mathbf{W}^A_{\mathrm{A}}}{\partial \mathbf{V}^G_0} = \mathbf{T}_{\mathrm{AE}} \underbrace{\frac{\partial \mathbf{f}^A_{\mathrm{A,aero}}}{\partial \mathbf{W}^A_{\mathrm{A}}}}_{\text{Eq. (4.19)}} \mathbf{T}_{\mathrm{A}} \,. \tag{4.23}$$

4.2.3. Output matrix

From the state-space representation of the system, the output matrix relates the state variables to the output of interest. As mentioned previously, this study focuses on assessing the internal forces at the structural nodes in the global frame of reference $\mathbf{f}^G_{\mathrm{E,int}}$. The former are assumed to be independent from the nodal velocities $\dot{\boldsymbol{\xi}}$ and accelerations $\ddot{\boldsymbol{\xi}}$, as well as from the input signal $\boldsymbol{\nu}$. Therefore, the output matrix of the state-space model can be expressed as:

$$\mathbf{C} = \left.\frac{\partial \boldsymbol{g}}{\partial \mathbf{x}}\right|_o = \begin{bmatrix} \mathbf{H} & \mathbf{0} \end{bmatrix}, \quad \mathbf{H}(t) = \left.\frac{\partial \boldsymbol{g}}{\partial \boldsymbol{\xi}}\right|_o \tag{4.24}$$

where, again, o denotes the equilibrium solution (steady-state) of the system.

Next, the derivation of the internal loads is explained, as well as their relation to the state variables. This work is based on internal documentation developed at SGRE.

The BHawC code models the structure of a wind turbine through three-dimensional finite beam elements with two nodes [32]. Other elements not included in this study are torsional springs with two nodes and torsional springs coupled to the beam elements. Fig. 4.2 illustrates a finite beam element of initial length ℓ_0, where the element frame of reference is positioned on the elastic axis with the z_{E}-axis along the element length.

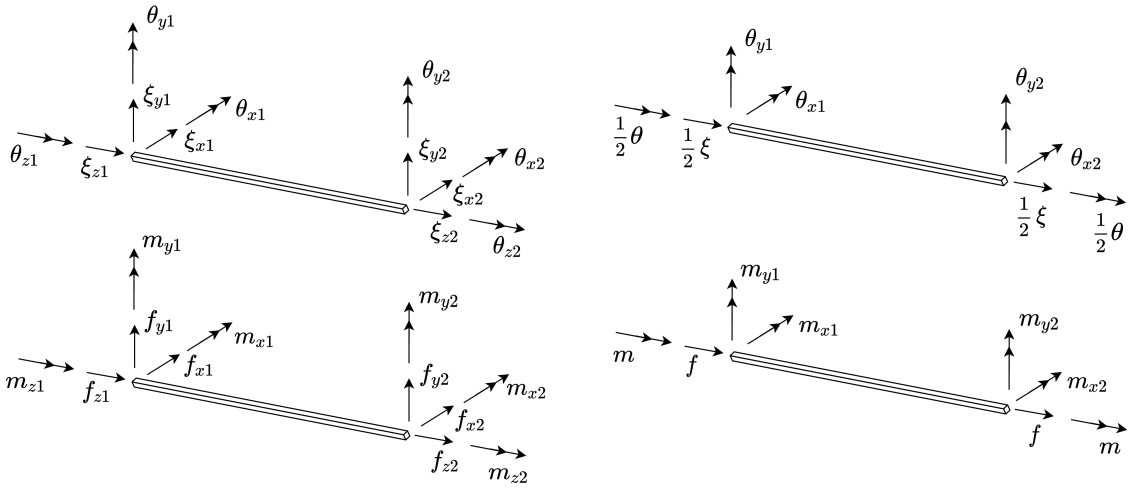

(a) Full format **(b)** Equilibrium format

Figure 4.2: Beam element displacements and forces in full and equilibrium format. Adapted from Krenk and Couturier [22]

The twelve degrees of freedom of the beam elements are collected in the full format displacement vector

(see Fig. 4.2a):

$$\boldsymbol{\xi}_\mathrm{f} = \left[\boldsymbol{\xi}_{1\mathrm{f}}, \boldsymbol{\xi}_{2\mathrm{f}}\right]^\top, \quad \boldsymbol{\xi}_{j\mathrm{f}} = \left[\xi_{xj\mathrm{f}} \quad \xi_{yj\mathrm{f}} \quad \xi_{zj\mathrm{f}} \quad \theta_{xj\mathrm{f}} \quad \theta_{yj\mathrm{f}} \quad \theta_{zj\mathrm{f}}\right]^\top \tag{4.25a}$$

where j denotes one of the two nodes, $\xi_{ij\mathrm{f}}$ and $\theta_{ij\mathrm{f}}$ are the translations and the rotations of the element node, respectively, and the corresponding load vector consists of the forces $f_{ij\mathrm{f}}$ and moments $m_{ij\mathrm{f}}$ as:

$$\mathbf{f}_\mathrm{f} = \left[\mathbf{f}_{1\mathrm{f}}, \mathbf{f}_{2\mathrm{f}}\right]^\top, \quad \mathbf{f}_{j\mathrm{f}} = \left[f_{xj\mathrm{f}} \quad f_{yj\mathrm{f}} \quad f_{zj\mathrm{f}} \quad m_{xj\mathrm{f}} \quad m_{yj\mathrm{f}} \quad m_{zj\mathrm{f}}\right]^\top \tag{4.25b}$$

The displacement of the beam elements can be separated into an elastic deformation of the element, described in the local, corotational frame, and a rigid-body displacement given by the motion of the coordinate system. Hence, the equilibrium format displacements and forces depicted in Fig. 4.2b are introduced, which describe the displacement due to elastic deformation as:

$$\boldsymbol{\xi}_\mathrm{eq} = \left[\xi \quad \theta \quad \theta_{x1} \quad \theta_{y1} \quad \theta_{x2} \quad \theta_{y2}\right]^\top \tag{4.26a}$$

where ξ is the longitudinal translation and θ_{ij} and θ are the nodal rotations.

The corresponding equilibrium format forces are expressed through the axial force f and the nodal moments m and m_{ij} as:

$$\mathbf{f}_\mathrm{eq} = \left[f \quad m \quad m_{x1} \quad m_{y1} \quad m_{x2} \quad m_{y2}\right]^\top. \tag{4.26b}$$

The conversion between full and equilibrium formats can be obtained through a transformation matrix as follows:

$$\mathbf{f}_\mathrm{f} = \mathbf{S}\,\mathbf{f}_\mathrm{eq}, \quad \mathrm{d}\mathbf{q}_\mathrm{eq} = \mathbf{S}^\top \mathrm{d}\mathbf{q}_\mathrm{f} \tag{4.27a}$$

where

$$\mathbf{S} = \begin{bmatrix} 0 & 0 & 0 & 1/\ell_0 & 0 & 1/\ell_0 \\ 0 & 0 & -1/\ell_0 & 0 & -1/\ell_0 & 0 \\ -1 & 0 & 0 & 0 & 0 & 0 \\ 0 & 0 & 1 & 0 & 0 & 0 \\ 0 & 0 & 0 & 1 & 0 & 0 \\ 0 & -1 & 0 & 0 & 0 & 0 \\ 0 & 0 & 0 & -1/\ell_0 & 0 & -1/\ell_0 \\ 0 & 0 & 1/\ell_0 & 0 & 1/\ell_0 & 0 \\ 1 & 0 & 0 & 0 & 0 & 0 \\ 0 & 0 & 0 & 0 & 1 & 0 \\ 0 & 0 & 0 & 0 & 0 & 1 \\ 0 & 1 & 0 & 0 & 0 & 0 \end{bmatrix}. \tag{4.27b}$$

For a two-noded beam element, the internal forces and the displacements are related through the element stiffness matrix $\mathbf{K}_\mathrm{E}^E$, which accounts for both the constitutive and the geometric element stiffness matrices. Note that the constitutive stiffness matrices in equilibrium format $\mathbf{K}_{\mathrm{E,const,eq}}^E$ is transformed into the full format through the conversion matrix in Eq. (4.27b). Hence,

$$\mathbf{K}_\mathrm{E}^E = \mathbf{K}_{\mathrm{E,const}}^E + \mathbf{K}_{\mathrm{E,geom}}^E = \mathbf{S}\mathbf{K}_{\mathrm{E,const,eq}}^E\mathbf{S}^\top + \mathbf{K}_{\mathrm{E,geom}}^E \tag{4.28}$$

Besides, the equations of motions in element coordinates can be assembled into a global form for the whole structure through the element rotation matrix. As a result, the element stiffness can be assembled into global form in global coordinates as:

$$\mathbf{K}_\mathrm{E}^G = \mathbf{T}_{\mathrm{E},4}\mathbf{K}_\mathrm{E}^E\mathbf{T}_{\mathrm{E},4}^\top \tag{4.29}$$

where $\mathbf{T}_{\mathrm{E},4}$ is a matrix with four copies of the three-by-three element orientations in the block diagonal.

Finally, to get the internal loads of the system, the force-displacement relationship is used:

$$\mathbf{f}_{\mathrm{E,int}}^G = \mathbf{K}_\mathrm{E}^G\,\boldsymbol{\xi}_\mathrm{f}. \tag{4.30}$$

Therefore, the matrix relating the displacements and the internal loads in Eq. (4.24) can be written as $\mathbf{H} = \mathbf{K}_{\mathrm{E}}^{G}$, and the output matrix yields

$$\mathbf{C} = \left.\frac{\partial \boldsymbol{g}}{\partial \mathbf{x}}\right|_{o} = \begin{bmatrix} \mathbf{K}_{\mathrm{E}}^{G} & \mathbf{0} \end{bmatrix}. \tag{4.31}$$

Specifically, the load channels of interest are the blade tower fore-aft and side-side and torsion moments as well as the blade-root flapwise, edgewise and torsion moments, which leads to having a very sparse output matrix with few non-zero entries, as seen in the lower-left quadrant of Fig. 4.3.

4.2.4. Feedforward matrix

The state-space system is assumed to not have direct feedthrough signals as, for instance, the controller is not included in the linearisation of the BHawC equations. Therefore, the feedforward matrix yields a $n_i \times n_o$ zero matrix as:

$$\mathbf{D} = \left.\frac{\partial \boldsymbol{g}}{\partial \mathbf{u}}\right|_{o} = \mathbf{0}. \tag{4.32}$$

Once the state-space matrices of the dynamic system (**A**, **B**, **C**, and **D**) are derived and assembled, the resulting full order model (FOM) is a sparse state-space multi-input and multi-output (MIMO) system. The wind turbine FOM has $n = 938$ state variables: 469 states related to the perturbations to the nodal displacements about the equilibrium configuration $\mathbf{q}$, and another 469 states regarding the perturbations to nodal velocities about the steady-state solution $\dot{\mathbf{q}}$. Fig. 4.3 shows the sparsity pattern of the full LTI state-space model at a given operating point. As seen, the number of non-zero elements (nnz) is significantly less than the number of entries of the full matrix, which has great potential in terms of storage requirements. Besides, the input matrix (upper-right quadrant in Fig. 4.3) only contains entries for the state variables related to the blades' substructure. The output matrix (bottom-left quadrant) only contains a few entries along its principal diagonal, corresponding to the relevant load channels of the system.

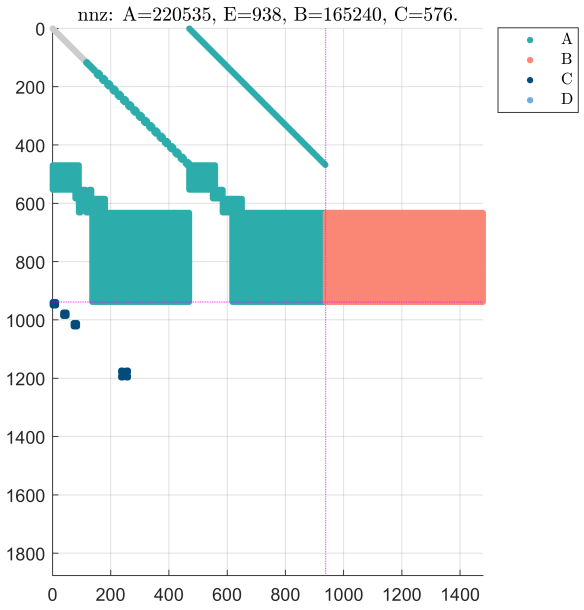

Figure 4.3: Sparsity pattern of the wind turbine LTI system

Appendix C contains the validation of the matrices of the state-space model. The validity of the input matrix is checked by means of a finite difference method. Additionally, the output matrix is examined by computing the time-domain response of the system to a ramping force input.

Below, the model order reduction (MOR) method used to obtain a low-order approximation of the system's relevant dynamics is explained, which is advantageous for reducing the computational complexity of the simulations, both in terms of storage requirements and run times.

4.3. Model order reduction

Large-scale models often result in high demand for computational resources and require a large amount of calculation time to obtain an accurate solution [10]. As a result, model-order reduction (MOR) methods are frequently used to reduce the complexity of the model. In short, projection-based MOR concerns with reducing the dimensions of nth-order dynamical systems represented in state-space form as:

$$\mathbf{E}\dot{\mathbf{x}} = \mathbf{A}\mathbf{x} + \mathbf{B}\mathbf{u}, \quad \mathbf{y} = \mathbf{C}\mathbf{x} + \mathbf{D}\mathbf{u}\,. \tag{4.33}$$

by substituting the model with a rth-order lower-dimensional model ($r \ll n$) [17]. Hence, it finds the projection subspaces $\mathbf{V}$ and $\mathbf{W}$ that allow formulating the reduced-order model (ROM) as

$$\mathbf{E}_r\dot{\mathbf{x}}_r = \mathbf{A}_r\mathbf{x}_r + \mathbf{B}_r\mathbf{u}, \quad \mathbf{y} = \mathbf{C}_r\mathbf{x}_r + \mathbf{D}_r\mathbf{u} \tag{4.34}$$

where the transformation matrix $\mathbf{V}$ is defined such that $\mathbf{x} \approx \mathbf{V}\mathbf{x}_r$ holds [41], and

$$\begin{aligned} \mathbf{E}_r &= \mathbf{W}^\top\mathbf{E}\mathbf{V}, \quad \mathbf{B}_r = \mathbf{W}^\top\mathbf{B} \\ \mathbf{A}_r &= \mathbf{W}^\top\mathbf{A}\mathbf{V}, \quad \mathbf{C}_r = \mathbf{C}\mathbf{V}, \quad \mathbf{D}_r = \mathbf{D}\,. \end{aligned} \tag{4.35}$$

As described by Antoulas [38], various MOR methods exist to reduce a system's complexity. Amongst them, the one used in this project is the *balanced truncation* (BT), which has the objective of identifying and preserving the dominant states, those states that "need the least energy to be controlled and at the same time result in the most energy through observation" [41]. Thus, the states that are hard to excite or difficult to observe are discarded.

Determining the projection matrices $\mathbf{V}$ and $\mathbf{W}$ is based on the controllability and observability of the system. Consequently, to identify the dominant states, the controllability and observability Gramians, $\mathbf{W}_c$ and $\mathbf{W}_o$, respectively, are obtained as solutions of the generalised controllability and observability algebraic Lyapunov equations (ALEs) [41]. A balanced realization is characterized by $\mathbf{W}_{b,c} = \mathbf{W}_{b,o} = \mathrm{diag}(\sigma_1, \ldots, \sigma_n)$, with σ being the so-called Hankel singular values (HSVs).

Fig. 4.4 plots the HSVs of the linear continuous-time state-space model with $n = 938$ states, which allows choosing a suitable order for the ROM. Note that HSVs correspond to the singular values of the product of the controllability and observability Gramians. As seen, the approximation error decreases with the number of states and discarding the last ~ 120 states has little impact on the approximation error, as they all have a small contribution to the system's input-output behaviour. The order of the reduced-order model is selected based on the desired fidelity. For the wind turbine application, it is of interest that the reduced-order model shows a good agreement with the full model in the frequency range below approximately 2 Hz. Therefore, the chosen order of the ROM is $r = 55$ states, which allows capturing the system's relevant dynamics whilst reducing its complexity. The benefit of reducing the full model is mainly using lower storage requirements and running simulations with much lower computation times.

Furthermore, as it has never been of interest in modal and stability analysis, the rotor rotation rigid body mode is not currently precisely represented in the BHawC linearised model. As a result, it can happen that this mode does not have exactly zero damping as is to be expected, and consequently, the system can appear unstable due to this mode. Therefore, in the present work, the rigid body mode is removed during the model reduction step. The removal of the rigid body mode means that this mode cannot be used to represent the variation of the rotor speed due to variations in the aerodynamic force.

Various tools are available to compute reduced-order approximations of large-scale systems while pre-

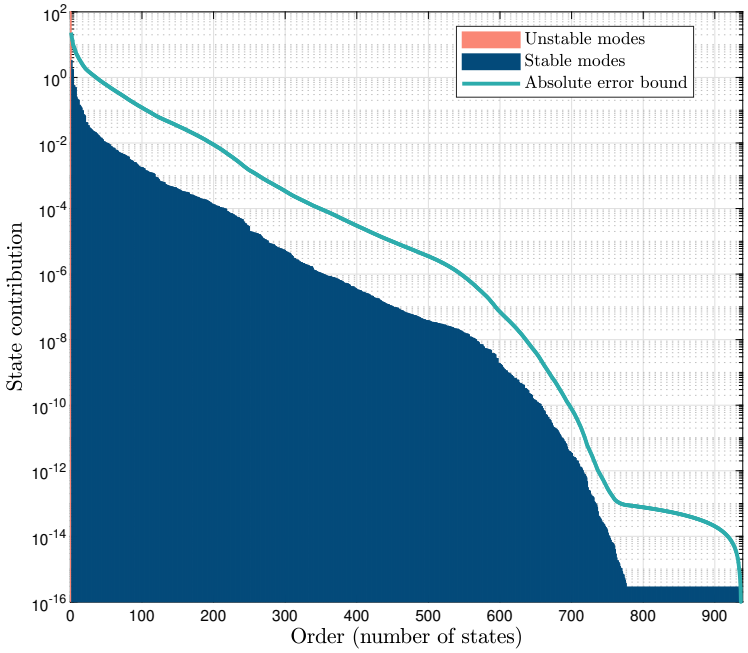

Figure 4.4: Hankel singular values and approximation error of the linear model

serving their important dynamics. For example, MATLAB® provides reduced-order modelling techniques such as balanced truncation, pole-zero simplification, and model selection methods [5]. In any case, these methods do not provide the projection matrices of the ROM, which are needed in this work to apply the methodology regarding LPV systems (see Chapter 6). Also, they are not explicitly developed for sparse models and thus require transforming the sparse matrices from sparse to full (or dense) storage. Consequently, for this study, the high-order model is reduced using the `sssMOR` [21] toolbox in MATLAB®, developed by the Chair of Automatic Control (TUM) for the model reduction of large-scale dynamical systems in a sparse state-space representation. As a result, it allows exploiting the sparsity of the system to achieve approximations of the full-order dynamics while drastically reducing the memory and computational requirements involved in the simulations [1]. It also provides the ROM projection matrices and can decompose the model into its stable and unstable parts to, for instance, remove a specific mode, i.e the rigid body mode.

4.3.1. Comparison between the FOM and the ROM

The dynamic behaviour of the reduced-order model is compared against that of the full system to evaluate its performance and to verify it contains all the information needed to describe the model. The two cases shown in Figs. 4.5 and 4.7 are studied, where the wind input used is either (a) a rectangular step function or (b) a white noise signal added to a rectangular wind step. The selected order of the ROM for this study is $r = 55$ states. Recall that the nodal displacements consist of three translations (ξ_x, ξ_y, ξ_z) and three rotations (θ_x, θ_y, θ_z) about the x_G, y_G, and z_G-axis, respectively.

Rectangular wind input

Fig. 4.5 presents the dynamic response of the displacements of the tower-top node when the system is subjected to a rectangular function wind input. The wind input steps up by 0.1 m/s at 10 s, and after 1 s, it returns to the initial value. The direction of the wind inflow is aligned with the rotor axis. Here, the simulations run for 120 s using a mean hub-height wind speed of 10 m/s. As seen, the dominant motions are the displacement in the longitudinal direction ξ_y and the fore-aft rotation θ_x. The dynamic response of the reduced-order model is in good agreement with that of the full system since the time series of both models present a full match for all degrees of freedom.

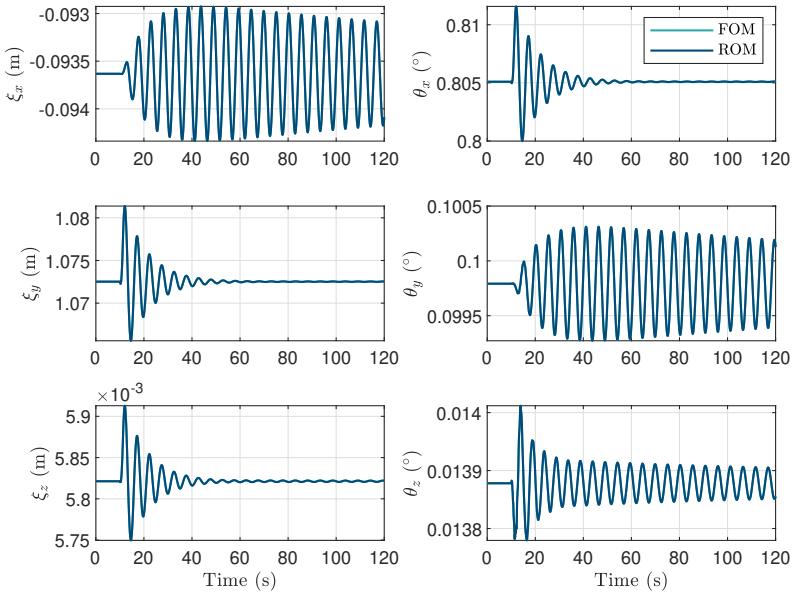

Figure 4.5: Response of the tower-top displacements under a 10 m/s rectangular wind step. Comparison between the linear ROM and the FOM

Moreover, the PSD of the dynamic response of both models is included in Fig. 4.6 to compare the responses in the frequency domain. The energy levels of the FOM are correctly captured in the ROM, especially for frequencies under approximately 2.5 Hz. Again, the DOF for which both the time-domain and the frequency-domain response differs the most is the rotation about the y_G-axis. For all degrees of freedom, both linear models are in good agreement, and they also match the response of the BHawC nonlinear model as seen in Appendix D.

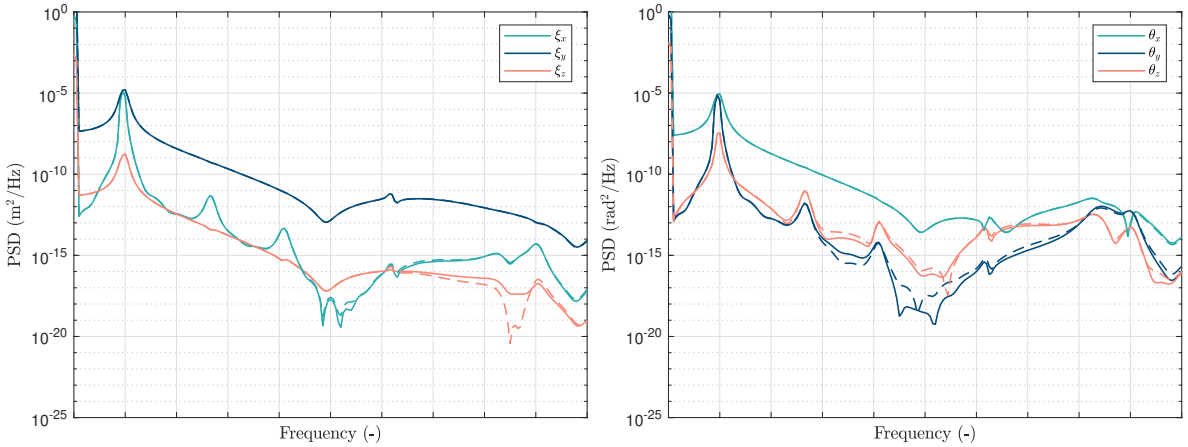

(a) PSD of the tower-top translations

(b) PSD of the tower-top rotations

Figure 4.6: PSD of the tower-top displacements under a 10 m/s rectangular wind step. Comparison between the linear ROM (dashed) and the FOM (solid)

The statistics of the responses are checked through the root-mean-square error (RMSE) normalised with the range in the solution, i.e. the maximum value minus the minimum. For all degrees of freedom, the RMSE is smaller than 0.1%. For the PSD, the error is smaller than 1×10^{-6}% in all cases. Therefore, in general, we see that the reduced-order system approximates the original system satisfactorily.

White noise rectangular wind input

The wind input signal is assumed to be a noise signal with a flat power spectrum (white noise) added to a rectangular step function; the white noise is low-pass filtered with a Butterworth filter having the cutoff frequency at 2 Hz. Fig. 4.7 depicts the time response of the displacements of the tower-top node for the full system and the ROM. The simulations run for 120 s with a mean hub-height wind speed of 27 m/s. Both signals are in good agreement throughout the simulation and for all degrees of freedom. Nevertheless, the longitudinal translation ξ_y and the fore-aft rotation θ_x slightly differ from displacements of the full system. A similar response occurs for the vertical translation ξ_z.

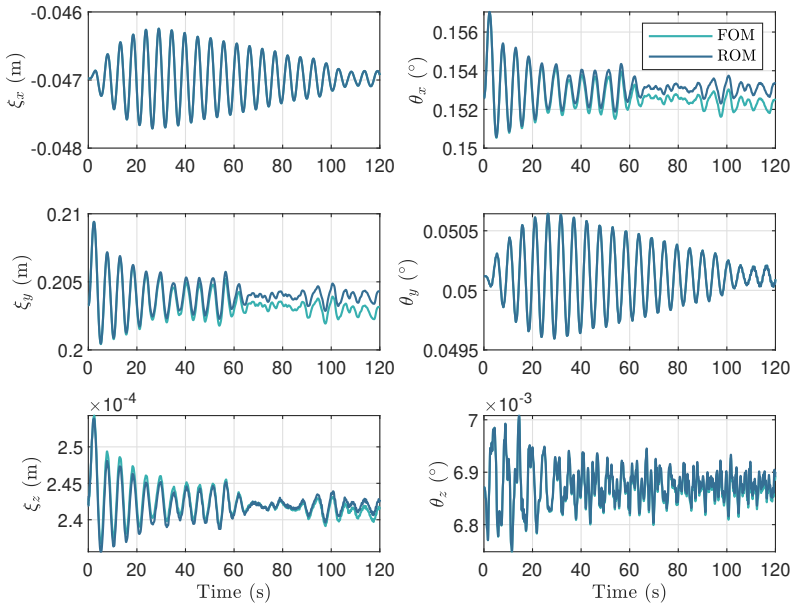

Figure 4.7: Response of the tower-top displacements under a 27 m/s white noise rectangular wind step. Comparison between the linear ROM and the FOM

Moreover, the frequency-domain comparison of both models is presented in Fig. 4.8 through the power spectral density (PSD) of the tower-top response. The energy content is preserved in the frequency range of interest for all degrees of freedom. Besides, the energy difference in the vertical translation and the fore-aft rotation is apparent. In general, the ROM adequately captures the dynamics of the system.

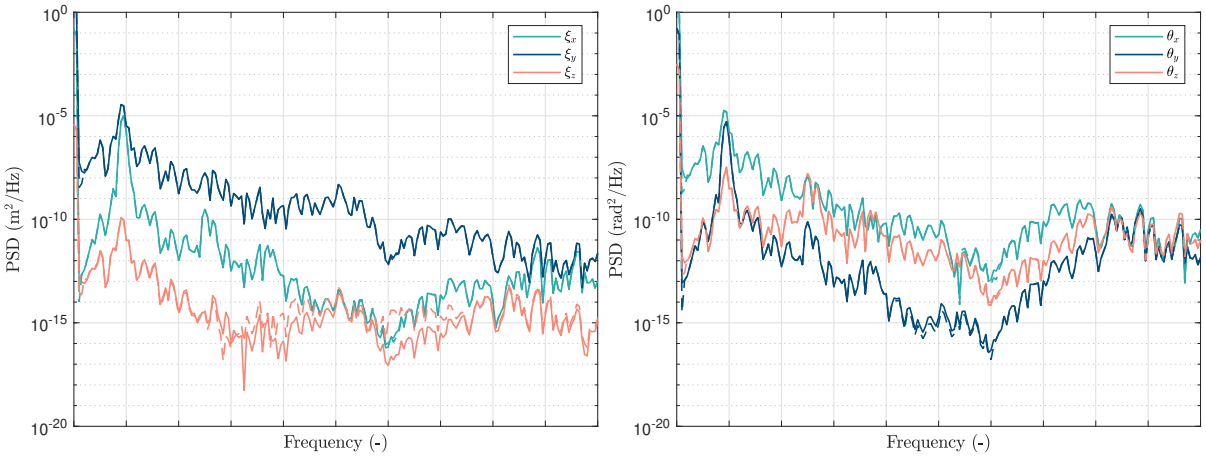

(a) PSD of the tower-top translations

(b) PSD of the tower-top rotations

Figure 4.8: PSD of the tower-top displacements under a 27 m/s white noise rectangular wind step. Comparison between the linear ROM (dashed) and the FOM (solid)

Similarly, to quantify the difference between the ROM and the full system, the root-mean-square error (RMSE) of both the dynamic response and the PSD of the simulations using a white noise input. In this case, the error regarding the tower-top displacements is under 5%. Besides, it is smaller than 0.001% for the PSDs. In conclusion, based on the time-series and the power spectra, the ROM contains the main information and yields a good approximation of the FOM.

5

Isotropic system with low turbulence intensity

A wind turbine system in isotropic conditions is characterised by having an isotropic rotor and being subject to isotropic environment conditions [32]. In such conditions, the time-periodic set of equations of motion can be transformed into time-invariant equations through a coordinate transformation, the so-called Coleman transformation. In doing so, the system can be modelled as a linear time-invariant (LTI) system and its behaviour studied in the frequency domain. This chapter begins by presenting the specific LTI system derived from the BHawC aeroelastic model (see Section 5.1). Moreover, Section 5.2 describes the transfer function approach followed to get the loads on isotropic wind turbines in low turbulence intensity wind inflow. Finally, while Section 5.3 shows some results for the analytical wind turbine model, Section 5.4 provides several simulations to determine the performance of the linearised model.

5.1. Linear time-invariant (LTI) system

To build the linear time-invariant (LTI) system at a given operating point, the T-periodic tangent mass $\mathbf{M}$, damping $\mathbf{C}$, and stiffness $\mathbf{K}$ matrices from the linearised structural model are exported from BHawC at a single azimuth angle. Then, combined with the *Coleman transformation*, the resulting system yields a linear time-invariant (LTI) system.

5.1.1. Coleman transformation

As mentioned above, the Coleman [51] transformation can be used to represent a time-periodic system using a time-invariant formulation. Specifically, for three-bladed wind turbines, it describes the motion of the rotor in the inertial frame of reference [43] through multi-blade coordinates (MBCs), designating the collective, cosine-cyclic, and sine-cyclic modes. Below, the procedure followed to obtain the linear time-invariant (LTI) formulation of the state-space model is described. In addition, Appendix B gives further details on the transformation of the system into multi-blade coordinates.

State equations

The equations of motion in global coordinates of a wind turbine dynamic system linearised about a periodic steady-state are expressed as:

$$\mathbf{M}(t)\ddot{\mathbf{q}} + \mathbf{C}(t)\dot{\mathbf{q}} + \mathbf{K}(t)\mathbf{q} = \mathbf{F}(t)\mathbf{u} \tag{5.1}$$

where $\mathbf{q} = [\boldsymbol{\rho}^\top, \boldsymbol{\theta}^\top]^\top$ is the perturbation to the vector of the system positions and orientations described in the global frame, $\mathbf{M}$, $\mathbf{C}$, and $\mathbf{K}$ are the T-periodic mass, damping and stiffness matrices composed by the structural and the steady aerodynamic matrices, $\mathbf{F}$ is the external forcing vector, and $\mathbf{u}$ is the perturbation to the wind inflow.

In the lines of the work by Skjoldan [32], the Coleman transformation needs the blade degrees of freedom to be equal in their respective local blade coordinate system. Consequently, the equations of motion of the wind turbine must be first transformed into substructure coordinates $\mathbf{q}_\mathrm{T}$ as:

$$\begin{aligned} \mathbf{q} &= \mathbf{T}\,\mathbf{q}_\mathrm{T} \\ \mathbf{T} &= \mathbf{diag}\left(\mathbf{I}_{N_\mathrm{s}}, \mathbf{T}_\mathrm{r}, \mathbf{T}_{\mathrm{b}1},\ \mathbf{T}_{\mathrm{b}2},\ \mathbf{T}_{\mathrm{b}3}\right) \end{aligned} \tag{5.2}$$

where the T-periodic matrix block diagonal matrix $\mathbf{T}$ includes the identity matrix $\mathbf{I}_{N_\mathrm{s}}$ sized by the number of degrees of freedom of the tower, nacelle, and drive-train, $\mathbf{T}_\mathrm{r}$ transforming the degrees of freedom on the shaft and hub into a hub centre frame, and $\mathbf{T}_{\mathrm{b}j}$ transforming the degrees of freedom on blade number $j = 1, 2, 3$ into a local frame for blade j [32].

Then, the aeroelastic system is transformed into the inertial frame structural degrees of freedom $\boldsymbol{\zeta}$ as

$$\begin{aligned} \mathbf{q}_\mathrm{T} &= \mathbf{B}_\mathrm{q}\,\boldsymbol{\zeta} \\ \mathbf{B}_\mathrm{q} &= \mathbf{diag}\left(\mathbf{I}_{N_\mathrm{s}}, \mathbf{B}_\mathrm{r}, \mathbf{B}_\mathrm{b}\right) \end{aligned} \tag{5.3}$$

where the structural inertial frame transformation matrix $\mathbf{B}_\mathrm{q}$ is composed of the Coleman transformation of the blade degrees of freedom $\mathbf{B}_\mathrm{b}$, and a simple rotational transformation $\mathbf{B}_\mathrm{r}$ of the shaft [32]. The periodic Coleman transformation matrix comprises blocks of Eq. (2.19) for each set of three corresponding degrees of freedom or state variables. In short, the transformation is only applied to those quantities that are specified in the rotating frame, whereas the signals specified in the inertial frame are left unchanged.

As explained in depth in Appendix B, the equations of motion of the aeroelastic system in the inertial frame of reference become:

$$\mathbf{M}_\mathrm{B}\,\dot{\tilde{\boldsymbol{\zeta}}} + (\mathbf{C}_\mathrm{B} + \mathbf{M}_\mathrm{B}\bar{\boldsymbol{\omega}})\,\tilde{\boldsymbol{\zeta}} + \mathbf{K}_\mathrm{B}\,\boldsymbol{\zeta} = \mathbf{F}_\mathrm{B}\mathbf{u}_\mathrm{B} \tag{5.4}$$

where $\tilde{\boldsymbol{\zeta}} = \dot{\boldsymbol{\zeta}} + \bar{\boldsymbol{\omega}}\boldsymbol{\zeta}$, with $\bar{\boldsymbol{\omega}} = \mathbf{B}_\mathrm{q}^{-1}\,\dot{\mathbf{B}}_\mathrm{q}$ being a constant matrix, $\mathbf{u}_\mathrm{B}$ is the wind input in the non-rotating frame, and the Coleman-transformed mass, damping/gyroscopic, stiffness, and external force matrices are, respectively,

$$\mathbf{M}_\mathrm{B} = \mathbf{B}_\mathrm{q}^{-1}\mathbf{T}^\top\mathbf{M}\mathbf{T}\mathbf{B}_\mathrm{q} \tag{5.5a}$$

$$\mathbf{C}_\mathrm{B} = \mathbf{B}_\mathrm{q}^{-1}\mathbf{T}^\top(\mathbf{C}\mathbf{T} + 2\mathbf{M}\dot{\mathbf{T}})\mathbf{B}_\mathrm{q} \tag{5.5b}$$

$$\mathbf{K}_\mathrm{B} = \mathbf{B}_\mathrm{q}^{-1}\mathbf{T}^\top(\mathbf{K}\mathbf{T} + \mathbf{C}\dot{\mathbf{T}} + \mathbf{M}\ddot{\mathbf{T}})\mathbf{B}_\mathrm{q} \tag{5.5c}$$

$$\mathbf{F}_\mathrm{B} = \mathbf{B}_\mathrm{q}^{-1}\mathbf{T}^\top\mathbf{F}\,. \tag{5.5d}$$

Similarly, in general, the wind input is transformed into the non-rotating frame of reference $\mathbf{u}_\mathrm{B}$. Nevertheless, for the case being, the input to the system is already described with the ground-fixed reference frame. Specifically, the wind inflow is extracted from a turbulence grid box in the wind coordinates system and transformed into the global coordinate frame.

Output equations

Particularly, the output of the wind turbine dynamic system corresponds to the internal loads on the structure. Hence, the linearised output equations are obtained through a matrix relating the nodal displacements in the ground-fixed frame to the internal loads as explained fully in Section 4.2.3. In general, a similar procedure to that in the state equations is followed to describe the output of the system in the non-rotating frame. This process requires two steps: first converting the degrees of freedom to substructure coordinates and then applying the Coleman transformation to the system. Appropriately, the

output equation expressed in the non-rotating frame reads:

$$\mathbf{y}_{gf} = \mathbf{H}_{\mathrm{B}}\boldsymbol{\zeta} \tag{5.6}$$

Nevertheless, as indicated in Section 4.2.3, for this study, the output matrix is already expressed with respect to the global frame of reference. Accordingly, the output matrix of the Coleman-transformed system yields $\mathbf{H}_{\mathrm{B}} = \mathbf{H}$.

Last, note that the output of the state-space model $\mathbf{y}_{gf}$ corresponds to the perturbation to the outputs about the steady-state equilibrium, as seen in Eq. (4.6). Therefore, to get the actual response of the system, the steady-state solution $\tilde{\boldsymbol{\gamma}}_{gf}$ must be added to the output as:

$$\boldsymbol{\gamma}_{gf}(t) = \mathbf{y}_{gf} + \tilde{\boldsymbol{\gamma}}_{gf}\,. \tag{5.7}$$

In the linearised BHawC model, the steady-state solution for the load channels is extracted from the internal forces in element coordinates and transformed into the global frame of reference.

5.1.2. State-space representation

Once transformed into the non-rotating frame, the wind turbine dynamic system can be represented in the state-space formulation as explained in Section 4.2. Thus, rearranging the system equations and considering the equality $\dot{\tilde{\boldsymbol{\zeta}}} = \dot{\tilde{\boldsymbol{\zeta}}}$ yields the state-space formulation as:

$$\dot{\mathbf{x}}(t) = \mathbf{A}\mathbf{x}(t) + \mathbf{B}\mathbf{u}_{\mathrm{B}}(t) \tag{5.8a}$$

$$\mathbf{y}_{gf}(t) = \mathbf{C}\mathbf{x}(t) + \mathbf{D}\mathbf{u}_{\mathrm{B}}(t) \tag{5.8b}$$

where the inertial frame state vector $\mathbf{x} = [\boldsymbol{\zeta}^{\top}\ \tilde{\boldsymbol{\zeta}}^{\top}]^{\top}$ comprises the inertial frame nodal displacements and velocities, $\mathbf{y}_{gf}$ is the system response in the ground-fixed reference, and the inertial frame model matrices derived from linear second-order equations of motion (see Eq. (5.4)) are

$$\mathbf{A} = \begin{bmatrix} -\tilde{\boldsymbol{\omega}} & \mathbf{I} \\ -\mathbf{M}_{\mathrm{B}}^{-1}\mathbf{K}_{\mathrm{B}} & -\mathbf{M}_{\mathrm{B}}^{-1}\mathbf{C}_{\mathrm{B}} - \tilde{\boldsymbol{\omega}} \end{bmatrix} \tag{5.9a}$$

$$\mathbf{B} = \begin{bmatrix} \mathbf{0} \\ \mathbf{M}_{\mathrm{B}}^{-1}\mathbf{F}_{\mathrm{B}} \end{bmatrix} \tag{5.9b}$$

$$\mathbf{C} = \begin{bmatrix} \mathbf{H}_{\mathrm{B}} & \mathbf{0} \end{bmatrix} \tag{5.9c}$$

$$\mathbf{D} = \mathbf{0}\,. \tag{5.9d}$$

which use Eqs. (5.5a) to (5.5d) for the Coleman transformed mass, damping, stiffness, and external force matrices.

To summarise, applying the Coleman transformation to the time-periodic system at a given operating point results in a linear time-invariant (LTI) model. Nevertheless, bear in mind that this is only applicable for wind turbines in isotropic conditions. As explained above, an LTI model is characterised by having equations of motion with constant coefficients. Consequently, the state-space representation of the system in Eq. (5.8) has constant matrices, described by Eqs. (5.9a) to (5.9d).

5.1.3. Model order reduction

The full state-space model is a MIMO system defined by a large number of state variables ($n = 938$), and inputs ($n_i = 540$). Therefore, calculating the transfer function of the system comes at the expense of a high computation cost. The model reduction technique used is known as the *balanced truncation* (BT) method, which allows to cut down the simulation times by reducing the complexity (order) of the system. The balanced truncation approach is based on the idea of finding a model representation in which (a) every state is as controllable as it is observable, and (b) the state variables with the slightest

contribution to the input-output behaviour are removed [17]. In summary, first, a state transformation brings the system into a balanced representation to straightforwardly identify the negligible state variables. Then, the reduced model is obtained by truncation of the full system.

Balancing

To find the directions that are as well controllable as observable, a state transformation of the form $\mathbf{x}_b = \mathbf{T}\mathbf{x}$ is introduced [39], where $\mathbf{x}$ and $\mathbf{x}_b$ are the original and the new state variables, respectively. Then, the state coordinate transformation produces the equivalent model:

$$\begin{aligned} \dot{\mathbf{x}}_b &= \mathbf{T}\mathbf{A}\mathbf{T}^{-1}\mathbf{x}_b + \mathbf{T}\mathbf{B}\mathbf{u} \\ \mathbf{y}_{gf} &= \mathbf{C}\mathbf{T}^{-1}\mathbf{x}_b + \mathbf{D}\mathbf{u} \end{aligned} \tag{5.10}$$

and transforms the controllability and observability Gramians to $\mathbf{W}_{b,c} = \mathbf{T}\mathbf{W}_c\mathbf{T}^\top$ and $\mathbf{W}_{b,o} = \mathbf{T}^{-\top}\mathbf{W}_o\mathbf{T}^{-1}$.

For a balanced system, all state variables as just as well controllable as observable. Hence, $\mathbf{T}$ is a transformation for which both Gramian matrices become equal diagonal matrices that have the Hankel singular values (HSVs) as entries:

$$\mathbf{W}_{b,c} = \mathbf{W}_{b,o} = \mathrm{diag}(\sigma_1, \sigma_2, \ldots, \sigma_n) \tag{5.11}$$

with $\sigma_1 \geq \sigma_2 \geq \cdots \geq \sigma_n$ reflecting the combined controllability and observability of the individual states of the balanced model.

As the HSVs are ordered according to their importance for the input-output behaviour, the balanced representation of the system allows us to pinpoint which state variables can be neglected in the simplified model [17]. In short, the small entries of Hankel singular values indicate the states that can be removed to form the reduced-order model (ROM).

Truncation

Once the balanced representation of the system is determined, the system can be reduced by partitioning it into two blocks:

$$\begin{aligned} \begin{bmatrix} \dot{\mathbf{x}}_{b,1} \\ \dot{\mathbf{x}}_{b,2} \end{bmatrix} &= \begin{bmatrix} \mathbf{A}_{11} & \mathbf{A}_{12} \\ \mathbf{A}_{21} & \mathbf{A}_{22} \end{bmatrix} \begin{bmatrix} \mathbf{x}_{b,1} \\ \mathbf{x}_{b,2} \end{bmatrix} + \begin{bmatrix} \mathbf{B}_1 \\ \mathbf{B}_2 \end{bmatrix} \mathbf{u} \\ \mathbf{y}_{gf} &= \begin{bmatrix} \mathbf{C}_1 & \mathbf{C}_2 \end{bmatrix} \begin{bmatrix} \mathbf{x}_{b,1} \\ \mathbf{x}_{b,2} \end{bmatrix} + \begin{bmatrix} \mathbf{D}_1 \\ \mathbf{D}_2 \end{bmatrix} \mathbf{u} \end{aligned} \tag{5.12}$$

The states variables $\mathbf{x}_{b,1}$ are those retaining the most important input-output characteristics of the original system, while $\mathbf{x}_{b,2}$ are those with the smallest HSVs. The latter can, therefore, be neglected, as they contribute little to the energy transfer from input to output [39]. By truncating the $\mathbf{x}_{b,2}$ state variables, the reduced system reads:

$$\begin{aligned} \dot{\mathbf{x}}_{b,1} &= \mathbf{A}_{11}\mathbf{x}_r + \mathbf{B}_1\mathbf{u} \quad &\rightarrow \quad \dot{\mathbf{x}}_r &= \mathbf{A}_r\mathbf{x}_r + \mathbf{B}_r\mathbf{u} \\ \mathbf{y}_{gf} &= \mathbf{C}_1\mathbf{x}_r + \mathbf{D}_1\mathbf{u} \quad &\rightarrow \quad \mathbf{y}_{gf} &= \mathbf{C}_r\mathbf{x}_r + \mathbf{D}_r\mathbf{u} \end{aligned} \tag{5.13}$$

Consequently, the reduced model is also balanced and has diagonal Gramians matrices with the largest HSVs as entries. The model reduction method used is the balanced truncation (BT), as it preserves stability and is suitable for models with up to $n = 5000$ states [17]. BT can be interpreted as a Petrov-Galerkin projection onto the subspaces $\mathbf{V}$ and $\mathbf{W}$ such that the states are approximated as $\mathbf{x} \approx \mathbf{V}\mathbf{x}_r$, where $\mathbf{x}_r$ is the new state-space coordinate system. Since the projection subspaces are biorthogonal ($\mathbf{W}^\top\mathbf{V} = \mathbf{I}$), the matrices of reduced system result in:

$$\mathbf{A}_r = \mathbf{W}^\top\mathbf{A}\mathbf{V}, \quad \mathbf{B}_r = \mathbf{W}^\top\mathbf{B}, \quad \mathbf{C}_r = \mathbf{C}^\top\mathbf{V}, \quad \mathbf{D}_r = \mathbf{D}\,. \tag{5.14}$$

In conclusion, the reduced-order model yields from eliminating the states that are simultaneously difficult to reach and difficult to observe. For this study, the selected order of the ROM is $r = 55$ states, as previously discussed in Section 4.3.

5.2. Frequency-domain analysis

For an isotropic rotor subject to isotropic external conditions, the Coleman-transformed model is characterised by being a linear time-invariant (LTI) system. Therefore, a convenient way of representing the system is in terms of the *transfer function*, which describes the system's input-output relation and can easily provide its response to any wind input. While time-domain analysis displays the temporal evolution of the system response over time, the frequency-domain analysis depicts the "amount" of a signal existing within a given frequency band in a range of frequencies. The latter contains the information about both the magnitude and phase of the signal at each frequency [7].

Fig. 5.1 presents the block diagram of the workflow to compute the loads on the wind turbine, starting from the wind sampling and the linear state-space model. First, the wind input in the frequency domain $\mathbf{U}_\mathrm{B}(\omega)$ is obtained by applying the fast Fourier transform (FFT) to the sampled wind speeds $\mathbf{u}_\mathrm{B}(t)$ at the aerodynamic calculation points. Besides, the transfer function of the linear model is obtained by equating the time-invariant state-space matrices $\mathbf{A}$, $\mathbf{B}$, $\mathbf{C}$, $\mathbf{D}$. Then, the wind turbine response in the ground-fixed reference frame $\mathbf{Y}_{gf}(\omega)$ is obtained by combining the wind input in the frequency domain with the system's transfer functions. Finally, the loads in the blade-fixed frame in the time domain $\mathbf{y}_{bf}(t)$ can be obtained by applying both the Coleman transformation in the frequency domain and the inverse fast Fourier transformation (IFFT).

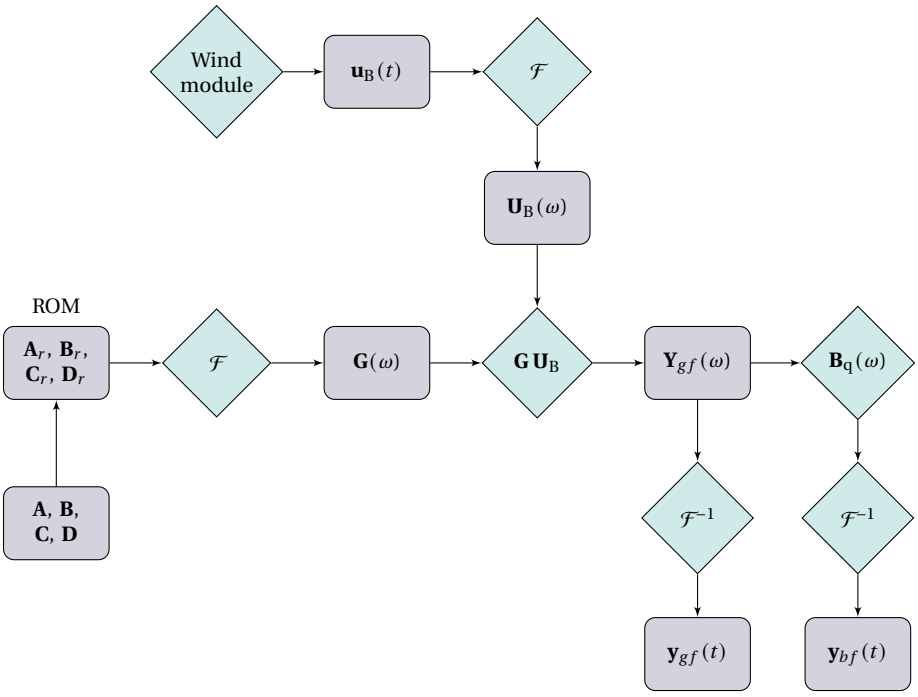

Figure 5.1: Block diagram of the workflow to compute the time-domain response starting from the linear system equations and the sampled wind

5.2.1. Wind input

In the wind turbine model described by Eq. (5.8), the free wind speed acts as an input to the system through the input matrix $\mathbf{B}$. Therefore, to evaluate the response of the linear model, the wind speed vector $\mathbf{u}_\mathrm{B}$ is used as the input to the system [26]. Specifically, $\mathbf{u}_\mathrm{B}$ refers to the free wind speed at the aerodynamic calculation points located along the blades, expressed in the non-rotating reference frame.

The time series of the free wind at each aerodynamic section are obtained by interpolating their positions during the entire simulation with the turbulence box, generated through a Mann turbulence model. First, the positions of the aerodynamic calculation points are computed in time using a constant rotor speed throughout the simulation and by assuming that the blade and tower deformations

do not affect the turbulence plane to be sampled. Then, the turbulence components for each spatial position in time are obtained by cubic spline interpolation of the turbulence box. In brief, the input to the state-space model results in a collection of the turbulent wind speeds at the aerodynamic sections of the wind turbine blades:

$$\mathbf{u}_{\mathrm{B}}(t) = \left[\mathbf{u}_{w,1}^{\top}(t) \quad \mathbf{u}_{w,2}^{\top}(t) \quad \dots \quad \mathbf{u}_{w,n_{aero}}^{\top}(t)\right]^{\top} . \tag{5.15}$$

Wind model

For turbulent wind simulations, the turbulence box of the linear model is computed by an external dynamic-link library (DLL) written in MATLAB® as a MEX file, which reproduces the BHawC internal turbulence generation and scaling process. Thereby, the wind module DLL is used to request the wind speed at each specific coordinate. The turbulence box specifications in the DLL are set equal to those in the BHawC simulations to ensure both models receive matching wind speeds. Some of the input parameters for the generation of the three-dimensional turbulent wind fields are the average hub-height wind speed, desired turbulence intensity, number of grid points in the longitudinal, transversal, and vertical directions, grid dimensions (width and height), and simulation length and time step.

Fig. 5.2 shows the time series of the wind speed fluctuations using a 12 m/s hub-height mean and 5% turbulence intensity. The grid boxes use a ratio of turbulence intensity in the longitudinal, transverse, and vertical directions of 1, 0.8, and 0.5, respectively. The time series at two points in the turbulence box are plotted to compare both methods, the wind module DLL and the BHawC simulation results. While Fig. 5.2a shows the turbulent wind at the hub in the transversal direction, Fig. 5.2b illustrates the time series at a different point in the box in the longitudinal direction. As seen, the time series generated in the wind module fully match those in BHawC. The component of the turbulent wind in the vertical direction is not shown as it presents a similar behaviour as the two other components when compared to the BHawC time series.

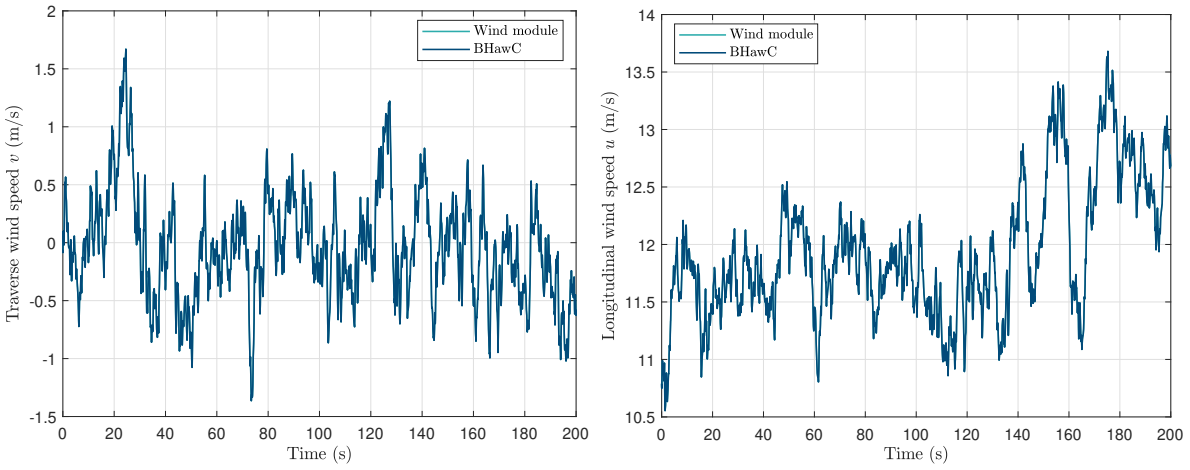

(a) Wind speed at the hub in the transversal direction

(b) Wind speed at a point in the longitudinal direction

Figure 5.2: Turbulent wind speeds at 12 m/s hub-height wind speed and 5% turbulence intensity. Comparison between the wind module DLL and BHawC

In summary, this methodology provides the turbulent wind speeds at the aerodynamic calculation points $\mathbf{u}_{\mathrm{B}}(t)$ sampled in time using a dynamic link library for the turbulent wind generation over time. Finally, the wind speed input in the frequency domain is computed by evaluating the fast Fourier transform (FFT) of the wind signals. Hence, in the linear model, the wind input in the frequency domain at all aerodynamic sections expressed in the ground-fixed reference frame is:

$$\mathbf{U}_{\mathrm{B}}(\omega) = \mathcal{F}\left[\mathbf{u}_{\mathrm{B}}\right] . \tag{5.16}$$

5.2.2. Transfer function

The transfer function operator is obtained by taking the Laplace transform of the state-space model assuming zero initial conditions, as previously illustrated in Section 2.2.2. Interpreting the Laplace operator $s = j\omega$ as a complex frequency, the state-space formulation of the linear model in the frequency-domain reads:

$$j\omega \mathbf{X}_r(\omega) = \mathbf{A}_r \mathbf{X}_r(\omega) + \mathbf{B}_r \mathbf{U}_\mathrm{B}(\omega) \tag{5.17a}$$

$$\mathbf{Y}_{gf}(\omega) = \mathbf{C}_r \mathbf{X}_r(\omega) + \mathbf{D}_r \mathbf{U}_\mathrm{B}(\omega) \tag{5.17b}$$

Recall that $\mathbf{A}_r$, $\mathbf{B}_r$, $\mathbf{C}_r$, $\mathbf{D}_r$ are the Coleman-transformed (time-invariant) matrices of the ROM, and $\mathbf{X}_r$ and $\mathbf{Y}_{gf}$ are system states and outputs, defined in the ground-fixed frame and expressed in the frequency domain.

Fig. 5.1 illustrates the procedure followed to get the transfer function of the system $\mathbf{G}(\omega)$. As seen, by equating the state and output equations, the transfer function between the wind speed at the aerodynamic sections and the wind turbine output can be evaluated as [26]:

$$\mathbf{G}(\omega) = \mathbf{C}_r (j\omega \mathbf{I} - \mathbf{A}_r)^{-1} \mathbf{B}_r + \mathbf{D}_r \tag{5.18}$$

where $j := \sqrt{-1}$ is the imaginary number, ω is the angular frequency, and $\mathbf{I}$ is the identity matrix.

Below, the different approaches explored to get the transfer function of the system are described. Although the methods are explained with regard to the full state-space systems, the same methodology can be extended to deal with reduced-order models.

MATLAB® implementation

The numerical approach used to get the transfer function involves looping over an array of frequencies and using Eq. (5.18) to determine the transfer function operator $\mathbf{G}(\omega)$. Since $\mathbf{G}(\omega)$ is calculated for many different values of frequency ω, the computation yields a fairly expensive one. In the process, the operation that requires most computational cost is getting $(j\omega\mathbf{I} - \mathbf{A})^{-1}\mathbf{B}$, which is equivalent to solving the system [42]:

$$(j\omega\mathbf{I} - \mathbf{A})^{-1} \mathbf{x}^* = \mathbf{B} \tag{5.19}$$

where $\mathbf{x}^*$ is the solution vector.

Nevertheless, since matrix $j\omega\mathbf{I} - \mathbf{A}$ is the same for each value of frequency, it is factored into LU just once [42], meaning the same factorisation can be used to solve the entire $\mathbf{G}(\omega)$ matrix. To reduce the computational times, the method proposed by Laub [49] and later employed by Tibaldi [26] is used, which allows for efficiently computing the system's transfer function. The approach is based on initially transforming the system matrix $\mathbf{A}$ to Hessenberg form. Accordingly, prior to computing of the transfer function, $\mathbf{A}$ is reduced to an upper Hessenberg matrix $\mathbf{H}$, such that $\mathbf{P}^\top \mathbf{A} \mathbf{P} = \mathbf{H}$. Then, the transfer function operator yields

$$\mathbf{G}(\omega) = \mathbf{C} \left(j\omega\mathbf{I} - \mathbf{A}\right)^{-1} \mathbf{B} = \mathbf{C}\mathbf{P} \left(j\omega\mathbf{I} - \mathbf{H}\right)^{-1} \mathbf{P}^\top \mathbf{B}\,, \tag{5.20}$$

which allows to compute the upper Hessenberg matrix $\mathbf{H}$, $\mathbf{B}' = \mathbf{P}^\top \mathbf{B}$, and $\mathbf{C}' = \mathbf{C}\mathbf{P}$ just once for all values of frequency. Algorithm 1 shows the algorithm to compute the transfer function of the state-space system based on the Hessenberg algorithm mentioned above.

PETSc implementation

As already stated, the full state-space model is a large system, making the computation of its transfer function a time-consuming process which requires large quantities of data. To speed up the computation, the Portable, Extensible Toolkit for Scientific Computation (PETSc) [4] is used on a high-performance computer for the numerical solution of the transfer function $\mathbf{G}(\omega)$. A prototype of the PETSc implementation is developed in the C++ programming language. Fig. 5.3 shows the workflow to compute the transfer function using the software tools in PETSc.

Algorithm 1: Computation of the transfer function based on a Hessenberg algorithm

Input: State $\mathbf{A}$, input $\mathbf{B}$, output $\mathbf{C}$, and feedforward $\mathbf{D}$ matrices, and frequency ω
Output: Transfer function $\mathbf{G}(\omega) = \mathbf{C}\,(j\omega\mathbf{I} - \mathbf{A})^{-1}\,\mathbf{B} + \mathbf{D}$

1 Transform $\mathbf{A}$ to an upper Hessenberg matrix $\mathbf{H}$
2 Compute $\mathbf{B}' = \mathbf{P}^{\top}\mathbf{B}$ and $\mathbf{C}' = \mathbf{C}\mathbf{P}$
3 **foreach** *Frequency* $\omega_i = 0 : \omega_{\max}$ **do**
4 Solve the Hessenberg system:

$$(j\omega_i\mathbf{I} - \mathbf{H})\,\mathbf{x}^* = \mathbf{B}' \tag{5.21}$$

5 Compute the transfer function $\mathbf{G}(\omega_i) = \mathbf{C}'\mathbf{x}^* + \mathbf{D}$.

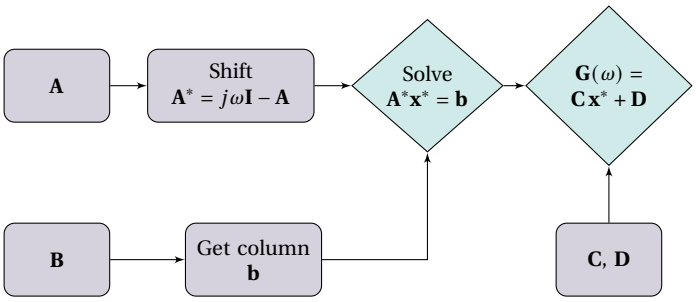

Figure 5.3: Block diagram of the workflow of the PETSc implementation to compute the transfer function for each frequency

First, the sparse matrices of the LTI system are read, and the PETSc vector and matrix objects are created. Then, the procedure in the block diagram is applied for each frequency ω in the frequency array. Thereby, the state matrix is shifted with the frequency as $\mathbf{A}^* = j\omega\mathbf{I} - \mathbf{A}$. Then, the KSP object [3] is used to solve the linear system of the form

$$\mathbf{A}^*\,\mathbf{x}^* = \mathbf{b} \tag{5.22}$$

where the right-hand-side vector is the m-th column of the input matrix $\mathbf{B}$ and $\mathbf{x}^*$ is the solution vector.

Specifically, as the system in Eq. (5.22) is an unsymmetric sparse linear system, the UMFPACK [18] routines are used for the numerical solution. Furthermore, the approach uses a direct solver based on lower-upper (LU) factorisation as a preconditioner. The linear system's solution can then be multiplied by the output matrix $\mathbf{C}$, and the result summed with the feedforward matrix $\mathbf{D}$ to get the transfer function of the system. This procedure is repeated for all the frequencies in the array.

Although PETSc provides numerical routines to compute $\mathbf{G}(\omega)$, the speed-up of the calculation is just around 1.7× with respect to the computations in MATLAB®. The reason for this is needing to loop over the columns of the input matrix to solve the linear system in Eq. (5.22) at each frequency. Recall that the $\mathbf{B}$ is a $n \times n_i$ system, being $n_i = 540$ the number of inputs to the state-space model. In view of the need to speed up the calculations, another possibility is to run the computing-intensive parts of the computation on a graphics processing unit (GPU).

5.2.3. Response

The transfer function gives the relationship between the system's input and output. Therefore, the response of the system to a given wind input is evaluated by joining the wind turbine transfer function and the wind input as [26]:

$$\mathbf{Y}_{gf}(\omega) = \mathbf{G}(\omega)\,\mathbf{U}_{\mathrm{B}}(\omega) \tag{5.23}$$

which indicates how much signal of frequency ω is contained in the original wind turbine load response measured in the ground-fixed reference frame.

Then, the frequency components of the $\mathbf{Y}_{gf}(\omega)$ response can be recombined to recover the original signal in the time domain [7]. The wind turbine's ground-fixed response is converted from the frequency-

domain signal back to the time domain by means of the inverse fast Fourier transform (IFFT). Hence,

$$\mathbf{y}_{gf}(t) = \mathcal{F}^{-1}\left[\mathbf{Y}_{gf}(\omega)\right], \quad \mathbf{y}_{gf}(t) = \frac{1}{2\pi}\int_{-\infty}^{\infty} \mathbf{Y}_{gf}(\omega)\, e^{j\omega t}\, d\omega\,. \tag{5.24}$$

On the other hand, the response in the ground-fixed reference frame $\mathbf{Y}_{bf}$ can be transformed into the blade-fixed reference frame through the frequency domain representation of the Coleman transformation, described as [10]:

$$\begin{bmatrix}\xi_1(s)\\ \xi_2(s)\\ \xi_3(s)\end{bmatrix} = \mathbf{C}_-^{\top}\begin{bmatrix}a_1\,(s-j\Omega)\\ b_1\,(s-j\Omega)\end{bmatrix} + \mathbf{C}_+^{\top}\begin{bmatrix}a_1\,(s+j\Omega)\\ b_1\,(s+j\Omega)\end{bmatrix} \tag{5.25}$$

where Ω is the rotor speed and $\mathbf{C}_-$ and $\mathbf{C}_+$ are defined as [10]:

$$\mathbf{C}_- := \frac{1}{2}\begin{bmatrix}1 & j\\ -j & 1\end{bmatrix}\begin{bmatrix}\cos\psi_1 & \cos\psi_2 & \cos\psi_3\\ \sin\psi_1 & \sin\psi_2 & \sin\psi_3\end{bmatrix}, \tag{5.26a}$$

$$\mathbf{C}_+ := \frac{1}{2}\begin{bmatrix}1 & -j\\ j & 1\end{bmatrix}\begin{bmatrix}\cos\psi_1 & \cos\psi_2 & \cos\psi_3\\ \sin\psi_1 & \sin\psi_2 & \sin\psi_3\end{bmatrix}. \tag{5.26b}$$

with the azimuthal angles of the three rotor blades being $\psi_1 = 0$ rad, $\psi_2 = \frac{2\pi}{3}$ rad, and $\psi_3 = \frac{4\pi}{3}$ rad.

Similarly, the response in the blade-fixed reference frame is reconstructed to obtain its time-domain response as:

$$\mathbf{y}_{bf}(t) = \mathcal{F}^{-1}\left[\mathbf{Y}_{bf}(\omega)\right], \quad \mathbf{y}_{bf}(t) = \frac{1}{2\pi}\int_{-\infty}^{\infty} \mathbf{Y}_{bf}(\omega)\, e^{j\omega t}\, d\omega\,. \tag{5.27}$$

Furthermore, this procedure allows to easily obtain the power spectral density (PSD) of both the ground-fixed and the blade-fixed responses. Fig. 5.4 illustrates the workflow to obtain the PSDs starting from the frequency-domain response $\mathbf{Y}_{gf}(\omega)$, which can be computed as:

$$\mathbf{\Phi}_{y,gf}(\omega) = \left|\mathbf{Y}_{gf}(\omega)\right|^2 \quad \text{and} \quad \mathbf{\Phi}_{y,bf}(\omega) = \left|\mathbf{Y}_{bf}(\omega)\right|^2. \tag{5.28}$$

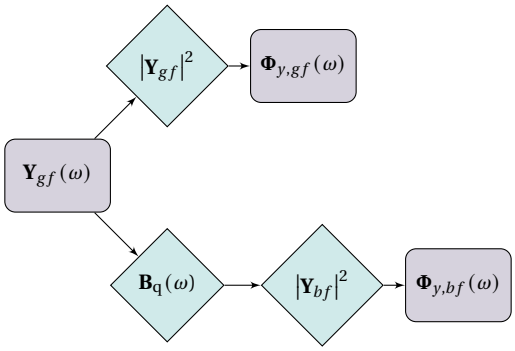

Figure 5.4: Block diagram of the workflow to compute the PSD of the time-domain response

5.3. Numerical results: analytical wind turbine model

This section compares the linear analytical wind turbine model against its nonlinear response to test the developed methodology. This study assumes an isotropic wind turbine in isotropic external conditions. Therefore, all blades have the same structural properties, and gravity field, wind shear, wind misalignment, and tower shadow are not present in the analysis. The dynamic responses of the analytical wind turbine under a steady wind speed are presented. The motion in the eight degree of freedom directions is analysed and discussed at two wind turbine operating regions: around rated and over rated wind speeds.

5.3.1. Response to a steady wind

The dynamic behaviour of the analytical wind turbine model in steady wind conditions is compared against its nonlinear response. The comparison between both models is evaluated at two operational points: 9 m/s (rated wind speed) and 20 m/s (high wind speed). The mean wind speed defines the operational conditions (pitch angle and rotor speed) of the turbine at each point. In addition, the turbine is represented in the ground-fixed coordinate system. Hence, the analysis uses multi-blade coordinates (a_0, a_1 and b_1) to represent the rotations of the flapwise and edgewise blade motions.

Figs. 5.5 and 5.6 provide the dynamic response of the simulations over 100 s. To excite all the degrees of freedom, the initial conditions of the tower fore-aft (z_H) and side-side (y_H) displacements are set to −0.1 m and 0.1 m, respectively. Specifically, setting initial values for the tower SS and FA allows exciting the rotor cosine and sine in edge and flap, respectively. The initial excitation can be seen at the first time instant, after which the degrees of freedom begin to oscillate about the steady-state. Then, the structural and aerodynamic damping causes these oscillations to dampen out towards the final equilibrium. Also, given that the wind input is an axial wind at the tower hub height, both cases are dominated by the tower fore-aft motion and the collective flapwise degree of freedom. In general, the linear model is in very good agreement with the nonlinear model as the dynamic responses fully match in both study cases.

In the time series at rated wind conditions, Fig. 5.5, the amplitude of the oscillations is much higher due to the high aerodynamic loads exerted on the system. Above rated conditions, i.e. in the time series in Fig. 5.6, the blades vary their angle so that the aerodynamic drag increases while the lift decreases and so, the output power is maintained while not damaging the turbine. Therefore, the tower-top displacements are lower. Moreover, the impact of the aerodynamic damping can be observed, where the simulations at low wind speed require a longer time to reach the final steady-state. Finally, the output of the linear model is in good agreement with the response of the nonlinear model since the time series present a full match.

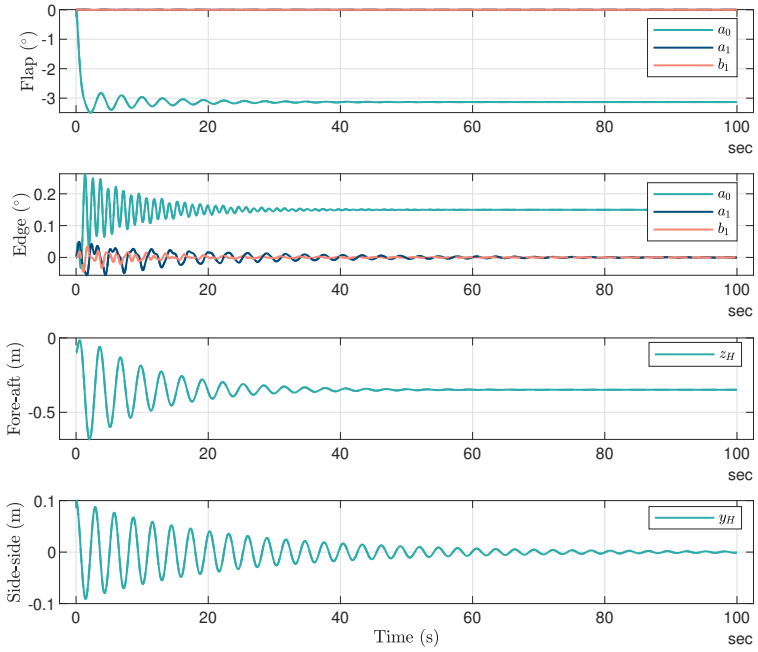

Figure 5.5: Response of the analytical WT under a 9 m/s steady wind.
Comparison between the linear model (solid) and the nonlinear model (dashed)

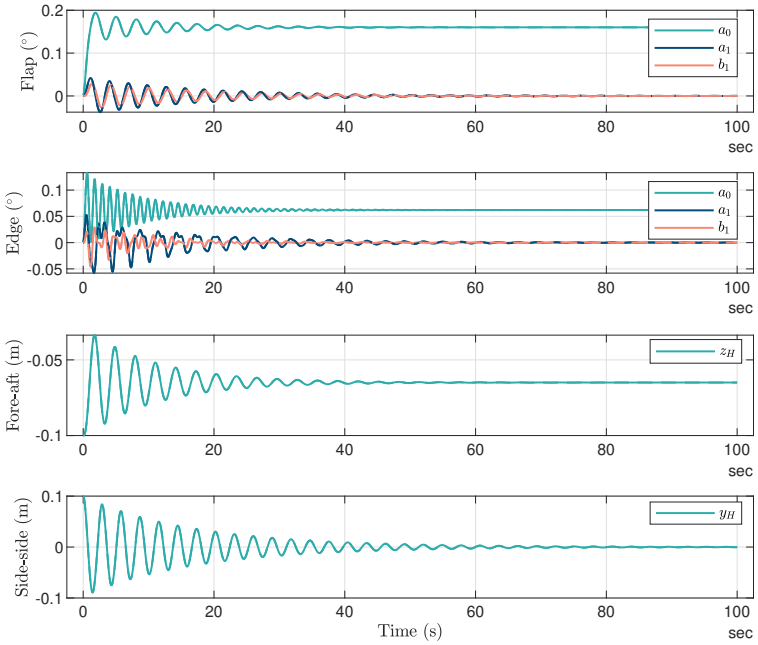

Figure 5.6: Response of the analytical WT under a 20 m/s steady wind.
Comparison between the linear model (solid) and the nonlinear model (dashed)

5.4. Numerical results: linearised BHawC model

This section presents a comparison of the linear state-space model against the nonlinear BHawC model. This study addresses isotropic wind turbines in isotropic external conditions. Hence, the nonlinear time simulations do not include gravity, wind shear, flow misalignment, and tower shadow. The comparison consists of two parts. First, Section 5.4.1 gives an overview of the computational requirements of the linear model. Then, Section 5.4.2 analyses the time responses due to a rectangular wind step. Although it clearly reflects the wind turbine model behaviour, it does not excite many aeroelastic modes. For that reason, Section 5.4.3 studies the time responses of turbulent wind simulations, showing a better overview of the aeroelastic modes.

5.4.1. Considerations of computational times

The generation of the state-space system matrices for the considered full-order wind turbine model takes around 1.5 s for each operating point. Then, getting the ROM takes another 9 s per operating point. Thus, for example, if the matrices are generated at 21 different wind speeds, building the LTI models requires a total of 3.5 min; the assembly of the full matrices takes approximately 30 s and the model order reduction needs about 3 minutes. This operation could be parallelised for each operational point independently to reduce further the computational cost of assembling the LTI systems.

Then, starting from the ROM at a given operating point, the transfer function calculation takes approximately 85 s. Besides, getting the wind input to the system requires interpolating the positions of the aerodynamic calculation points in time with the wind module DLL. Currently, this is an expensive operation; for instance, for a 600 s simulation, it takes around 120 s to get the wind input. Then, transforming the wind input from the time domain to the frequency domain takes some 0.5 s. Finally, getting the response (output) of the model and converting it back to the time domain takes approximately 17 s. Again, this operation can be parallelised for each wind speed. The computational time of this approach is, therefore, lower than the simulation time required to compute the time series with the nonlinear BHawC code. All the times mentioned above are obtained with a standard laptop machine.

5.4.2. Response to a step in wind speed

A comparison between the response of the linear and the nonlinear BHawC code is performed using a rectangular wind speed step and assuming a uniform wind inflow across the rotor. Ten seconds into the simulation, the wind input signal steps up by 0.1 m/s and after a duration of 1 s, it steps back down to the initial value. The direction of the wind is aligned with the rotor axis. Also, the rotor and the external conditions are assumed to be isotropic, and the system is modelled as an LTI system.

Figs. 5.7 and 5.8 present the time series of the tower-bottom loads from the linear model compared against the BHawC model results. For simplicity, the analysis shows the differences between the linear and nonlinear models at two operational points: 10 m/s (mid-wind speed) and 27 m/s (high wind speed). As seen, the responses are dominated by the fore-aft bending moment m_x, which is coupled to the force in the longitudinal direction (f_y). This is due to the wind speed being aligned with the rotor axis. The steady-state values of the linear model are in good agreement with those from the nonlinear model. Besides, the differences in frequencies and amplitude decays are well captured. However, at the time instant where the wind step is applied, the effect of the torque controller can be seen in the BHawC results. Furthermore, the analysis is extended to show the displacements of the tower-top node for the same cases, as explained in Appendix D.

To quantify the difference between the linear model and the BHawC aeroelastic model, the root-mean-square error (RMSE) normalised with the range (defined as the maximum value minus the minimum value) of the response is checked. For the simulation at 10 m/s mean wind speed, the normalised RMSE is smaller than 3% for all degrees of freedom. Likewise, in the simulation at 27 m/s wind inflow speed, the normalised RMSE is under 3% for the fore-aft and vertical forces and moments. And, for both the lateral force and side-side moment, it is approximately 5%.

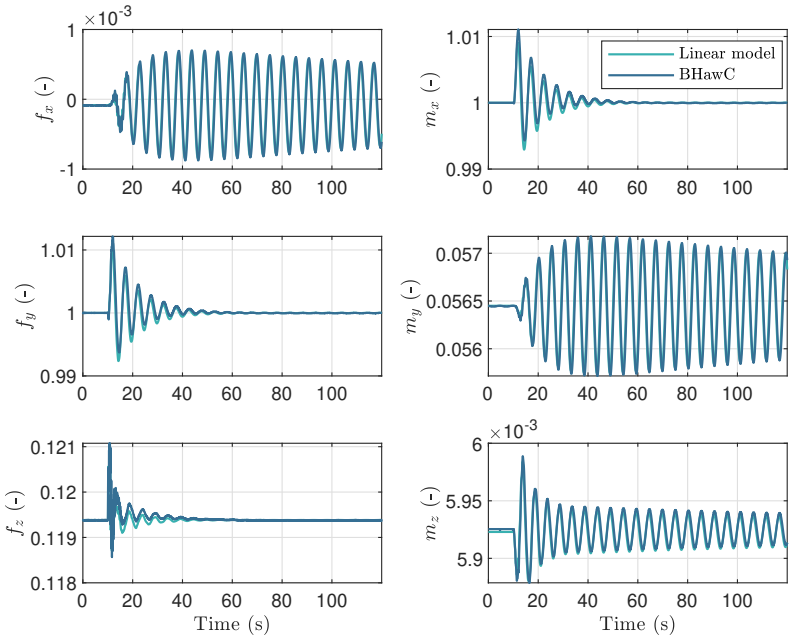

Figure 5.7: Response of the tower-top displacements under a rectangular wind step at 10 m/s hub-height wind speed. Comparison between the linear model and BHawC

Moreover, Fig. 5.9 displays the comparison of the power spectral density (PSD) of the tower-base loads between the nonlinear and the linear model. For simplicity, only one operating point is considered, with a 10 m/s mean hub-height wind speed. Again, the loads with the highest energy are the force in the fore-aft direction f_y and the longitudinal bending moment m_x. The linear model captures the main peaks and the overall energy level as predicted by the nonlinear model. Nevertheless, while frequencies and maximum power levels are well estimated, the linear model presents bigger dips than the nonlinear model. These dips are most important for the force in the lateral direction f_x and the tower-bottom

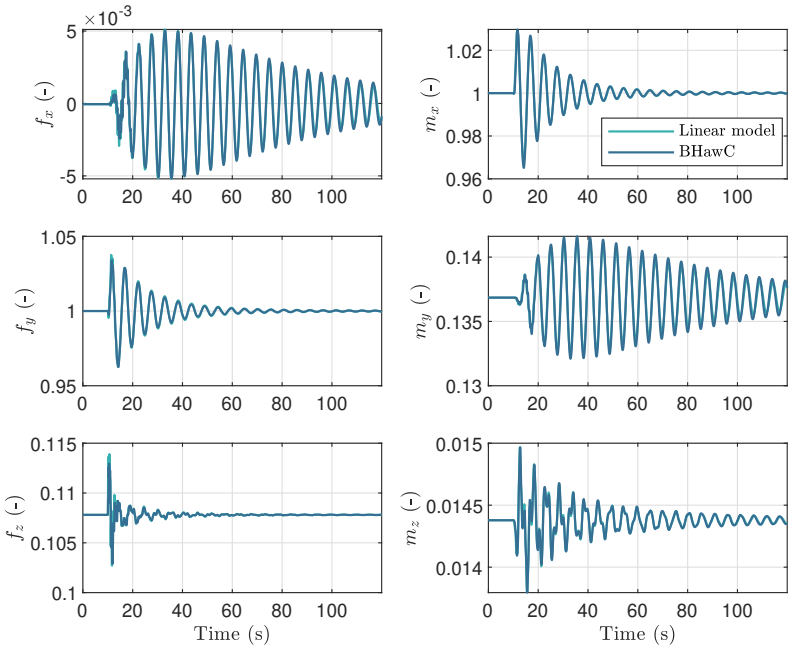

Figure 5.8: Response of the tower-top displacements under a rectangular wind step at 27 m/s hub-height wind speed. Comparison between the linear model and BHawC

side-side moment m_y. The models are in best agreement for lower frequencies and start differing for high frequencies. Some differences among the models might be partly due to having used a 55^{th}-order reduced system to represent the linearised BHawC model, which causes some of the energy in the system to be lost.

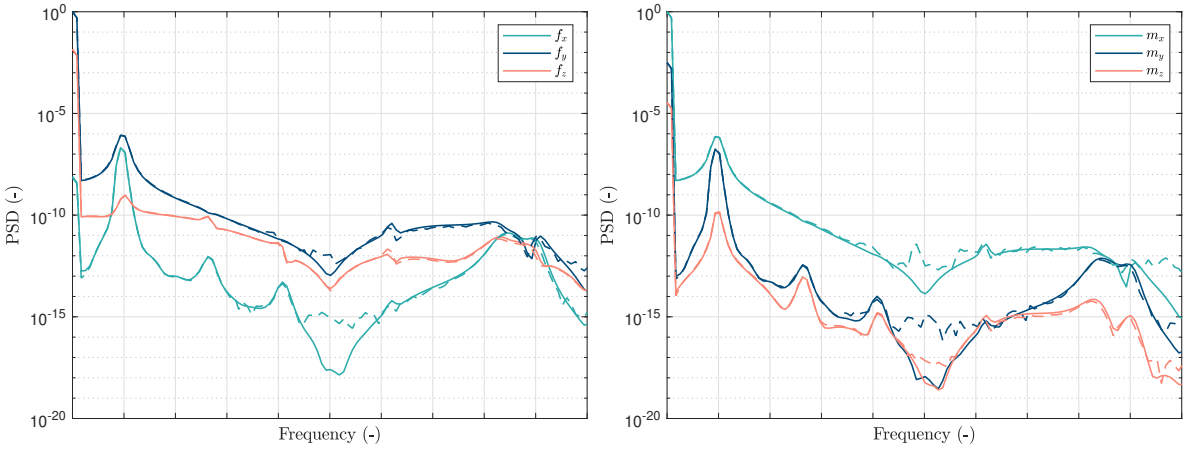

(a) PSD of the tower-bottom forces

(b) PSD of the tower-bottom moments

Figure 5.9: PSD of the tower-base loads under rectangular a wind step at 10 m/s hub-height wind speed. Comparison between the linear model (solid) and BHawC (dashed)

Overall, the differences between the linear model and BHawC for the time series and the PSDs are acceptable for the current application as the steady-state values match and the general trend in the response is captured.

5.4.3. Response to a turbulent wind speed

This study presents a comparison between the responses of the linear and the nonlinear BHawC code in turbulent wind. The simulations are run assuming an isotropic rotor in isotropic environmental conditions, and the wind inflow is a turbulent wind with low turbulence intensity. The analysis is done at three operating points: 8 m/s (below rated), 12 m/s (near rated), and 22 m/s (above rated). Each case is simulated for 600 s (10-minutes) using a turbulent wind speed generated through a Mann turbulence box. Also, a different turbulence intensity is used in each case to evaluate the impact of the increasing turbulence. Accordingly, Tab. 5.1 comprises the values of mean hub-height wind speed and turbulence intensity (TI) used for each study case.

Table 5.1: Environmental conditions: wind speed and turbulence intensity

Wind speed (m/s)	8	12	22
Turbulence intensity (%)	10	5	1

The time series of both the tower-top displacements and the tower-bottom loads are shown. Note that the load channels are normalised with the mean value of the dominant force and moment, respectively. That is, the forces are normalised with the longitudinal force f_y and the moments with the fore-aft moment m_x. Also, recall that the wind turbine has six nodal degrees of freedom consisting of three translations (ξ_x, ξ_y and ξ_z) and three rotations (θ_x, θ_y and θ_z). The fore-aft motion is related to the ξ_y and θ_x displacements; the side-side motion to ξ_x and θ_y; and the vertical motion to ξ_z and θ_z. Below, the three study cases are presented and explained.

Mean wind speed 8 m/s and 10% turbulence intensity

First, the simulations are run using an 8 m/s hub-height mean wind speed and 10% turbulence intensity. Figs. 5.10 and 5.11 show the tower-top displacements and the tower-bottom loads computed using the linear model. The results are compared to the time series from the BHawC simulations under the same environmental conditions.

The motion of the wind turbine system is dominated by the translation in the longitudinal direction ξ_y, which is coupled to the fore-aft rotation θ_x. For the translations in the longitudinal and vertical directions, ξ_y and ξ_z, the dynamic behaviour of the displacements is in fairly good agreement. However, while the trend of the response in time is adequately captured, the fluctuations present higher amplitudes in comparison to the BHawC responses.

Also, the linear model contains some "lag" with respect to the nonlinear response. Particularly, such behaviour can be seen in the rotation about the x_G-axis (θ_x). As mentioned previously, the method of calculating the positions of the aerodynamic calculation points in time uses the assumption of a constant rotor speed. On the other hand, the BHawC simulations use a simple speed controller to maintain the rotor speed constant. In practice, this is not exactly the case, and the rotor speed of the nonlinear model fluctuates in time. In addition, the sampling plane is assumed to remain constant throughout the simulation. The difference in both approaches may cause the positions of the aerodynamic calculation points to vary with respect to the nonlinear model. Consequently, the interpolation of the wind speeds in the turbulence boxes may result in different values for the fluctuating wind speed. Moreover, a large discrepancy in the displacement in the lateral direction ξ_x, which is coupled to the rotation about the θ_y, can be seen.

On the other hand, Fig. 5.11 illustrates the response of the tower-bottom loads subject to an 8 m/s mean wind speed with 10% turbulence intensity. The loads computed with the linear model have a particularly good match for the dominant load channels: the tower-bottom fore-aft moment m_x and the force in the longitudinal direction f_y. For these degrees of freedom, although the amplitudes of the fluctuations are slightly overpredicted, the dynamic responses are in good agreement with the BHawC simulation. This is also the case for the force in the vertical direction. Similarly, the tower-bottom side-side moment m_y presents larger discrepancies, related to the high overestimation of the DOFs of the

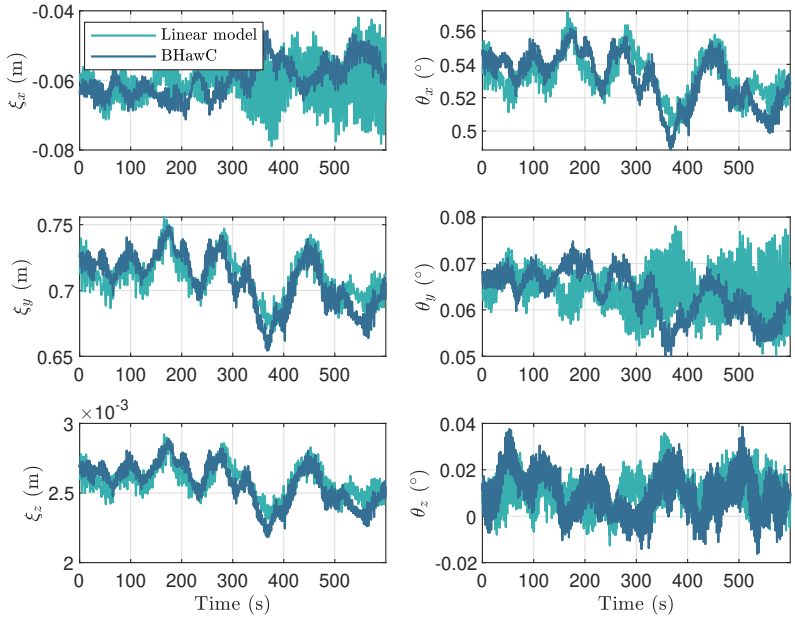

Figure 5.10: Response of the tower-top displacements under an 8 m/s mean wind speed with 10% turbulence intensity. Comparison between the linear model and BHawC

side-side motion. The statistics between the responses are checked through the root-mean-square error (RMSE) normalised with the range of the response. As expected, the error is seen to be highest for the tower-bottom side-side moment and the torsion moment. In brief, the root-mean-square error is around 11% for the degrees of freedom related to the longitudinal and the vertical motions and goes up to approximately 20% for the states linked to the side-side motion of the system.

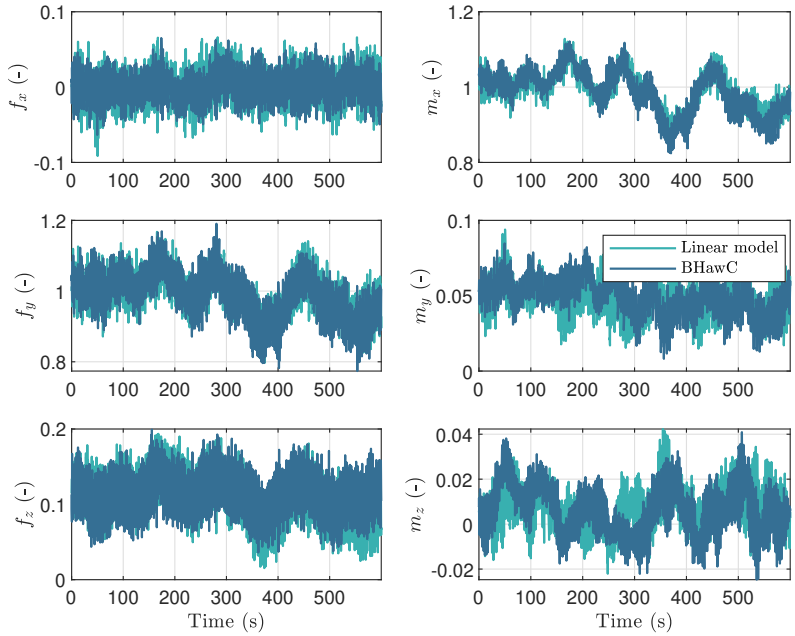

Figure 5.11: Response of the tower-bottom loads under an 8 m/s mean wind speed with 10% turbulence intensity. Comparison between the linear model and BHawC

Mean wind speed 12 m/s and 5% turbulence intensity

Figs. 5.12 and 5.13 compare the tower-top displacements and the tower-bottom loads of the linear model to the time series of the BHawC code. The simulations run for 600 s using a mean hub-height

wind speed of 12 m/s and a 5% turbulence intensity. Hence, the wind turbine is operating in near-rated conditions. Again, the dominant displacements are the tower translation in the fore-aft direction ξ_y and the rotation about the x_G-axis (θ_x). Similarly, the tower fore-aft and vertical translations and the fore-aft rotation are in fairly good agreement with the nonlinear model. Nevertheless, the amplitudes of the fluctuations are seen to be a bit higher. The responses of these degrees of freedom also contain a time shift, which is likely to be related to the method in which the positions of the aerodynamic calculation points are calculated over time. Finally, the time series of the translation and the rotation in the side-side direction, ξ_x and θ_y, present a high difference with respect to the BHawC simulation. Besides, as the wind speed is near rated conditions, all degrees of freedom experience larger displacements than for the case above, where the operating point is in the below-rated region. Another reason for the discrepancies might be linked to the deviation from the operating point since the wind turbine is operating in the near-rated region.

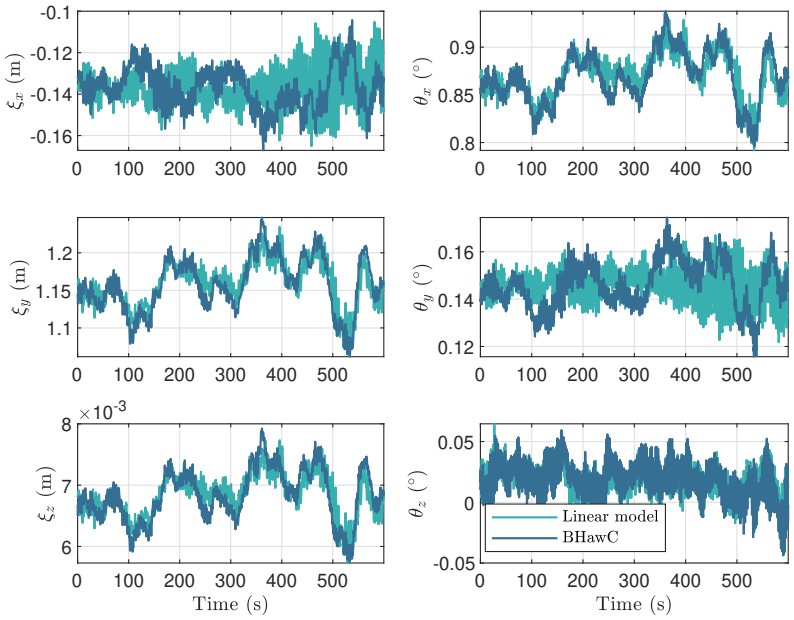

Figure 5.12: Response of the tower-top displacements under a 12 m/s mean wind speed with 5% turbulence intensity. Comparison between the linear model and BHawC

In this line, Fig. 5.13 illustrates the tower-base loads for a simulation with a 12 m/s mean hub-height wind speed and 5% turbulence intensity. In general, the dynamic response of the linear model is congruent with the nonlinear BHawC model. Among all the load channels, those providing the best match are the force in the longitudinal direction f_y and the tower-base fore-aft moment m_x. Besides, the force in the lateral direction f_x and the side-side moment m_y are overestimated as a result of the corresponding displacements being overpredicted. The normalised RMSE is used to measure the differences between the values from the linearised model and BHawC. All load channels present around a 12% error with respect to the BHawC simulations except for the side-side moment, where it is approximately 20%. This large difference is intrinsically related to the lateral displacement and the side-side rotation, which are seen to be larger than those in the BHawC results.

Last, the power spectral density of the loads at the tower base is compared in Fig. 5.14 between the linear model and BHawC. Both the PSD of the forces and the moments are studied. On the whole, the PSD of the linear model is overestimated for low frequencies. Despite this variation, the energy content of the solution is reproduced fairly well for the remaining frequencies. As seen, the energy level of the highest energy peak is overestimated for the load channels related to the lateral displacement: lateral force and side-side moment, f_x and m_y, respectively.

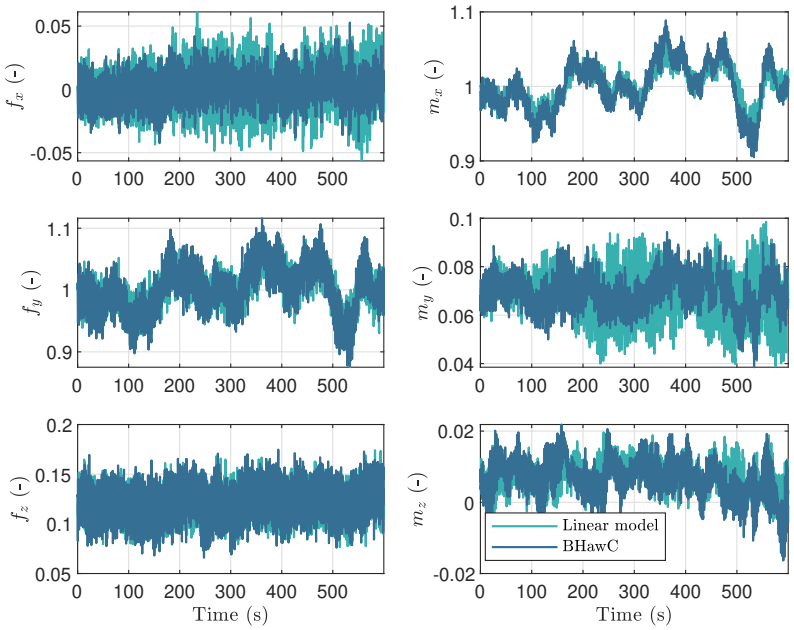

Figure 5.13: Response of the tower-bottom loads under a 12 m/s mean wind speed with 5% turbulence intensity. Comparison between the linear model and BHawC

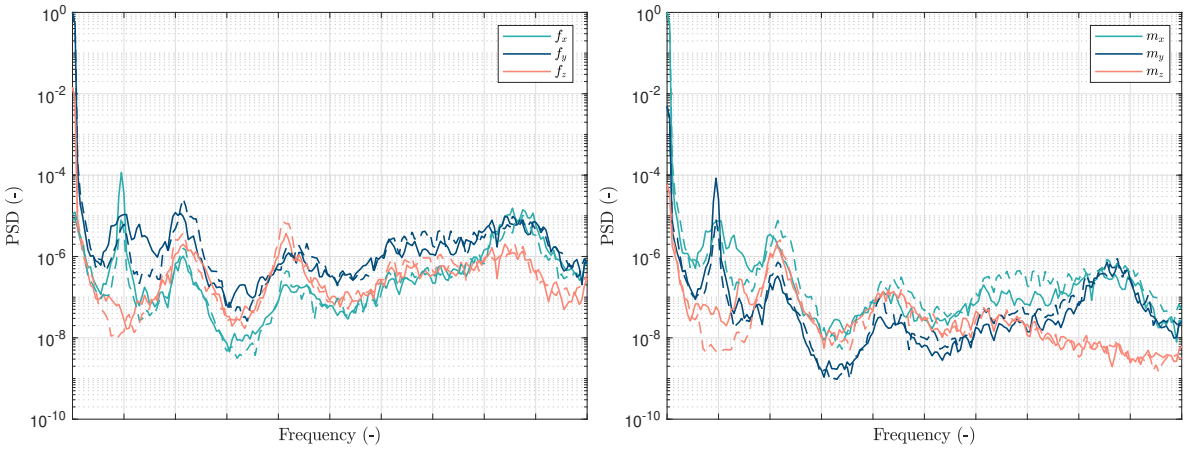

(a) PSD of the tower-bottom forces

(b) PSD of the tower-bottom moments

Figure 5.14: PSD of the tower-bottom loads under a 12 m/s wind speed and 5% turbulence intensity. Comparison between the linear model (solid) and BHawC (dashed)

Mean wind speed 22 m/s and 1% turbulence intensity

Last, a simulation using a 22 m/s hub-height wind speed and assuming a 1% turbulence wind speed is considered. Once more, the time series of the output are obtained from 10-min simulations. Figs. 5.15 and 5.16 show the tower-top states and the tower-bottom loads over time. Again, the dominant displacements are the translation in the fore-aft direction ξ_y and the fore-aft rotation θ_x. And, as expected, the smallest displacements are the vertical translation ξ_z and torsion θ_z. As seen, in this case, the discrepancies between the linear model and BHawC are more obvious. Regarding the displacements of the tower-top node, the linear model follows the trend of the BHawC simulations during the initial some 150–200 s, particularly for the displacements in the longitudinal and vertical directions. Soon after, the output from the linear model begins to differ from the nonlinear response, and the solution seems to contain an error accumulating in time. Again, the degrees of freedom related to the side-side motion are overestimated and present the highest differences.

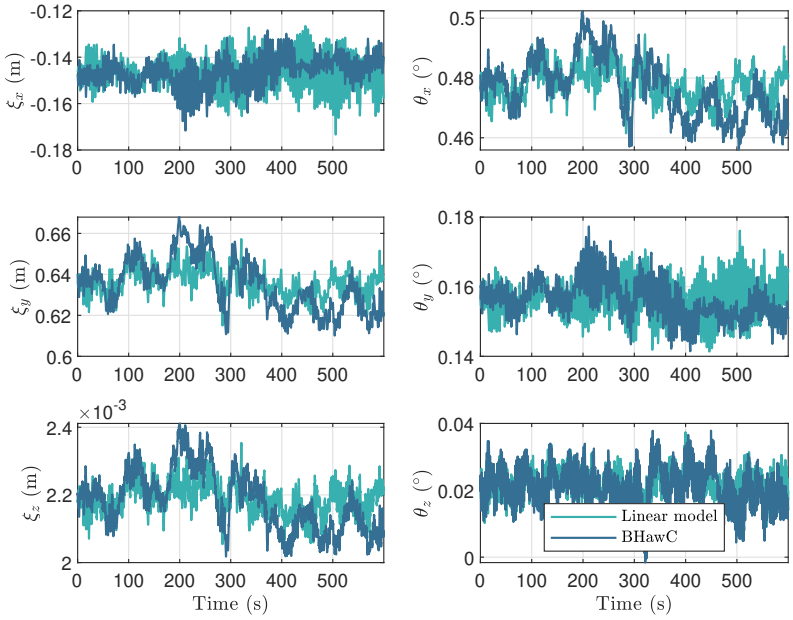

Figure 5.15: Response of the tower-top displacements under a 22 m/s mean wind speed with 1% turbulence intensity. Comparison between the linear model and BHawC

In terms of the load channels, similar behaviour can be noticed. Also, the normalised root-mean-square error is around 14% for all tower-bottom loads except for the loads related to the side-side motion, the lateral force f_x and the side-side moment m_y, where the error increases up to values of 22%. The reason for this is likely to be linked to the influence of the simple controller used in the BHawC simulations. As seen in Fig. 5.18, at higher wind speeds, the jumps in the rotor speed become more important. As mentioned above, the methodology in the linear model assumes a constant rotor speed to compute the positions of the aerodynamic calculations points in time. A greater shift in rotor speed will cause the interpolated wind speed to differ.

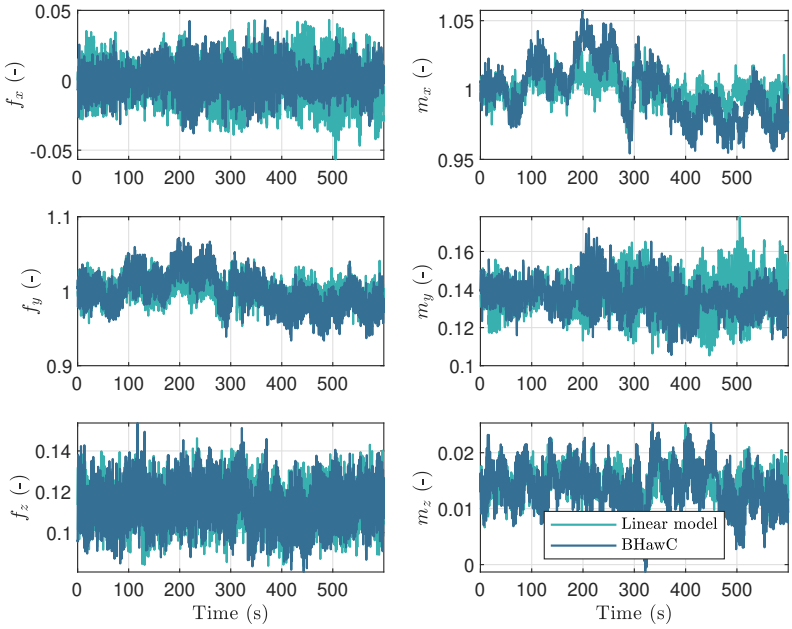

Figure 5.16: Response of the tower-bottom loads under a 22 m/s mean wind speed with 1% turbulence intensity. Comparison between the linear model and BHawC

Finally, the power spectral density of the tower-base loads of the linear model is compared against that

of the nonlinear BHawC model in Fig. 5.17 for the simulation at 22 m/s and 1% TI. As seen, the energy level is captured fairly well in the frequency range of interest, especially for the longitudinal and vertical forces and moments. However, the linear model overpredicts the highest energy peak of the force in the lateral direction (f_x) and the side-side moment (m_x). For the higher frequencies, the models are more in disagreement, particularly for m_x and m_y.

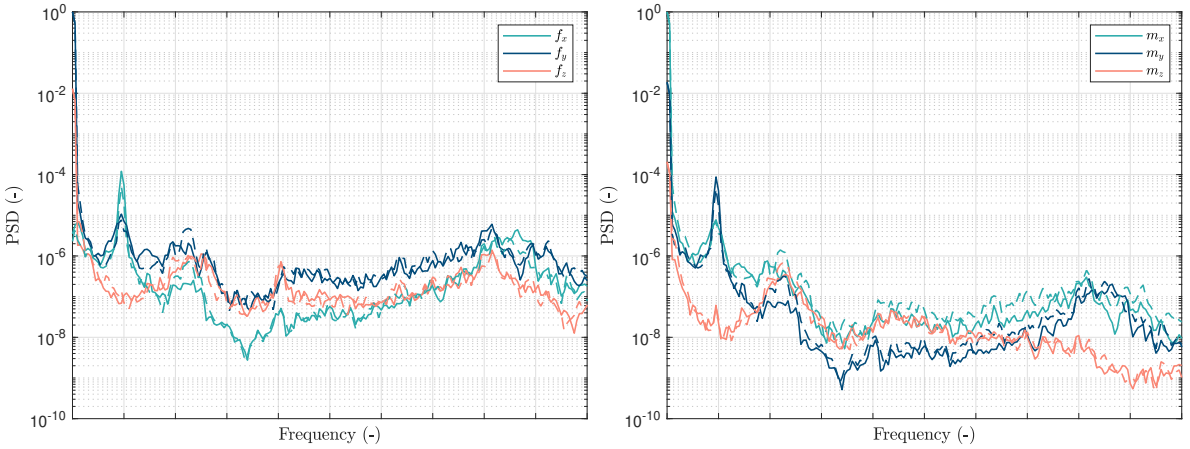

(a) PSD of the tower-bottom forces

(b) PSD of the tower-bottom moments

Figure 5.17: PSD of the tower-base loads under a 22 m/s wind speed and 1% turbulence intensity. Comparison between the linear model (solid) and BHawC (dashed)

In summary, the simulations presented above display the discrepancies between the linear and nonlinear models for turbulent inflows with mild turbulence intensity. Three operational points and three different turbulence intensities are considered. As mentioned, a factor that is expected to influence the discrepancies between both models is the assumption used when computing the velocities at the aerodynamic calculation points. For instance, Fig. 5.18 compares the rotor speed of the BHawC simulation with that assumed in the linear model. While the linear model assumes a constant rotor speed to get the positions of the aerodynamic sections in time, the BHawC simulations use a simple controller to regulate the rotor speed. At low wind speeds, this controller maintains the rotational speed fairly constant throughout the simulation. At higher wind speeds, however, the fluctuations become quite relevant. The sampling plane is also assumed constant to get the input wind speeds. In addition, other potential reasons for the discrepancies between both models are the deviation from the operating point, defined by mean wind speed, rotor speed and pitch angle, the frequency properties of the solutions, and the system presenting a nonlinear behaviour.

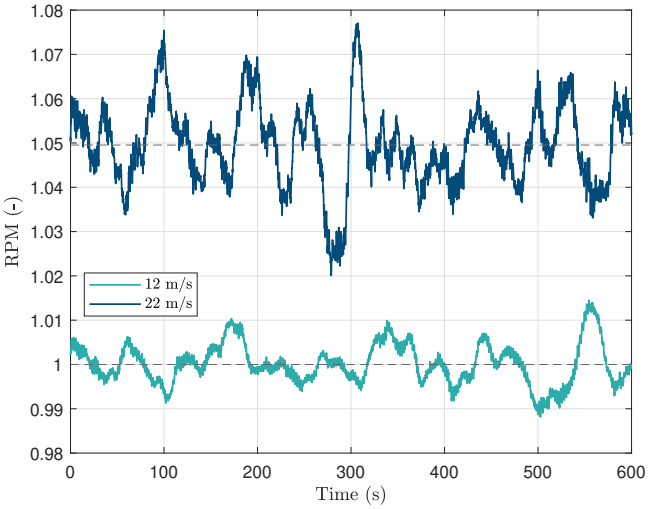

Figure 5.18: Rotor speed of the BHawC simulations at two wind speeds with 5% turbulence intensity

5.4.4. Damage equivalent loads

Fatigue loads are an important issue for wind turbines, as they are exposed to long-term vibrations and fluctuating loads. This section outlines the fatigue damage analysis of the linear model and provides its comparison to the nonlinear BHawC code. The fatigue damage equivalent loads (DELs) are computed from the load time series by applying a rainflow counting (RFC) algorithm. Particularly, the DELs regarding the tower-bottom fore-aft moment m_x, tower-bottom side-side moment m_y, and tower-top torsion m_z are studied. Tab. 5.2 depicts the Wöhler exponent used for each load channel. The resulting fatigue loads are also checked employing the Wöhler exponents used in SGRE, where 3.5 is selected for all load channels.

Table 5.2: Example of Wöhler exponent (Torben Juul Larsen, personal communication to R. Riva)

Load channel	Wöhler exponent
Tower fore-aft	4
Tower side-side	4
Tower torsion	7

Moreover, the analysis is done considering the mean wind speeds in the previous study and three turbulence intensities for each. Tab. 5.3 depicts the percentage difference in the estimated DELs between the linearised BHawC model and the nonlinear model. 'TB FA' and 'TB SS' refer to the tower-bottom fore-aft and side-side moments, and 'TT Tors.' denotes the tower-top torsional moment. As seen, the DELs estimated using the linear model present large differences from those in BHawC, and the accuracy varies depending on the wind speed at the operating point. Overall, the fatigue loads are overpredicted in all study cases, while the tower-top torsion is the load showing the best agreement with BHawC.

Table 5.3: Percentage difference between the DELs estimated from the linear model and BHawC

Wind speed (m/s)	TI (%)	Difference in DELs (%)		
		TB FA	TB SS	TT Tors.
8	1	6.23	3.33	2.85
	5	5.76	4.01	2.45
	10	6.85	2.25	1.89
12	1	19.66	47.78	10.07
	5	19.28	48.88	11.07
	10	19.16	49.60	10.69
22	1	22.27	18.68	21.25
	5	23.33	29.19	21.82
	10	24.19	35.08	22.71

For the simulations at 8 m/s mean hub-height wind speed (below-rated speed), the estimated fatigue loads are within reasonable agreement with those from the BHawC simulations. Besides, at 12 m/s (around rated conditions), the difference in the DELs becomes very large. Particularly, the tower-bottom side-side moment differs by around 50%. Finally, at high winds, for instance, in the case with 22 m/s hub-height wind speed, the estimated DELs are overpredicted by approximately 20%, meaning they present a large discrepancy with the fatigue loads as predicted in the BHawC simulations.

6

Isotropic system with high turbulence intensity

For isotropic rotors in isotropic environmental conditions, the Coleman transformation is often used to represent wind turbines as time-invariant systems. However, suppose the inflow wind field has a high turbulence intensity. In that case, the velocity fluctuations can cause the wind turbine to suddenly jump from one operating region to another. In doing so, given that the controller continuously monitors the system, the control laws will also vary in time. To handle such nonlinearities and hence, follow the wind turbine performance variation in time, the system can be modelled as a linear parameter-varying (LPV) system. This chapter presents the specific LPV system derived from the BHawC aeroelastic code (see Section 6.1) and shows the time-domain analysis used to get the loads acting on isotropic wind turbines in high turbulence intensity wind inflow (see Section 6.2). Some numerical results of the applied method are included in Section 6.3.

6.1. Linear Parameter-Varying (LPV) system

As mentioned, to capture the changes in the wind turbine dynamics and thus, adapt to the controller variability, the nonlinear WT system is modelled as a linear parameter-varying (LPV) system. Accordingly, the nonlinear BHawC model is approximated by an LPV state-space form of the system using a linearisation-based (or grid-based) approach. Hence, the nonlinear system is linearised around a set of operating/equilibrium points, resulting in a series of local LTI representations of the system along a grid of scheduling parameters $\mathbf{p}$. Fig. 6.1 illustrates the obtained LPV system, where each local description corresponds to the linearised BHawC model at an equilibrium and describes the system dynamics in the local vicinity of that point. Furthermore, these LTI models can be interpolated to represent the physical system over the entire operation regime.

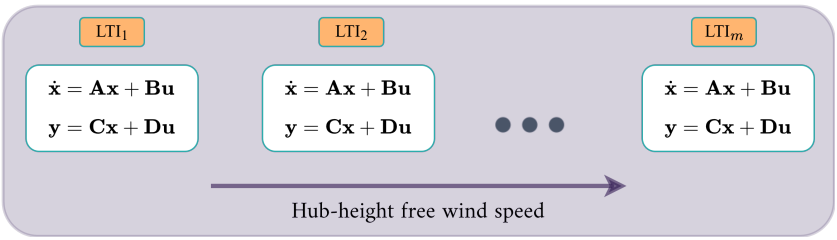

Figure 6.1: Wind turbine LPV model defined on a linear scheduling grid

For this study, the parameter of the original system selected to obtain an equivalent LPV description is

an external variable. Specifically, it is assumed that the hub-height wind speed in the rotor axial direction, U_w, is the scheduling variable that governs the dynamic behaviour of the system.

6.1.1. Linearisation-based approximation

The linearisation theory is applied to the state-space representation of the nonlinear model to obtain the local LTI models in a state-space form. To achieve this, the T-periodic tangent mass $\mathbf{M}$, damping/gyroscopic $\mathbf{C}$, and stiffness $\mathbf{K}$ matrices are first exported from BHawC at each grid point of the scheduling space. Then, the matrices are transformed using the Coleman transformation as described in Section 5.1, leading to the assembly of the local linear time-invariant (LTI) state-space models.

The grid-based representation of the LPV system can be extended to allow offsets in the state variables and the inputs. These correspond to the equilibrium configuration and the inputs to the system at those operating points around which the model is linearised. Therefore, the LPV model can be expressed in the *affine* form as:

$$\begin{aligned} \dot{\hat{\mathbf{x}}}(t;\mathbf{p}) &= \mathbf{A}(\mathbf{p})\,\hat{\mathbf{x}}(t;\mathbf{p}) + \mathbf{B}(\mathbf{p})\,\hat{\mathbf{u}}(t;\mathbf{p}) \\ \hat{\mathbf{y}}_{gf}(t;\mathbf{p}) &= \mathbf{C}(\mathbf{p})\,\hat{\mathbf{x}}(t;\mathbf{p}) + \mathbf{D}(\mathbf{p})\,\hat{\mathbf{u}}(t;\mathbf{p}) \end{aligned} \tag{6.1}$$

where the states of the linear model in the affine formulation are related to the states of the overall LPV model as $\hat{\mathbf{x}}(t;\mathbf{p}) = \mathbf{x}(t) - \tilde{\mathbf{x}}(\mathbf{p})$, and similarly for the inputs $\hat{\mathbf{u}}(t;\mathbf{p}) = \mathbf{u}(t) - \tilde{\mathbf{u}}(\mathbf{p})$.

6.1.2. Model order reduction

Motivated by reducing the computational expense of the simulations, the use of model order reduction (MOR) methods is explored and integrated into the methodology. Specifically, and as mentioned previously in Chapter 5, the model order reduction technique used for this work is the balanced truncation (BT) approach, which consists of first balancing the original model and then truncating it so as to remove the negligible states of the system.

Balanced truncation

Balancing the linearised dynamic system allows to identify which states are relevant to describe the model and which state variables can be removed without compromising the system's behaviour. Recall that balanced state-space models are characterised by having equal controllability and observability Gramians, these being positive diagonal matrices with the Hankel singular values (HSVs) as entries.

As described above in Section 4.3, the method of truncating the resulting balanced realisation is based on eliminating the states with singular numbers below a certain threshold. In practice, the system can be reduced by partitioning it into two blocks: one for the state variables that contain the relevant characteristics of the full system and one for the states with small HSVs. On that account, the latter can be neglected to form the reduced-order model (ROM). Given that the projection subspaces are biorthogonal ($\mathbf{W}^\top\mathbf{V} = \mathbf{I}$), the equations that describe the ROM result in:

$$\begin{aligned} \dot{\mathbf{x}}_r &= \mathbf{A}_r\mathbf{x}_r + \mathbf{B}_r\mathbf{u} \\ \mathbf{y}_r &= \mathbf{C}_r\mathbf{x}_r + \mathbf{D}_r\mathbf{u} \end{aligned} \tag{6.2}$$

where

$$\mathbf{A}_r = \mathbf{W}^\top\mathbf{A}\mathbf{V}, \quad \mathbf{B}_r = \mathbf{W}^\top\mathbf{B}, \quad \mathbf{C}_r = \mathbf{C}^\top\mathbf{V}, \quad \mathbf{D}_r = \mathbf{D}\,, \tag{6.3}$$

and the state variables are approximated as $\mathbf{x} \approx \mathbf{V}\mathbf{x}_r$ and $\mathbf{x}_r \approx \mathbf{W}^\top\mathbf{x}$.

In summary, after determining which modes can be eliminated, and thus choosing the order r of the ROM, the model order reduction method is applied to the full system such that the projection matrices can be calculated and stored. With such transformations, the state variables lose their physical meaning. Therefore, the transformation matrices are stored for each grid point in the LPV system, which will later allow for the necessary interpolation of the local LTI models.

As explained in further detail in Section 4.3, this work uses the `sssMOR` toolbox [21] in MATLAB® to per-

form the model order reduction of the FOM. By doing so, the sparse representation of the system is exploited to reduce the storage requirements of the MOR method, and the projection matrices $\mathbf{V}$ and $\mathbf{W}$ are extracted to later interpolate the LTI systems in the same basis. It also allows decomposing the model into its stable and unstable parts, which is used to ensure that no unstable poles are present in the system.

6.1.3. Discretisation of the LPV system

In order to obtain a computationally simpler system, the LPV model is represented in the discrete-time (DT) domain. For simplicity, the discretisation of the continuous-time system is done assuming a zero-order hold (ZOH). Therefore, in the derived discrete-time description of the system, the signals are only observed at the end of the sampling interval, and the variation of the input $\mathbf{u}$ and the scheduling parameter $\mathbf{p}$ signals is piecewise-constant as [35]:

$$\mathbf{u}(t) = \mathbf{u}_\mathrm{d}(k)\,, \quad \mathbf{p}(t) = \mathbf{p}_\mathrm{d}(k)\,, \quad \forall t \in [kT_\mathrm{d}, (k+1)T_\mathrm{d}) \quad \text{and} \quad \mathbf{y}_{gf,\mathrm{d}}(k) = \mathbf{y}_{gf}(kT_\mathrm{d})\,. \tag{6.4}$$

where T_d is the sampling (discretisation) period, selected according to the criteria in Tóth [35] used for the appropriate choice of the discretisation step size.

In this research, the discretisation method used is the *complete* signal evolution approach in Tóth [35], previously explained in Section 2.2.4. The reason for choosing this discretisation method is based on wanting to reduce the discretisation error of the methodology; while approximate methods are less complex, they introduce discretisation errors. For example, in the Euler discretisation approach, the output has a strong dependence on the discretisation time step as the matrix exponential term is approximated to its first-order expansion. Among the existing approaches, the exact discretisation is the one that provides the best match between the discrete-time output and the continuous-time output at the sampling times. Therefore, by transferring the model into its discrete counterpart, the state-space matrices of the ROM become:

$$\begin{aligned}
\mathbf{A}_\mathrm{d}(\mathbf{p}_\mathrm{d}(k)) &= e^{\mathbf{A}_r(\mathbf{p}(kT_\mathrm{d}))T_\mathrm{d}} \\
\mathbf{B}_\mathrm{d}(\mathbf{p}_\mathrm{d}(k)) &= \mathbf{A}_r^{-1}(\mathbf{p}(kT_\mathrm{d}))\left(e^{\mathbf{A}_r(\mathbf{p}(kT_\mathrm{d}))T_\mathrm{d}} - \mathbf{I}\right)\mathbf{B}_r(\mathbf{p}(kT_\mathrm{d})) \\
\mathbf{C}_\mathrm{d}(\mathbf{p}_\mathrm{d}(k)) &= \mathbf{C}_r(\mathbf{p}(kT_\mathrm{d})) \\
\mathbf{D}_\mathrm{d}(\mathbf{p}_\mathrm{d}(k)) &= \mathbf{D}_r(\mathbf{p}(kT_\mathrm{d}))\,.
\end{aligned} \tag{6.5}$$

Algorithm 2 contains the procedure followed to assemble the discrete-time LPV system, starting from the full LTI systems at each grid point of the scheduling domain. It depicts how, for each operating point in the LPV grid, the linearised model is extracted from BHawC, reduced, discretised, and stored. Besides, the scheduling parameter value, the equilibrium configuration, and the wind speed inputs are also saved at each grid point in the LPV domain.

6.2. Time-domain analysis

To address the dynamic variations of the system, the model is studied in the time domain. In the discretised domain, the derivative of the state is expressed as the state update vector: $\dot{\mathbf{x}} = \mathbf{x}(k+1)$. Hence, the discretised LPV state-space model can be formulated in the affine form as:

$$\begin{aligned}
\mathbf{x}(k+1) &= \mathbf{A}_\mathrm{d}(\mathbf{p}_\mathrm{d})\,(\mathbf{x}(k) - \tilde{\mathbf{x}}(\mathbf{p}_\mathrm{d})) + \mathbf{B}_\mathrm{d}(\mathbf{p}_\mathrm{d})\,(\mathbf{u}(k) - \tilde{\mathbf{u}}(\mathbf{p}_\mathrm{d})) + \tilde{\mathbf{x}}(\mathbf{p}_\mathrm{d}) \\
\mathbf{y}_{gf}(k) &= \mathbf{C}_\mathrm{d}(\mathbf{p}_\mathrm{d})\,(\mathbf{x}(k) - \tilde{\mathbf{x}}(\mathbf{p}_\mathrm{d})) + \mathbf{D}_\mathrm{d}(\mathbf{p}_\mathrm{d})\,(\mathbf{u}(k) - \tilde{\mathbf{u}}(\mathbf{p}_\mathrm{d})) + \tilde{\mathbf{y}}_{gf}(\mathbf{p}_\mathrm{d})\,.
\end{aligned} \tag{6.9}$$

where $\mathbf{A}_\mathrm{d}$, $\mathbf{B}_\mathrm{d}$, $\mathbf{C}_\mathrm{d}$ and $\mathbf{D}_\mathrm{d}$ are the discretised state-space matrices, $\mathbf{p}_\mathrm{d}$ is the discrete-time scheduling parameter, and $\tilde{\mathbf{u}}$ and $\tilde{\mathbf{x}}$ are the values of the inputs and the equilibrium state variables at the operating points around which the model is linearised.

Algorithm 2: Assembly of the discretised LPV system

Input: T-periodic tangent mass $\mathbf{M}$, stiffness $\mathbf{K}$ and damping $\mathbf{C}$ matrices exported from BHawC at each operating point

Output: DT parameter-varying system $\mathbf{H}$ and projection transformations such that $\mathbf{x}_r \approx \mathbf{V}\mathbf{x}$ and $\mathbf{W}^\top\mathbf{V} = \mathbf{I}$

1 **foreach** *Operating point* $i = 1 : m$ **do**

2 Compute the system matrices and assemble the local LTI model:

$$\mathbf{H}_{\ell,i} = \left[\begin{array}{c|c} \mathbf{A}_i & \mathbf{B}_i \\ \hline \mathbf{C}_i & \mathbf{D}_i \end{array}\right] \tag{6.6}$$

3 Reduce the order of the system and get the BT projection matrices $\mathbf{V}_i$ and $\mathbf{W}_i$:

$$\mathbf{H}_{r,i} = \left[\begin{array}{c|c} \mathbf{A}_{r,i} & \mathbf{B}_{r,i} \\ \hline \mathbf{C}_{r,i} & \mathbf{D}_{r,i} \end{array}\right] = \left[\begin{array}{c|c} \mathbf{W}_i^\top\mathbf{A}_i\mathbf{V}_i & \mathbf{W}_i^\top\mathbf{B}_i \\ \hline \mathbf{C}_i\mathbf{V}_i & \mathbf{D}_i \end{array}\right] \tag{6.7}$$

4 Convert the system to the discrete-time domain:

$$\mathbf{H}_{\mathrm{d},i} = \left[\begin{array}{c|c} \mathbf{A}_{\mathrm{d},i} & \mathbf{B}_{\mathrm{d},i} \\ \hline \mathbf{C}_{\mathrm{d},i} & \mathbf{D}_{\mathrm{d},i} \end{array}\right] \tag{6.8}$$

5 Get the local value of the scheduling parameter p_i, i.e., free hub-height wind speed in the rotor axial direction $U_{w,i}$.

6 Store the offsets in the states variables and inputs, $\tilde{\mathbf{x}}_i$ and $\tilde{\mathbf{u}}_i$, respectively.

7 Store the matrices in the LPV scheduling domain: $\mathbf{H}_i = \mathbf{H}_{\mathrm{d},i}$

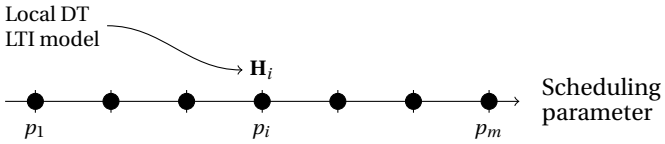

The procedure explained in Section 3.1.1 is employed to get the steady-state configuration of the analytical wind turbine model, used to test the implemented methodology. On that account, the model is first simplified under the assumption of isotropic conditions. Next, the MBC transformation is used to transform each system in the LPV domain into its time-invariant representation. Thus, the systems reduce to nonlinear systems that can be solved for the state variables. Besides, as the simple model only considers the wind input at the wind turbine hub, the offset to the inputs corresponds to the hub-height wind speed in the axial direction. In contrast, the linearised BHawC model uses the wind speed at the aerodynamic calculation points along the wind turbine blades as the input to the system. For this reason, the offset to the input signals $\tilde{\mathbf{u}}$ is the mean free wind speed (in the three components) at all aerodynamic sections.

Finally, Algorithm 3 presents the methodology to obtain the response of the LPV model. The algorithm loops over the simulation time and interpolates the current hub-height wind speed over the array of scheduling parameters. For the wind speeds that are not simulated, the system matrices are interpolated using either nearest neighbour interpolation (NN) or linear interpolation (LI) of the neighbouring LTI systems. Assuming that m local LPV state-space models have been obtained, they must be defined coherently (in the same basis) to allow for such interpolation. In brief, the methodology uses the discrete-time domain where, for each time instant, the current wind speed is interpolated over the scheduling parameters, the output is evaluated, and the state vector is updated. These steps are repeated over time until the end of the simulation time.

Algorithm 3: DT simulation of the LPV system

Input: DT parameter-varying system $\mathbf{H}$, scheduling parameter array $\mathbf{p}$, projection transformation matrices $\mathbf{V}\,\mathbf{W}$, and wind input $\mathbf{u}_{\mathrm{B}}(t)$

Output: Response of the system $\mathbf{y}$

Initialize the states $\mathbf{x}(t_0) = \mathbf{x}_0$ and the output $\mathbf{y}(t_0) = \mathbf{y}_0$ of the system

foreach *time step* $k = 1 : N_t$ **do**

Interpolate the current hub-height wind speed in the y_G-direction ($U_{w,k}$) over the scheduling parameter array $\mathbf{p}$

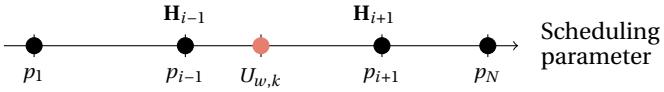

if *Nearest neighbour interpolation* **then**

Choose the neighbouring LTI model with the scheduling parameter closest to the current wind speed:

$$p_i = \mathbf{p}(\min|\mathbf{p} - U_{w,k}|), \quad \mathbf{H}_k = \mathbf{H}_i \tag{6.10}$$

Transform the local ROM model into a coherent LTI model:

$$\mathbf{H}_k = \left[\begin{array}{c|c} \mathbf{A}_k & \mathbf{B}_k \\ \hline \mathbf{C}_k & \mathbf{D}_k \end{array}\right] = \left[\begin{array}{c|c} \mathbf{W}_i^{-\top}\mathbf{A}_{r,i}\mathbf{V}_i^{-1} & \mathbf{W}_i^{-\top}\mathbf{B}_{r,i} \\ \hline \mathbf{C}_{r,i}\mathbf{V}_i^{-1} & \mathbf{D}_{r,i} \end{array}\right] \tag{6.11}$$

else if *Linear Interpolation* **then**

Compute the interpolation weights w: the dimensionless distance between the current wind speed $U_{w,k}$ and the neighbouring scheduling parameters p_{i-1} and p_{i+1}:

$$w_{i-1} = \frac{p_{i+1} - U_{w,k}}{p_{i+1} - p_{i-1}}, \quad w_{i+1} = \frac{U_{w,k} - p_{i-1}}{p_{i+1} - p_{i-1}} \tag{6.12}$$

such that $w_{i-1} + w_{i+1} = 1$.

Get the interpolated LTV system as a weighted average of the neighbouring LPV systems, and transform it into a coherent model:

$$\mathbf{H}_k = \left[\begin{array}{c|c} \mathbf{A}_k & \mathbf{B}_k \\ \hline \mathbf{C}_k & \mathbf{D}_k \end{array}\right] = \left[\begin{array}{c|c} \sum_{j\in S_j} w_j\mathbf{W}_j^{-\top}\mathbf{A}_{r,j}\mathbf{V}_j^{-1} & \sum_{j\in S_j} w_j\mathbf{W}_j^{-\top}\mathbf{B}_{r,j} \\ \hline \sum_{j\in S_j} w_j\mathbf{C}_{r,j}\mathbf{V}_j^{-1} & \sum_{j\in S_j} w_j\mathbf{D}_{r,j} \end{array}\right] \tag{6.13}$$

with $S_j = \{i-1,\ i+1\}$.

Solve the DT state-space equations (update the states and evaluate the output):

$$\begin{aligned} \mathbf{x}_{k+1} &= \mathbf{A}_k\hat{\mathbf{x}}_k + \mathbf{B}_k\hat{\mathbf{u}}_{\mathrm{B},k} + \tilde{\mathbf{x}}_k \\ \mathbf{y}_{gf,k} &= \mathbf{C}_k\hat{\mathbf{x}}_k + \mathbf{D}_k\hat{\mathbf{u}}_{\mathrm{B},k} + \tilde{\mathbf{y}}_k \end{aligned} \tag{6.14}$$

6.3. Numerical results: analytical wind turbine model

This section contains a comparison of the linear analytical wind turbine model against its nonlinear behaviour. This study assumes an isotropic wind turbine in isotropic external conditions. Therefore, all blades have the same structural properties, and gravity field, wind shear, wind misalignment, and tower shadow are not present in the analysis. First, Section 6.3.1 gives an overview of the computation time required to assemble and evaluate the LPV system. Then, Section 6.3.2 presents the dynamic response of the analytical wind turbine under a wind ramp increasing linearly in time. Last, Section 6.3.3 shows the time responses of the model both under a turbulent wind speed and a turbulent wind ramp. The displacements of all eight degrees of freedom are discussed in both cases.

6.3.1. Consideration of computational times

Considering a 600 s simulation with turbulence, the nonlinear model takes around 60 s to get the dynamic response of the system. Regarding the linear parameter-varying system, the scheduling parameter used is the hub-height free wind speed. A fine grid is used for its assembly, where the system is stored every 0.2 m/s. It takes approximately 0.15 s to loop over the scheduling parameter grid and store both the LPV system and the offsets in the inputs and the state variables of the system. Then, the discrete-time LPV system is obtained assuming a zero-order hold and using a time step $T_\mathrm{d} = 0.1$ s. Discretising the state-space matrices of the entire LPV system takes ≈ 0.02 s.

The simulation of the continuous-time LPV systems takes some 12 s, meaning the latter is about 5× faster than the nonlinear model. Finally, the simulation using the discrete-time LPV model is around 100 times faster, as it needs about 0.5 s to get the response of the system. Overall, including obtaining the LPV system, discretising, and evaluating the output, the discrete-time LPV system requires $\approx$ 85× less computational time than the nonlinear model simulation. The aforementioned times are obtained with a standard laptop machine.

6.3.2. Linear wind ramp

The dynamic behaviour of the analytical wind turbine model is compared against its nonlinear response. The simulations run for 120 s with a linearly ramping axial wind at the wind turbine hub-height. Three cases are studied, for which the turbine operates (a) between cut-in and rated conditions, (b) around rated conditions, and (c) above-rated in high wind speeds. The wind speed is assumed to increase uniformly from the initial value until its maximum value over the time interval from 20 s to 100 s. Outside this interval, the values are kept constant at the initial and final values, respectively.

The turbine is represented in the ground-fixed coordinate system. Thence, the analysis uses the collective, cosine and sine coordinates to describe the rotations of the flapwise and edgewise blade motions. The LPV system is extracted from the cut-in speed (3 m/s) until the cut-out speed (25 m/s) with steps of 0.2 m/s. The discretisation time step used is $T_\mathrm{d} = 0.1$ s, and the LPV model is represented in the affine LPV form to account for the offsets in the input and the state variables.

Ramping wind speed from 3 m/s to 6 m/s

Here, the comparison of the discrete-time LPV system against the nonlinear model is made assuming a ramping wind speed in the below-rated operating region. The axial hub-height wind speed begins at the cut-in speed, 3 m/s, and ramps up until 6 m/s. Fig. 6.2 shows the dynamic response of both models under the ramping wind input. As seen, the discretised LPV system is able to capture the variations in the motion of the turbine DOFs due to the ramping wind. The tower side-side and collective cosine and sine motions are negligible as the wind is applied in the axial direction. The dominant modes are the tower fore-aft z_H and the collective flap $a_{\beta,1}$.

As seen, at the start of the simulation, the system is excited with the initial wind speed of, i.e., 3 m/s, which causes the degrees of freedom to start oscillating. These oscillations begin to die out as a result of the structural and aerodynamic damping. Then, the wind speed starts ramping up at time instant 20 s and increases linearly until it reaches 6 m/s at time 100 s. This ramping wind speed causes the degrees of freedom to vary throughout this period, eventually reaching the final steady-state value once the final wind speed is maintained constant.

Ramping wind speed from 7 m/s to 10 m/s

Fig. 6.3 presents the dynamic response of the discrete-time LPV system and that of the nonlinear model. In this case, the simulation begins at the below-rated operational region and ends in above-rated conditions —the initial wind speed is 7 m/s and the final is 10 m/s. The linear model is in good agreement with the nonlinear model as it is capable of following the variation in wind speed, as well as reaching the same final equilibrium state. Besides, the wind inflow is an axial wind at the tower hub-height. This results in the dominant degrees of freedom being the tower fore-aft motion z_H and the collective flapwise

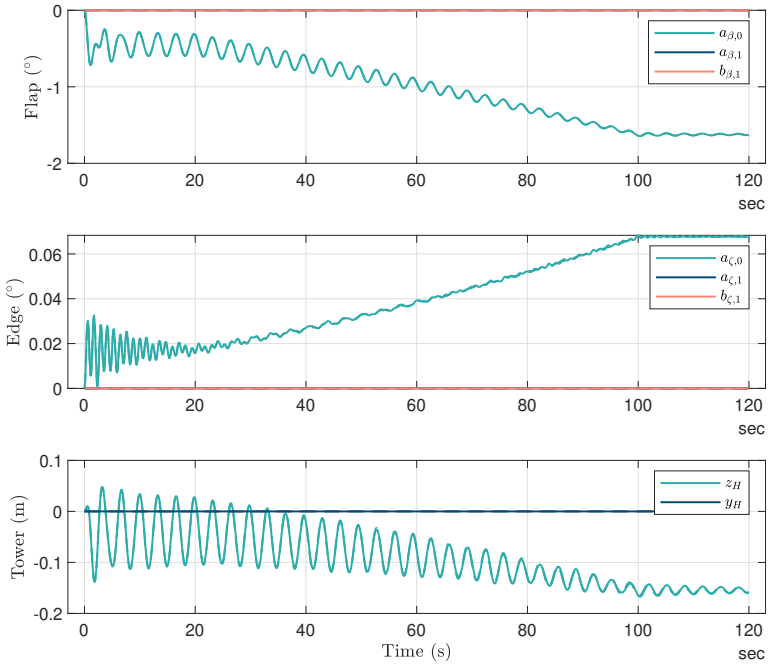

Figure 6.2: Response of the analytical WT linear model (solid) and the nonlinear model (dashed) under uniformly ramping wind from 3 m/s to 6 m/s

degree of freedom $a_{\beta,0}$. Some collective edgewise contribution ($a_{\zeta,0}$) can also be seen. The excitation of the rotor cosine and sine modes, $a_{(\cdot),1}$ and $b_{(\cdot),1}$, is negligible in both flap and edge, and so it the tower side-side motion y_H.

Also, small excitations can be seen throughout the linearly ramping region due to the change of operating point in the LPV system. Specifically, this behaviour can be seen in the edgewise collective coordinate $a_{\zeta,1}$. Such behaviour is known as the switching effect of linear parameter-varying systems. As expected, the deflections of the system are higher than in the below-rated case due to the wind speed being higher, which results in larger aerodynamic forces and moments. The oscillations also decay more rapidly as a result of larger aerodynamic damping. In general, the response of the linear model matches well the dynamic behaviour of the nonlinear model.

Ramping wind speed from 17 m/s to 20 m/s

Last, Fig. 6.4 shows the comparison of the dynamic behaviour of the discretised LPV to that of the nonlinear model. In this case, the turbine is operating under high wind speeds since the ramping wind ranges from 17 m/s to 20 m/s over the course of the simulation. The linear model is still in fairly good agreement with the nonlinear dynamics. The tower fore-aft motion of the linear model, however, oscillates throughout the period with ramping wind speed, which differs from the nonlinear model. The switching effect of the LPV system can also be seen as the system is somewhat excited due to the change of operating point.

Overall, the LPV system is capable of following the variation in the dynamic behaviour due to a ramping wind speed. These results have a particularly good match at low to mid-range wind speeds. Besides, it is also able to capture the changes around rated conditions, where the turbine varies its rotational speed and blade pitch angle. At high wind speeds, the effects of LPV switching become more important, and the simulations present more differences.

6.3.3. Turbulent ramp wind

Similarly, the dynamic behaviour of the linear analytical wind turbine model is compared against its nonlinear model. The simulations run for 120 s, with a turbulent and linearly ramping axial wind at the

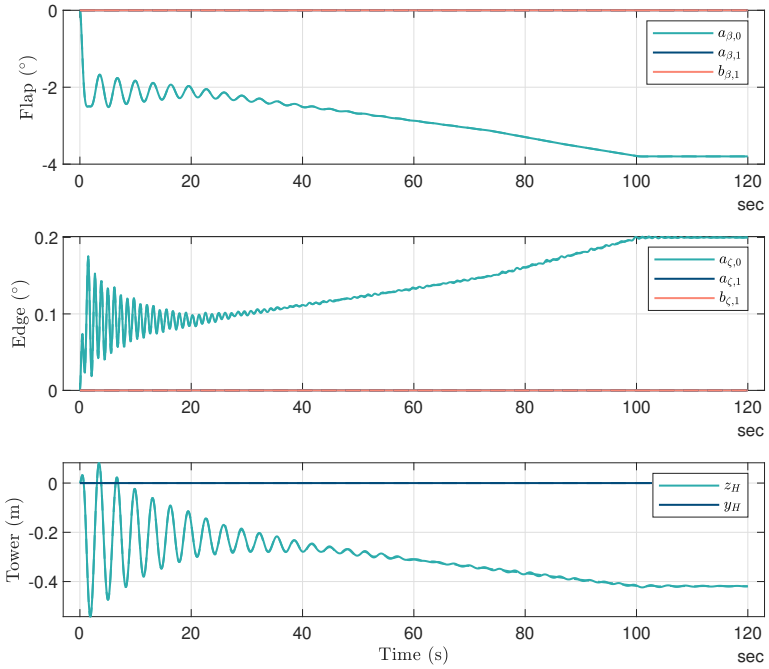

Figure 6.3: Response of the analytical WT linear model (solid) and the nonlinear model (dashed) under uniformly ramping wind from 7 m/s to 10 m/s

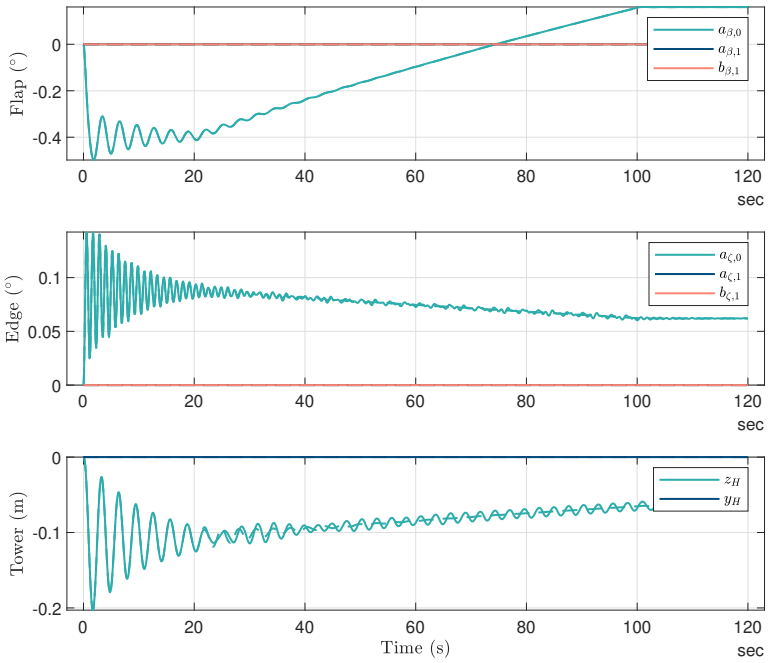

Figure 6.4: Response of the analytical WT linear model (solid) and the nonlinear model (dashed) under uniformly ramping wind from 17 m/s to 20 m/s

hub-height. The wind speed is assumed to increase linearly over the time interval from 20 s to 100 s, with a turbulence time series added onto it. Outside this interval, the mean values are kept constant at the initial and final values, respectively. Again, the turbine is described in the ground-fixed coordinate frame, which uses the collective, cosine and sine coordinates to describe the rotations of the blades both in edge and in flap. The LPV system is composed by the LTI systems extracted at the operating points ranging from the cut-in speed (3 m/s) to the cut-out speed (25 m/s) with steps of 0.2 m/s. The discretisation time step used to discretise the LPV system is $T_\mathrm{d} = 0.1$ s. Moreover, the LPV model is

represented in the affine LPV form to account for the offsets in the input and the state variables.

Turbulent wind

The wind turbine model only has as input the wind speed in the longitudinal direction. The turbulence wind series is obtained using the Kaimal spectral models, which describes the single-sided velocity spectrum as [12]:

$$S(f) = \frac{4\sigma_1^2 f L_1/U_{hub}}{(1+6fL_1/U_{hub})^{5/3}} \tag{6.15}$$

where f is the cyclic frequency, σ is the standard deviation of velocity component, L_1 is the integral length scale, and U_{hub} is the mean wind speed at hub height. The parameters of the Kaimal model have been adjusted to meet the IEC [15] standard, for which $L_1 = 8.1\Lambda_1$ when considering the wind speed longitudinal component, with $\Lambda_1 = 42$ m for hub-heights over 60 m, as is the case. For example, Fig. 6.5 shows the Kaimal spectral density and the 10-min time series of the longitudinal turbulent wind speed considering a 10 m/s hub-height wind speed and turbulence intensity of 10%. As seen, the main energy contribution occurs at frequencies under 1 Hz.

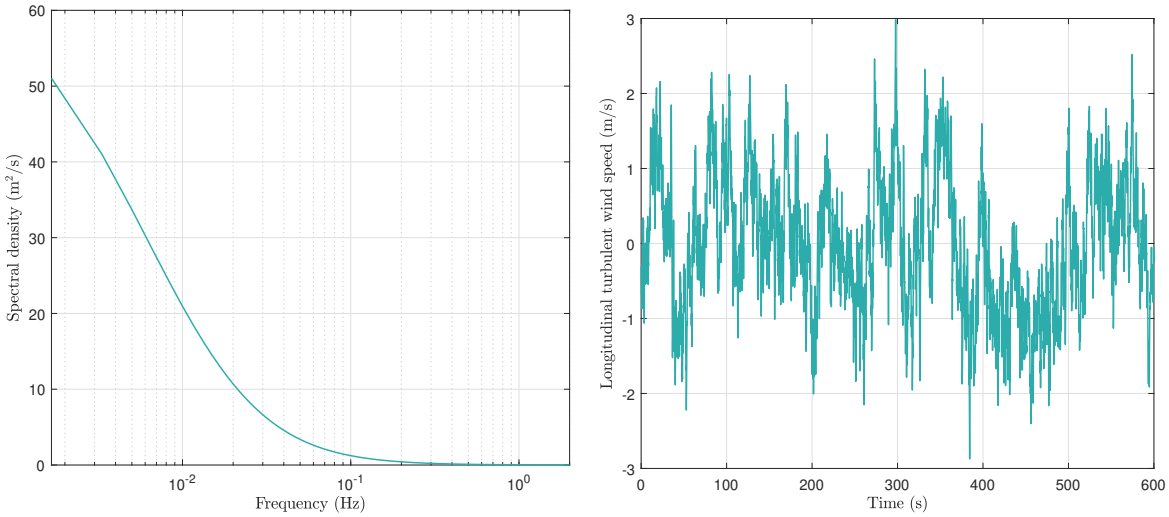

(a) Kaimal spectrum

(b) Turbulent wind speed time series

Figure 6.5: Kaimal spectrum derived for a mean hub-height wind speed of 10 m/s and a turbulence intensity of 10%

The wind turbine class is assumed to be class IIB (medium wind) of the IEC 61400 standard. Thus, $I_{ref} = 0.14$ is used for the hub-height turbulence intensity at a 10-min average wind speed of 15 m/s, and the reference 10-min average wind speed is $U_{ref} = 42.5$ m/s. The turbulence intensity is computed using the normal turbulence model (NTM) as per the IEC 61400-1 standard [15], for which the value of the turbulence standard deviation is calculated as:

$$\sigma_1 = I_{ref}\,(0.75\,U_{hub} + b), \quad \text{with } b = 5.6 \text{ m/s} \tag{6.16}$$

where the values of the hub-height wind speed must fall within the range from $0.2\,U_{ref}$ to $0.4\,U_{ref}$, and the turbulence intensity is then given by $TI = \sigma_1/U_{hub}$.

Three simulations are tested to evaluate the performance of the discretised LPV model. All simulations run for 600 s and use wind speed time series extracted from the Kaimal spectral model. The simulations are performed using various random turbulence time series with a different seed for each case. First, the analytical wind turbine model is used to simulate the dynamic response of the model under a turbulent inflow with constant mean wind speed. The velocity fluctuations are due to the turbulence. Second, the models are used to simulate the response to a turbulent ramping wind speed. The turbulence time series is added onto a uniformly ramping wind speed in time. For all cases, the linear parameter-varying model is compared against the nonlinear model.

Mean wind speed 5 m/s and turbulence intensity 26%

The performance of the linear model is compared against the response of the nonlinear model, where the wind turbine is subject to a 5 m/s mean hub-height wind speed and 26% turbulence intensity, calculated according to the NTM. The simulations run in below-rated operating conditions. For clarity, Fig. 6.6 provides a 200 s window of the simulation and compares the response of the analytical LPV model with that of the nonlinear model. Similar to the results above, the wind speed acts in the axial direction and does not excite the tower side-side mode. The cosine and sine collective modes are also negligible both in edge and in flap, and the predominant motion is the collective flap $a_{\beta,0}$ and the tower fore-aft displacements z_H. The response of the linear model is in good agreement with that of the nonlinear model, and it is able to adjust to the velocity fluctuations due to turbulence.

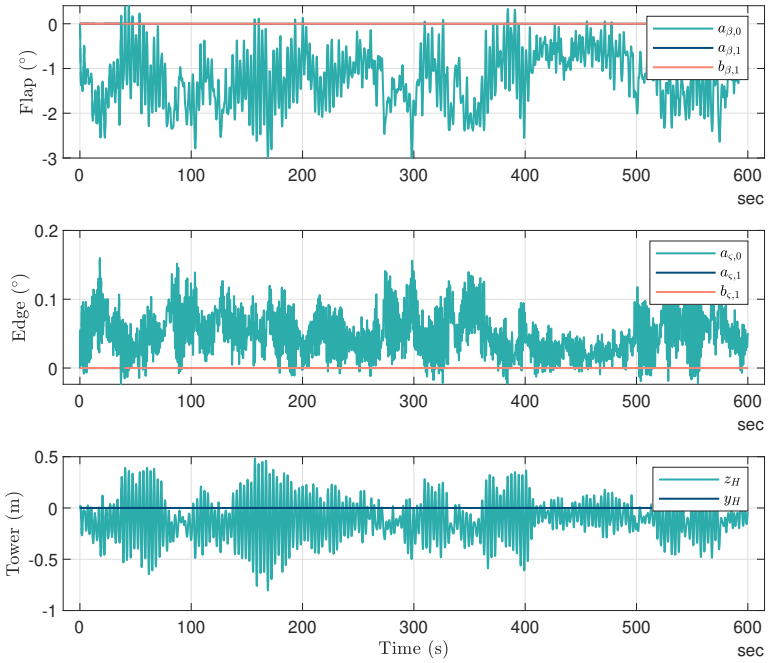

Figure 6.6: Response of the analytical WT linear model (solid) and the nonlinear model (dashed) under a 5 m/s turbulent with 26% turbulence intensity

Mean wind speed 9 m/s and turbulence intensity 19%

Here, the linear model is compared against the nonlinear model under a 9 m/s mean hub-height wind speed and 19% turbulence intensity, calculated according to the NTM. The rated wind speed of the simple wind turbine model is 9 m/s. Thus, throughout the simulation, the wind turbine continuously switches from below-rated to above-rated operating conditions. Fig. 6.7 shows the comparison of the response of the analytical LPV model with that of the nonlinear model. Overall, the linear model properly predicts the motion of the wind turbine over time. The amplitude of the oscillations slightly differs between both models, which can be seen particularly in the collective edgewise coordinate $a_{\zeta,0}$.

Ramping wind speed from 15 m/s to 18 m/s and turbulence intensity 16%

Fig. 6.8 shows the comparison between the LPV system and the nonlinear model under a ramping wind speed from 15 m/s until 18 m/s, superposed with a turbulent wind speed computed from the Kaimal spectrum using a 16% turbulence intensity, calculated from to the normal turbulence model. Throughout the simulation, the wind turbine is mostly in above-rated operating conditions and switches to below-rated at some instants due to the velocity fluctuations. Similarly to the simulations above, the wind speed acts in the axial direction and does not excite the tower side-side mode. The cosine and sine collective modes are also negligible both in edge and in flap, and the predominant motion is the

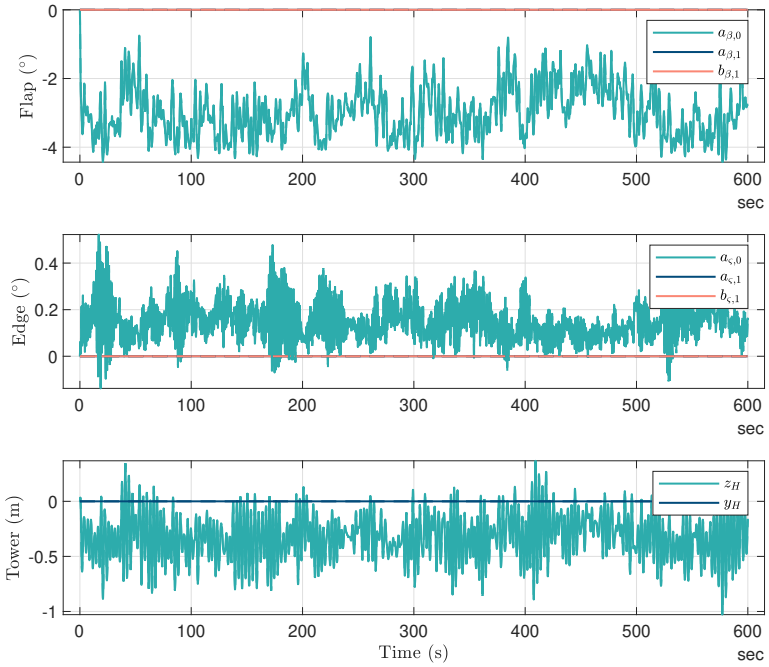

Figure 6.7: Response of the analytical WT linear model (solid) and the nonlinear model (dashed) under a 9 m/s turbulent with 19% turbulence intensity

collective flap $a_{\beta,0}$ and the tower fore-aft displacements z_H. The linear system is able to adjust to the velocity fluctuations due to turbulence, as the response fully matches that of the nonlinear model.

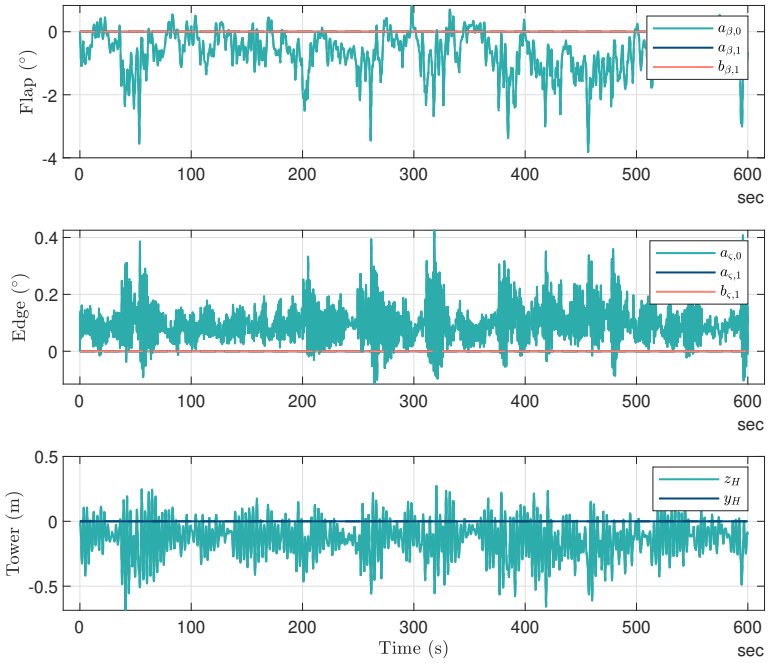

Figure 6.8: Response of the analytical WT linear model (solid) and the nonlinear model (dashed) under a ramping turbulent wind from 15 m/s mean to 18 m/s and 15% turbulence intensity

In summary, for the applications above, the nonlinear behaviour of the analytical wind turbine model is modelled as an array of LTI systems obtained at a series of scheduling parameter values and evaluated in the discrete-time domain. The resulting linear parameter-varying system is seen to approximate well the original nonlinear system for scenarios in isotropic conditions. Besides, it provides a fast simulation

method for evaluating the dynamic behaviour of a wind turbine.

6.4. Numerical results: BHawC linearised model

As described in the previous sections, the linear parameter-varying (LPV) system is formulated in the affine form. By doing so, the state-space configuration of the system can be taken into consideration. For this reason, the methodology implemented regarding the LPV system requires using the offsets in the inputs and state variables to get the response of the model. For the linearised BHawC model, the equilibrium configuration of the state variable must be extracted from BHawC. Once the offsets of the inputs and the state variables, $\tilde{\mathbf{u}}$ and $\tilde{\mathbf{x}}$, are obtained, the LPV model can be evaluated in the discrete-time domain, where the state update vector and the response of the system at each time system are calculated as follows:

$$\begin{aligned} \mathbf{x}(k+1) &= \mathbf{A}_\mathrm{d}(\mathbf{p}_\mathrm{d})\,(\mathbf{x}(k) - \tilde{\mathbf{x}}(\mathbf{p}_\mathrm{d})) + \mathbf{B}_\mathrm{d}(\mathbf{p}_\mathrm{d})\,(\mathbf{u}(k) - \tilde{\mathbf{u}}(\mathbf{p}_\mathrm{d})) + \tilde{\mathbf{x}}(\mathbf{p}_\mathrm{d}) \\ \mathbf{y}_{gf}(k) &= \mathbf{C}_\mathrm{d}(\mathbf{p}_\mathrm{d})\,(\mathbf{x}(k) - \tilde{\mathbf{x}}(\mathbf{p}_\mathrm{d})) + \mathbf{D}_\mathrm{d}(\mathbf{p}_\mathrm{d})\,(\mathbf{u}(k) - \tilde{\mathbf{u}}(\mathbf{p}_\mathrm{d})) + \tilde{\mathbf{y}}(\mathbf{p}_\mathrm{d})\,. \end{aligned} \tag{6.17}$$

where $\mathbf{A}_\mathrm{d}$, $\mathbf{B}_\mathrm{d}$, $\mathbf{C}_\mathrm{d}$ and $\mathbf{D}_\mathrm{d}$ are the discretised matrices of the state-space formulation, and $\tilde{\mathbf{u}}$ and $\tilde{\mathbf{x}}$ correspond to the offset in the inputs and the state variables.

However, the BHawC model represents the orientations of the nonlinear configuration differently from those in the linear model. While the nonlinear configuration describes the orientations using unit quaternions, the model linearised around that configuration uses three angles. Therefore, whilst the procedure to simulate the output of the LPV model is readily implemented, the steady-state configuration of the linear model cannot currently be used to assess the response of the linear model. For future developments, the configurations of the state variables could be modified to get matching descriptions for the linear and nonlinear models. A possible approach to achieve the continuity in the rotational state variables from BHawC is to convert the quaternion representation into Tait-Bryan angles and rotating the linear model —which is currently in global coordinates— into the orientations at the steady-state equilibrium. Nevertheless, some results of the applied methodology are explained below, as well as the required computational times to get the loads on the system.

6.4.1. Considerations of computational times

As the method of obtaining the response of the time-varying parameter system is developed, an overview of the computational times of the procedure is given. The linear LPV model consists of an array of linear time-invariant systems collected for each scheduling parameter value in the grid space. Thus, at first, the state-space system is extracted at each operating point, which takes around 1.5 s to compute. Then, getting the reduced-order model to approximate the full system with lower complexity takes another 8 s per operating point. Moreover, getting the discretised matrices of the state-space model takes around 2 s per grid point. Finally, evaluating the response on the system takes around 10 s for a simulation lasting 300 s. In short, although using ROMs to get the response of the system is very beneficial in terms of run times, reducing the model at each grid point can become a time-consuming process.

6.4.2. Uniform wind ramp

The dynamic response of the linearised BHawC model is compared to the results of the nonlinear BHawC code. The simulation runs for 300 s, where the wind turbine is subject to a linearly ramping wind. Initially, the wind speed is 8 m/s. Then, it starts to ramp up uniformly in time until the wind reaches 11 m/s. This final wind speed is maintained until the end of the simulation. Also, the wind speed is applied along the rotor axis, which causes the dominant motion to be that of the tower fore-aft degree of freedom ξ_y. For this case, the LPV system contains an array of LTI systems extracted every 0.3 m/s, which are discretised to evaluate the solution in the discrete-time (DT) domain.

Fig. 6.9 shows the dynamic response of the tower-top node of both models under the aforementioned

wind speed. In the results from the BHawC simulations, the degrees of freedom of the tower-top node increase linearly throughout the simulation due to the rising wind speed. Once the final wind speed is kept constant, the displacements reach their final steady-state values. Rather, the response of the linear system shows a step-like behaviour where the displacements receive an excitation when the model switches between operational points.

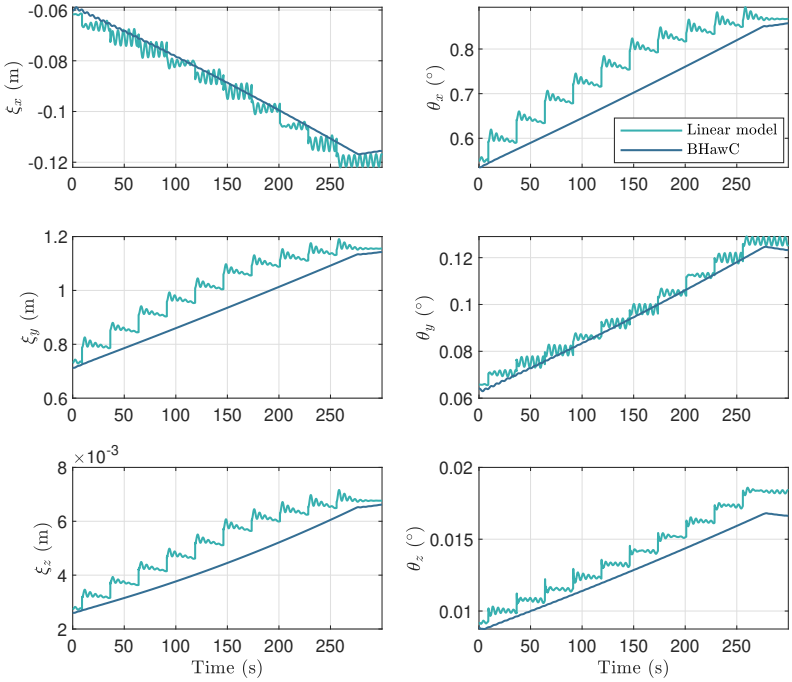

Figure 6.9: Response of the tower-top displacements under a uniformly ramping wind from 8 m/s mean to 11 m/s. Comparison between the linear model and BHawC

As explained above, the methodology requires using the offsets in the inputs as well as the equilibrium configuration for each grid point in the linear parameter-varying scheduling domain. The latter, however, cannot be extracted from BHawC using the same description for the rotational states as that in the linear model. Thus, at this stage, the equilibrium configurations cannot be used in the LPV methodology. As a consequence, when the LPV parameter switches between operating points, the system receives as input an excitation much higher than that in the nonlinear model. As a result, the response of the system begins to oscillate, and the output presents the step-like performance as seen in Fig. 6.9. In summary, not accounting for the offsets in the system's steady-state configuration causes the LPV model not to capture the response of the system to a ramping variation in the wind speed properly. The same occurs for simulations under turbulent wind speeds.

7

Conclusions and recommendations

This chapter reviews the most relevant results found throughout this thesis work and makes recommendations on improvements to the model and the analysis for future work to be done on the topic.

7.1. Conclusions

The main objective of this thesis was to develop a fast linear state-space model based on the BHawC code to reduce the computational times required to assess the loads on wind turbines subject to turbulent wind inflows. The contributions of the work lie in several factors. First, a state-space system of the linearised BHawC model was implemented based on the work of Skjoldan [32], previously developed for modal analysis; the existing linear model contained the system matrix. In addition, the input and output matrices of the state-space formulation were derived in this research using an analytically-based methodology. While the input matrix relates the free wind input to the state variables, the output matrix relates the states to the internal loads of the structure.

A methodology to evaluate the loads on wind turbines in isotropic environmental conditions was developed using the linearised BHawC model. First, the system was assumed to be an isotropic wind turbine in isotropic external conditions and low turbulence intensity. Accordingly, the Coleman transformation was used to eliminate the periodic content in the equations of motion. The loads on the wind turbine were then evaluated by modelling the system as a linear time-invariant (LTI) system. The developed state-space model is a large, sparse model. Consequently, using model order reduction (MOR) methods allowed to reduce the complexity of the system and the computational requirements of the simulations. Specifically, the approach used was the balanced truncation (BT) method, which allowed getting reduced-order models to approximate the main dynamics of the nonlinear model whilst preserving the stability of the system.

The loads on the turbine were evaluated using a frequency-domain approach, where the transfer function was computed to get the system response to an arbitrary wind input. The computation of the transfer function of the full-order model (FOM) was computationally expensive, defeating the purpose of this study. Using the reduced-order models (ROMs), however, was seen to be very beneficial for speeding up the process. In addition, other approaches to improve the computation times of the simulations were examined, such as using the numerical tools in PETSc to compute the transfer function of LTI systems.

For this study, the linearised model was compared against the nonlinear BHawC code both through time-domain simulations and by comparing the power spectral densities of the response. First, the simulations were compared assuming a rectangular wind step at two operating points. The tower-top displacements and the tower-bottom loads were studied to assess the performance of the model. From the time-domain responses and power spectral densities, the models are in good agreement, and the

linear time-invariant (LTI) system captures the dynamics of the nonlinear model. Second, the wind inflow was assumed to be a low turbulence wind speed. Again, the states of the tower-top node and the loads at the tower base were evaluated. From the time series, the displacements and loads related to the longitudinal and vertical motions are in fairly good agreement with the nonlinear model and present maximum root-mean-square errors of around 10%. However, the states regarding the side-side motion present large discrepancies from the nonlinear model, with normalised RMSEs up to 20%. A fatigue analysis was performed to estimate the damage equivalent loads (DELs) based on the rainflow counting algorithm. The tower-base fore-aft and the tower-top torsion moments present differences up to 20%, whereas the tower-base side-side are largely overpredicted.

Second, the wind turbine was assumed to be an isotropic system subject to a highly-turbulent wind. The high turbulence intensity causes the wind turbine to quickly shift between operating regions. These shifts become more important for wind speeds around rated. Thus, using a linear time-invariant model was no longer suitable for describing the dynamic behaviour of the nonlinear model. Under such conditions, the loads of the wind turbine were evaluated by approximating the nonlinear BHawC model as a linear parameter-varying (LPV) system. Again, the balanced-truncation (BT) model order reduction method was used to reduce the complexity of the system and, thus, the computational times of the simulations. To further speed up the calculations, the LPV system was converted to the discrete-time domain by discretising the matrices of the state-space model.

The implemented approach uses the affine form of the grid-based approach for the assembly and evaluation of the LPV system and, therefore, requires using the equilibrium configuration of the state variables and the inputs. In the BHawC model, however, the orientations of the nonlinear configurations are described differently than in the linearised model. Therefore, although the framework of the analysis was implemented, it was not possible to examine the performance of the linear model in comparison to the results from BHawC. Instead, the analytical wind turbine model developed by Riva [24] was used to validate the methodology and to compare the performance of the linear model to the response of the nonlinear model. The discrete-time LPV system is able to capture the fluctuations in the operating conditions and approximates well the nonlinear behaviour of the turbine. Moreover, the simulations using the linear parameter-varying (LPV) system require much less computational time than the simulations of the nonlinear model.

7.2. Recommendations for future work

The presented linearised BHawC model could be further developed to include the aerodynamic loads on other wind turbine substructures such as tower and nacelle, as well as accounting for the unsteady aerodynamics in the state-space input matrix or adding dynamic wake models. Besides, the linearised BHawC model could become an aero-servo-elastic model by integrating a linearised controller. Adding a controller would also require developing the formulation for the feedforward matrix of the state-space model. The model could also be further developed for offshore wind applications by considering the hydrodynamic loads on the system. In addition, in light of wanting to reduce the computational expense of the simulations using LTI systems, other approaches could be further investigated to get the transfer function, such as using a GPU for the operations.

Related to the applicability of the linear parameter-varying (LPV) system, it is recommended that future work is dedicated to obtaining a matching representation of the rotational state variables of both systems. In case of achieving continuity in the description of the nodal orientations between the BHawC nonlinear model and the linearised model, the equilibrium configurations could be used as offsets to the LPV system. Thereby, the response of the LPV system could be compared to the loads in the BHawC simulations. Besides, the most time-consuming aspect of the LPV methodology is that of getting the reduced-order model (ROM) at each value of the scheduling parameter. That being so, it would be interesting to explore other model order reduction (MOR) techniques that require less computational effort while still capturing the main information of the nonlinear system.

Finally, it is strongly encouraged for future investigations to extend the work in this study to deal with wind turbines in anisotropic conditions, i.e., rotor unbalance, gravitational forcing, or wind shear. In anisotropic conditions, the blades experience different conditions in their rotation around the rotor, introducing further sources of periodicity into the system. To account for the periodicity of such systems, the system should be modelled as a linear time-periodic (LTP) system. The harmonic transfer function (HTF) concept could be employed to get the response of the linearised model. Furthermore, the LPV approach can also be used to model the system in anisotropic conditions. In that view, the implemented approach could also be extended to account for the time variation of other scheduling parameters, i.e., the azimuthal position of the blades.

References

[1] Chair of Automatic Control, "sssMOR Toolbox," Technical University of Munich, Munich, Tech. Rep. [Online]. Available: https://www.epc.ed.tum.de/en/rt/forschung/modellordnungsreduktion/software/sssmor/.

[2] M. Hall, S. Housner, D. Zalkind, P. Bortolotti, D. Ogden, and G. Barter, "An Open-Source Frequency-Domain Model for Floating Wind Turbine Design Optimization," *Journal of Physics: Conference Series*, vol. 2265, no. 4, p. 042 020, May 2022. DOI: 10.1088/1742-6596/2265/4/042020. [Online]. Available: https://iopscience.iop.org/article/10.1088/1742-6596/2265/4/042020.

[3] Satish Balay *et al.*, *KSP: Linear System Solvers*, 2022. [Online]. Available: https://petsc.org/main/docs/manual/ksp/?highlight=ksp.

[4] Satish Balay *et al.*, *PETSc 3.17*, 2022. [Online]. Available: https://petsc.org/.

[5] The MathWorks Inc., *Model Reduction Basics*, 2022. [Online]. Available: https://se.mathworks.com/help/control/ug/about-model-order-reduction.html.

[6] ——, *Piecewise Cubic Hermite Interpolating Polynomial (PCHIP)*, 2022. [Online]. Available: https://se.mathworks.com/help/matlab/ref/pchip.html.

[7] ——, *Practical Introduction to Frequency-Domain Analysis*, 2022. [Online]. Available: https://se.mathworks.com/help/signal/ug/practical-introduction-to-frequency-domain-analysis.html.

[8] P. den Boef, P. B. Cox, and R. Tóth, "LPVcore: MATLAB Toolbox for LPV Modelling, Identification and Control," *IFAC-PapersOnLine*, vol. 54, no. 7, pp. 385–390, Jan. 2021. DOI: 10.1016/J.IFACOL.2021.08.390.

[9] D. D. Bueno and E. H. Dowell, "A note on the state space representation of aeroelastic systems for time domain analysis," *Journal of Fluids and Structures*, vol. 104, p. 103 294, Jul. 2021. DOI: 10.1016/j.jfluidstructs.2021.103294. [Online]. Available: https://linkinghub.elsevier.com/retrieve/pii/S0889974621000773.

[10] K. Lu *et al.*, "A Review of Model Order Reduction Methods for Large-Scale Structure Systems," *Shock and Vibration*, vol. 2021, Z. Lu, Ed., pp. 1–19, May 2021. DOI: 10.1155/2021/6631180. [Online]. Available: https://www.hindawi.com/journals/sv/2021/6631180/.

[11] National Renewable Energy Laboratory, *RAFT*, 2021. [Online]. Available: https://openraft.readthedocs.io/en/latest/index.html.

[12] R. M. Putri, C. Obhrai, J. B. Jakobsen, and M. C. Ong, "Numerical Analysis of the Effect of Offshore Turbulent Wind Inflow on the Response of a Spar Wind Turbine," *Energies*, vol. 13, no. 10, p. 2506, May 2020. DOI: 10.3390/en13102506. [Online]. Available: https://www.mdpi.com/1996-1073/13/10/2506.

[13] R. Riva, "Stability analysis of wind turbines," 2020.

[14] The MathWorks Inc., *Simulate Linear Parameter-Varying (LPV) systems*, 2020. [Online]. Available: https://se.mathworks.com/help/control/ref/lpvsystem.html.

[15] International Electrotechnical Commission, "IEC 61400-1:2019: Wind energy generation systems - Part 1: Design requirements," Geneva, 2019. [Online]. Available: https://webstore.iec.ch/publication/26423.

[16] F. J. Madsen, A. Pegalajar-Jurado, and H. Bredmose, "Performance study of the QuLAF pre-design model for a 10 MW floating wind turbine," *Wind Energy Science*, vol. 4, no. 3, pp. 527–547, Sep. 2019. DOI: 10.5194/wes-4-527-2019. [Online]. Available: https://wes.copernicus.org/articles/4/527/2019/.

[17] Maria Cruz Varona, Alessandro Castagnotto, Thomas Wolf, Rudy Eid, and Mikhail Pak, "Modeling and Reduction of Complex Systems," in Munich, Jul. 2019, ch. Part B.

[18] Timothy A. Davis, *Suitesparse: a suite of sparse matrix software*, 2019. [Online]. Available: https://people.engr.tamu.edu/davis/suitesparse.html.

[19] P. J. Couturier and P. F. Skjoldan, "Implementation of an advanced beam model in BHawC," *Journal of Physics: Conference Series*, vol. 1037, no. 6, p. 062 015, Jun. 2018. DOI: 10.1088/1742-6596/1037/6/062015. [Online]. Available: https://iopscience.iop.org/article/10.1088/1742-6596/1037/6/062015.

[20] A. Pegalajar-Jurado, M. Borg, and H. Bredmose, "An efficient frequency-domain model for quick load analysis of floating offshore wind turbines," *Wind Energy Science*, vol. 3, no. 2, pp. 693–712, Oct. 2018. DOI: 10.5194/wes-3-693-2018. [Online]. Available: https://wes.copernicus.org/articles/3/693/2018/.

[21] A. Castagnotto, M. Cruz Varona, L. Jeschek, and B. Lohmann, "sss & sssMOR: Analysis and reduction of large-scale dynamic systems in MATLAB," *At-Automatisierungstechnik*, vol. 65, no. 2, pp. 134–150, Feb. 2017. DOI: 10.1515/AUTO-2016-0137.

[22] S. Krenk and P. J. Couturier, "Equilibrium-Based Nonhomogeneous Anisotropic Beam Element," *AIAA Journal*, vol. 55, no. 8, pp. 2773–2782, Aug. 2017. DOI: 10.2514/1.J055884. [Online]. Available: https://arc.aiaa.org/doi/10.2514/1.J055884.

[23] T. M. Letcher, "Why Wind Energy?" *Wind Energy Engineering: A Handbook for Onshore and Offshore Wind Turbines*, pp. 3–14, Jan. 2017. DOI: 10.1016/B978-0-12-809451-8.00001-1.

[24] R. Riva, S. Cacciola, and C. L. Bottasso, "Periodic stability analysis of wind turbines operating in turbulent wind conditions," *Wind Energy Science*, vol. 1, no. 2, pp. 177–203, Oct. 2016. DOI: 10.5194/wes-1-177-2016. [Online]. Available: www.wind-energ-sci.net/1/177/2016/%20https://wes.copernicus.org/articles/1/177/2016/.

[25] J. N. Sørensen, *General Momentum Theory for Horizontal Axis Wind Turbines*, 1st ed., ser. Research Topics in Wind Energy. Cham: Springer Cham, 2016, vol. 4, ISBN: 978-3-319-22113-7. DOI: 10.1007/978-3-319-22114-4. [Online]. Available: http://link.springer.com/10.1007/978-3-319-22114-4.

[26] C. Tibaldi, L. C. Henriksen, M. H. Hansen, and C. Bak, "Wind turbine fatigue damage evaluation based on a linear model and a spectral method," *Wind Energy*, vol. 19, no. 7, pp. 1289–1306, Jul. 2016. DOI: 10.1002/we.1898. [Online]. Available: https://onlinelibrary.wiley.com/doi/10.1002/we.1898.

[27] M. Hansen, *Aerodynamics of Wind Turbines*. Routledge, May 2015, ISBN: 9781317671039. DOI: 10.4324/9781315769981. [Online]. Available: https://www.taylorfrancis.com/books/9781317671039.

[28] A. Hjartarson, P. Seiler, and A. Packard, "LPVTools: A Toolbox for Modeling, Analysis, and Synthesis of Parameter Varying Control Systems," *IFAC-PapersOnLine*, vol. 48, no. 26, pp. 139–145, 2015. DOI: 10.1016/j.ifacol.2015.11.127. [Online]. Available: www.sciencedirect.com%20https://linkinghub.elsevier.com/retrieve/pii/S240589631502385X.

[29] D. Infield, "Wind Energy," *Future Energy: Improved, Sustainable and Clean Options for our Planet*, Jan. 2014. DOI: 10.1016/B978-0-08-099424-6.00015-6.

[30] M. S. Allen, M. W. Sracic, S. Chauhan, and M. H. Hansen, "Output-only modal analysis of linear time-periodic systems with application to wind turbine simulation data," *Mechanical Systems and Signal Processing*, vol. 25, no. 4, pp. 1174–1191, May 2011. DOI: 10.1016/j.ymssp.2010.12.018. [Online]. Available: https://linkinghub.elsevier.com/retrieve/pii/S0888327011000100.

[31] M. Dahleh, M. A. Dahleh, and G. Verghese, "Lectures on Dynamic Systems and Control," Massachuasetts Institute of Technology, Tech. Rep., 2011. [Online]. Available: https://ocw.mit.edu/courses/electrical-engineering-and-computer-science/6-241j-dynamic-systems-and-control-spring-2011/readings/MIT6_241JS11_chap07.pdf.

[32] P. F. Skjoldan, "Aeroelastic modal dynamics of wind turbines including anisotropic effects," Ph.D. dissertation, Danmarks Tekniske Universitet, 2011, ISBN: 978-87-550-3848-6. [Online]. Available: https://orbit.dtu.dk/files/5509069/ris-phd-66.pdf.

[33] G. S. Bir, "User's Guide to MBC3: Multi-Blade Coordinate Transformation Code for 3-Bladed Wind Turbines," National Renewable Energy Laboratory (NREL), Golden, CO (United States), Tech. Rep. NREL/TP-500-44327, Sep. 2010. DOI: 10.2172/989416. [Online]. Available: http://www.osti.gov/servlets/purl/989416-tPlWK1/.

[34] P. F. Skjoldan, "BHawC equations of motion," Siemens Wind Power A/S, Tech. Rep., 2010.

[35] R. Tóth, "Discretization of LPV Systems," in *Modeling and Identification of Linear Parameter-Varying Systems*, vol. 403, Berlin, Heidelberg: Springer Berlin Heidelberg, 2010, pp. 143–169. DOI: 10.1007/978-3-642-13812-6_6. [Online]. Available: http://link.springer.com/10.1007/978-3-642-13812-6_6.

[36] S. Bittanti and P. Colaneri, *Periodic Systems*, ser. Communications and Control Engineering July. London: Springer London, 2009, ISBN: 978-1-84800-910-3. DOI: 10.1007/978-1-84800-911-0. [Online]. Available: http://link.springer.com/10.1007/978-1-84800-911-0.

[37] G. Bir, "Multi-Blade Coordinate Transformation and its Application to Wind Turbine Analysis," in *46th AIAA Aerospace Sciences Meeting and Exhibit*, Reston, Virigina: American Institute of Aeronautics and Astronautics, Jan. 2008, ISBN: 978-1-62410-128-1. DOI: 10.2514/6.2008-1300. [Online]. Available: https://arc.aiaa.org/doi/10.2514/6.2008-1300.

[38] A. C. Antoulas, *Approximation of Large-Scale Dynamical Systems*. Society for Industrial and Applied Mathematics, Jan. 2005, ISBN: 978-0-89871-529-3. DOI: 10.1137/1.9780898718713. [Online]. Available: http://epubs.siam.org/doi/book/10.1137/1.9780898718713.

[39] V. Mehrmann and T. Stykel, "Balanced Truncation Model Reduction for Large-Scale Systems in Descriptor Form," in *Dimension Reduction of Large-Scale Systems*, Berlin/Heidelberg: Springer-Verlag, Oct. 2005, pp. 83–115. DOI: 10.1007/3-540-27909-1_3. [Online]. Available: http://link.springer.com/10.1007/3-540-27909-1_3.

[40] R. Rubak, J. T. Petersen, and Siemens Wind, "Monopile as Part of Aeroelastic Wind Turbine Simulation Code," Siemens Wind Power A/S, Brande, 2005. [Online]. Available: https://citeseerx.ist.psu.edu/viewdoc/download?doi=10.1.1.604.8266&rep=rep1&type=pdf.

[41] M. Salleras *et al.*, "Comparison of model order reduction methodologies for thermal problems," in *EuroSimE 2005. Proceedings of the 6th International Conference on Thermal, Mechanial and Multi-Physics Simulation and Experiments in Micro-Electronics and Micro-Systems, 2005.*, IEEE, 2005, pp. 60–65, ISBN: 0-7803-9062-8. DOI: 10.1109/ESIME.2005.1502773. [Online]. Available: http://ieeexplore.ieee.org/document/1502773/.

[42] B. N. Datta, "Linear state-space models and solutions of the state equations," *Numerical Methods for Linear Control Systems*, pp. 107–157, Jan. 2004. DOI: 10.1016/B978-012203590-6/50009-4.

[43] M. H. Hansen, "Improved Modal Dynamics of Wind Turbines to Avoid Stall-induced Vibrations," *Wind Energy*, vol. 6, no. 2, pp. 179–195, Apr. 2003. DOI: 10.1002/we.79. [Online]. Available: https://onlinelibrary.wiley.com/doi/10.1002/we.79.

[44] A. Björck, "AERFORCE: subroutine package for unsteady blade-element momentum calculations," The Aeronautical Research Institute of Sweden, Bromma (Sweden), Tech. Rep., 2000. [Online]. Available: https://www.osti.gov/etdeweb/biblio/20104443.

[45] N. M. Wereley, "Analysis and control of linear periodically time varying systems," Ph.D. dissertation, Massachusetts Institute of Technology, 1991. [Online]. Available: https://dspace.mit.edu/handle/1721.1/13761.

[46] N. M. Wereley and S. R. Hall, "Linear time periodic systems: Transfer function, poles, transmission zeroes and directional properties," *Proceedings of the American Control Conference*, vol. 2, pp. 1179–1184, 1991. DOI: 10.23919/acc.1991.4791563.

[47] D. M. Eggleston and F. Stoddard, *Wind Turbine Engineering Design*. New York: Springer US, Jan. 1987. [Online]. Available: https://www.osti.gov/biblio/5719832.

[48] F. N. Fritsch and R. E. Carlson, "Monotone Piecewise Cubic Interpolation," *SIAM Journal on Numerical Analysis*, vol. 17, no. 2, pp. 238–246, Apr. 1980. DOI: 10.1137/0717021. [Online]. Available: https://epubs.siam.org/terms-privacy%20http://epubs.siam.org/doi/10.1137/0717021.

[49] A. J. Laub, "Efficient multivariable frequency response computations," in *1980 19th IEEE Conference on Decision and Control including the Symposium on Adaptive Processes*, IEEE, Dec. 1980, pp. 39–41. DOI: 10.1109/CDC.1980.272015. [Online]. Available: http://ieeexplore.ieee.org/document/4046612/.

[50] J. C. Willems, "Feedback Systems," in *The Analysis of Feedback Systems*, The MIT Press, 1971. DOI: 10.7551/mitpress/1258.003.0005. [Online]. Available: https://direct.mit.edu/books/book/4801/chapter/219631.

[51] R. P. Coleman and A. M. Feingold, "Theory of mechanical oscillations of rotors with two hinged blades," National Advisory Committee for Aeronautics, Tech. Rep. NACA-TR-1351, Jan. 1958. [Online]. Available: https://ntrs.nasa.gov/citations/19930092339.

[52] H. Glauert, "Airplane Propellers," in *Aerodynamic Theory*, vol. IV, Berlin, Heidelberg: Springer Berlin Heidelberg, 1935, pp. 169–360. DOI: 10.1007/978-3-642-91487-4_3. [Online]. Available: http://link.springer.com/10.1007/978-3-642-91487-4_3.

A

Equations of motion of the analytical wind turbine model

A.1. Nonlinear equations of motion

The Lagrangian equations of motion are derived from the Lagrangian $L = T - V$, where T and V are the kinetic and potential energy of the system, respectively. First, the kinetic energy of the system is computed as [24]:

$$T = T_H = \sum_{j=1}^{B} \left(T_{U_j} + T_{D_j} \right) \tag{A.1}$$

where T_H is the kinetic energy of the hub, and T_{U_k} and T_{D_k} are the kinetic energy of fixed and movable parts of blade j. Besides, the contribution of all springs and the gravity to the potential energy is accounted as [24]:

$$V = V_{y_H} + V_{z_H} + \sum_{j=1}^{B} \left(V_{\beta_j} + V_{\zeta_j} + V_{U_j} + V_{D_j} \right) \tag{A.2}$$

where V_{z_H} and V_{y_H} are the potential energies of the tower fore-aft and side-side springs, V_β and V_ζ are the potential energies flapwise and edgewise springs, and the contribution of gravity of the fixed and the movable parts of the blades are V_U and V_D. The resulting analytical expression for the kinematic energy and the potential energy of the system can be found in Riva et al. [24].

The aerodynamic forces and moments on the blade hinges are computed based on a model developed by Eggleston and Stoddard [47], which corresponds to a linearised blade element momentum approach [24]. It considers constant aerodynamic properties along the blades. The model is extended to include the aerodynamic loads due to the tower motion. The aerodynamic forces and moments on the system consist of (a) the hub shear force in the fore-aft direction S_β^{aero}, (b) the hinge out-of-plane moment M_β^{aero}, (c) the hub shear force in the direction parallel to the chord of the blade and pointing towards the leading edge S_ζ^{aero}, and (d) the hinge moment in the edgewise direction M_ζ^{aero}. Similarly, the analytical expressions regarding the aerodynamic forces and moments be found in Riva et al. [24].

Finally, the Lagrangian equations of motion of the nonlinear model are computed with Wolfram Mathematica ®, and read [24]:

$$\begin{aligned} J_D\ddot{\beta} + C_\beta\dot{\beta} + K_\beta\beta = M_\beta^{\text{aero}} &- J_D(\Omega + \dot{\zeta})^2 \cos\beta \sin\beta - m_D r_{\text{GD}} \Big(g\cos(\psi + \zeta)\sin\beta + e\Omega^2 \cos\zeta \sin\beta \\ &- \ddot{y}_H \sin(\psi + \zeta)\sin\beta + \ddot{z}_H \cos\beta \Big) \end{aligned} \tag{A.3a}$$

$$J_D \cos^2\beta\ddot{\zeta} + C_\zeta\dot{\zeta} + K_\zeta\zeta = M_\zeta^{\text{aero}} + 2J_D(\Omega+\dot{\zeta})\dot{\beta}\cos\beta\sin\beta - m_D r_{\text{GD}}\cos\beta(g\sin(\psi+\zeta) + e\Omega^2\sin\zeta + \ddot{y}_H\cos(\psi+\zeta)), \tag{A.3b}$$

$$(m_{\text{H}} + B(m_U + m_D))\ddot{z}_H + C_z\dot{z}_H + K_z z_H = \sum_{j=1}^{B}\left(S_{\beta_j}^{\text{aero}} - m_D r_{\text{GD}}\left(\ddot{\beta}_j\cos\beta_j - \dot{\beta}_j^2\sin\beta\right)\right), \tag{A.3c}$$

$$(m_{\text{H}} + B(m_U + m_D))\ddot{y}_H + C_y\dot{y}_H + K_y y_H = \sum_{k=1}^{B}\left(S_{\zeta_j}^{\text{aero}}\cos(\psi_j+\zeta_j) + m_D r_{\text{GD}}\left(\Omega^2\cos\beta_j\sin(\psi_j+\zeta_j) + \dot{\beta}_j^2\cos\beta_j\sin(\psi_j+\zeta_j) + 2\dot{\beta}_j\dot{\zeta}_j\sin\beta_j\cos(\psi_j+\zeta_j) + \dot{\zeta}_j^2\cos\beta_j\sin(\psi_j+\zeta_j + 2\Omega(\dot{\beta}_j\sin\beta_j\cos(\psi_j+\zeta_j) + \dot{\zeta}_j\cos\beta_j\sin(\psi_j+\zeta_j)) + \ddot{\beta}_j\sin\beta_j\sin(\psi_j+\zeta_j) - \ddot{\zeta}_j\cos\beta_j\cos(\psi_j+\zeta_j)\right)\right) \tag{A.3d}$$

The second-order nonlinear model is obtained by reassembling the Lagrangian equations of motion of the simplified wind turbine model derived by Riva et al. [24]. The resulting nonlinear second-order implicit system can then be expressed as a system linear in $\ddot{\boldsymbol{\xi}}$ as:

$$\mathbf{M}_{NL}(\dot{\boldsymbol{\xi}}, \boldsymbol{\xi}, t)\,\ddot{\boldsymbol{\xi}} + \boldsymbol{f}_{NL}(\boldsymbol{\xi}, \dot{\boldsymbol{\xi}}, \boldsymbol{\nu}, t) = \mathbf{0} \tag{A.4}$$

where $\mathbf{M}_{NL}$ is the nonlinear mass matrix, $\boldsymbol{f}_{NL}$ is the nonlinear forcing vector, $\boldsymbol{\nu}$ are the system inputs, i.e, the hub-height axial wind speed, and the blade and tower coordinates are collected in the displacement vector as [24]:

$$\boldsymbol{\xi} = [\beta_1, \ldots, \beta_B, \zeta_1, \ldots, \zeta_B, y_H, z_H]^\top \tag{A.5}$$

where β and ζ are the flapwise and edgewise blade degrees of freedom, y_H and z_H are the tower side-side and fore-aft displacements, and $B = 3$ is the number of blades.

A.2. Linearised equations of motion

The linearised time-periodic equations of motion are derived by performing a multi-variable first-order Taylor series expansion of the nonlinear system about the periodic equilibrium trajectory $\tilde{\boldsymbol{\xi}}(t)$ with inputs $\tilde{\boldsymbol{\nu}}(t)$. The second-order linear model yields:

$$\mathbf{M}(t)\ddot{\mathbf{q}}(t) + \mathbf{C}(t)\dot{\mathbf{q}}(t) + \mathbf{K}(t)\mathbf{q}(t) + \mathbf{F}(t)\mathbf{u}(t) = \mathbf{0} \tag{A.6}$$

where the perturbations to the inputs and the states about the equilibrium are expressed as $\mathbf{u}(t) = \boldsymbol{\nu}(t) - \tilde{\boldsymbol{\nu}}(t)$ and $\mathbf{q}(t) = \boldsymbol{\xi}(t) - \tilde{\boldsymbol{\xi}}(t)$, respectively. Also, $\mathbf{M}$, $\mathbf{C}$, $\mathbf{K}$ and $\mathbf{F}$ are time-periodic linear mass, damping/gyroscopic, stiffness matrices and forcing vector, respectively. The system is a time-periodic system arising from the azimuthal rotation of the blades [43].

A.2.1. Multi-blade coordinate transformation

The linear time-periodic system can be transformed into multi-blade coordinates by means of the Coleman transformation matrix $\mathbf{B}_{\text{q}}$. To remove the periodic terms in the equations of motion, and thus obtain a linear time-invariant system, the simple wind turbine model is assumed be have an *isotropic* rotor with identically pitched blades ($\theta_{p,j} = \theta_p$) symmetrically mounted on the hub [43]. Also, the external (wind) conditions are also assumed to be isotropic. Hence, the gravity forcing, cross wind, and vertical wind shear terms are neglected.

The tower fore-aft and side-side motions are already described in the ground-fixed reference. The motion of the blades is, however, expressed in their own corotating frame [43]. The multi-blade coordinate transformation allows to transform the blade coordinate into the non-rotating frame as:

$$q_{n,j} = a_{n,0} + a_{n,1}\cos\psi_j + b_{n,1}\sin\psi_j \tag{A.7}$$

where n is the blade mode and the azimuth angle of blade j reads $\psi_j = \Omega t + \frac{2}{3}\pi(j-1)$. The multi-blade coordinates $a_{n,0}$, $a_{n,1}$, and $b_{n,1}$ describe the collective, cosine-cyclic, and sine-cyclic blade modes.

Then, the state vector can be transformed into MBCs as:

$$\mathbf{q} = \mathbf{B}_\mathrm{q}\mathbf{q}_\mathrm{B} \tag{A.8}$$

where the Coleman transformation matrix reads:

$$\mathbf{B}_\mathrm{q} = \begin{bmatrix} \mathbf{I}_B & \mathbf{I}_B\cos\psi_1 & \mathbf{I}_B\sin\psi_1 & \mathbf{0} \\ \mathbf{I}_B & \mathbf{I}_B\cos\psi_2 & \mathbf{I}_B\sin\psi_2 & \mathbf{0} \\ \mathbf{I}_B & \mathbf{I}_B\cos\psi_3 & \mathbf{I}_B\sin\psi_3 & \mathbf{0} \\ \mathbf{0} & \mathbf{0} & \mathbf{0} & \mathbf{I}_2 \end{bmatrix}. \tag{A.9}$$

The equations of the linear system expressed in the ground-fixed reference frame are derived by substituting the new state vector into the linearised EoM in Eq. (A.6). Under the assumption of an isotropic rotor in isotropic conditions, the resulting equations of motion are characterised by having constant matrices, and the system yields a linear time-invariant (LTI) system. The linear Coleman-transformed system reads:

$$\mathbf{M}_\mathrm{B}\ddot{\mathbf{q}}_\mathrm{B}(t) + \mathbf{C}_\mathrm{B}\dot{\mathbf{q}}_\mathrm{B}(t) + \mathbf{K}_\mathrm{B}\mathbf{q}_\mathrm{B}(t) + \mathbf{F}_\mathrm{B}\mathbf{u}_\mathrm{B}(t) = \mathbf{0} \tag{A.10}$$

where the Coleman-transformed mass, damping/gyroscopic, and stiffness matrices and force vector of the system are [43]:

$$\begin{aligned} \mathbf{M}_\mathrm{B} &= \mathbf{B}_\mathrm{q}^{-1}\mathbf{M}\mathbf{B}_\mathrm{q} \\ \mathbf{C}_\mathrm{B} &= \mathbf{B}_\mathrm{q}^{-1}(2\mathbf{M}\mathbf{B}_\mathrm{q}\mathbf{R} + \mathbf{C}\mathbf{B}_\mathrm{q}) \\ \mathbf{K}_\mathrm{B} &= \mathbf{B}_\mathrm{q}^{-1}(\mathbf{M}\mathbf{B}_\mathrm{q}\mathbf{R}^2 + \mathbf{C}\mathbf{B}_\mathrm{q}\mathbf{R} + \mathbf{K}\mathbf{B}_\mathrm{q}) \\ \mathbf{F}_\mathrm{B} &= \mathbf{B}_\mathrm{q}^{-1}\mathbf{F} \end{aligned} \tag{A.11}$$

where $\mathbf{R} = \mathbf{B}_\mathrm{q}^{-1}\dot{\mathbf{B}}_\mathrm{q}$, $\mathbf{B}_\mathrm{q}^{-1}$ being the inverse Coleman transformation matrix of the system.

Following, Eqs. (A.12) to (A.15) present the Coleman-transformed mass, damping/gyroscopic, and stiffness matrices, and the force vector of the analytical wind turbine model developed by Riva et al. [24],

where

m_H is the mass of the hub,

m_U and m_D is the mass of the fixed and the movable parts of the blade,

J_D is the blade moment of inertia,

$C_{(\cdot)}$ is the spring damping,

$K_{(\cdot)}$ is the spring stiffness,

e is the hinge offset,

θ_p is the pitch angle,

V_0, $V_{0,eq}$ is the axial wind speed,

v_i is the axial induced velocity,

γ is the Lock number,

R is the rotor radius, and

Ω is the rotor speed.

All the equations and matrices included in this derivation are computed analytically with Wolfram Mathematica®.

$$\mathbf{M}_{\mathrm{B}} = \begin{bmatrix} J_D & 0 & 0 & 0 & 0 & 0 & 0 & 0 \\ 0 & J_D & 0 & 0 & 0 & 0 & S_D & 0 \\ 0 & 0 & J_D & 0 & 0 & 0 & 0 & 0 \\ 0 & 0 & 0 & J_D & 0 & 0 & 0 & S_D \\ 0 & 0 & 0 & 0 & J_D & 0 & 0 & 0 \\ 3S_D & 0 & 0 & 0 & 0 & 0 & 3M_D + M_H + 3M_U & 0 \\ 0 & 0 & 0 & 0 & \frac{3S_D}{2} & 0 & 0 & 3M_D + M_H + 3M_U \end{bmatrix} \tag{A.12}$$

$$\mathbf{C}_{\mathrm{B}} = \begin{bmatrix} C_\beta + 1/8 J_D \gamma \Omega^3 & 0 & 0 & 0 \\ 0 & C_\beta + 1/8 J_D \gamma \Omega^3 & 2.J_D\Omega & 0 \\ 0 & -2J_D\Omega & C_\beta + 1/8 J_D \gamma \Omega^3 & 0 \\ J_D\gamma\Omega^2(8V_{0,eq} - 8v_i + 3R\theta_p\Omega)/(24R) & 0 & 0 & C_\zeta \\ 0 & J_D\gamma\Omega^2(8V_{0,eq} - 8v_i + 3R\theta_p\Omega)/(24R) & 0 & 0 \\ 0 & 0 & J_D\gamma\Omega^2(8V_{0,eq} - 8v_i + 3R\theta_p\Omega)/(24R) & 0 \\ J_D\gamma\Omega^3/(2R) & 0 & 0 & 0 \\ 0 & J_D\gamma\Omega^2(3V_{0,eq} - 3v_i + R\theta_p\Omega)/(4R^2) & 0 & 0 \end{bmatrix} \tag{A.13}$$

$$\begin{bmatrix} 0 & 0 & -J_D\gamma\Omega/(6R) & 0 \\ 0 & 0 & 0 & J_D\gamma(-3V_{0,eq} + 3v_i + 4R\theta_p\Omega)/(12R^2) \\ 0 & 0 & 0 & 0 \\ 0 & 0 & -J_D\gamma(3V_{0,eq} - 3v_i + R\theta_p\Omega)/(6R^2) & 0 \\ C_\zeta & 2J_D\Omega & 0 & J_D(-V_{0,eq} + v_i)\gamma\theta_p/(4R^2) \\ -2J_D\Omega & C_\zeta & 0 & 0 \\ 0 & 0 & C_z - 3J_D\gamma\Omega/(4R^2) & 0 \\ 0 & 0 & 0 & C_y + 3J_D(-V_{0,eq} + v_i)\gamma\theta_p/(4R^3) \end{bmatrix}$$

$$\mathbf{K}_{\mathrm{B}} = \begin{bmatrix} K_\beta + (J_D + eRS_D)\Omega^2 & 0 & 0 & 0 \\ 0 & K_\beta - J_D\Omega^2 + (J_D + eRS_D)\Omega^2 & C_\beta\Omega + 1/8 J_D\gamma\Omega^4 & 0 \\ 0 & -\Omega(8C_\beta + J_D\gamma\Omega^3)/8 & K_\beta - J_D\Omega^2 + (J_D + eRS_D)\Omega^2 & 0 \\ 0 & 0 & 0 & K_\zeta + eRS_D\Omega^2 \\ 0 & 0 & J_D\gamma\Omega^3(8V_{0,eq} - 8v_i + 3R\theta_p\Omega)/(24R) & 0 \\ 0 & -J_D\gamma\Omega^3(8V_{0,eq} - 8v_i + 3R\theta_p\Omega)/(24R) & 0 & 0 \\ 0 & 0 & 0 & 0 \\ 0 & 0 & J_D\gamma\Omega^3(3V_{0,eq} - 3v_i + R\theta_p\Omega)/(4R^2) & 0 \end{bmatrix} \tag{A.14}$$

$$\begin{bmatrix} 0 & 0 & 0 & 0 \\ 0 & 0 & 0 & 0 \\ 0 & 0 & 0 & 0 \\ 0 & 0 & 0 & 0 \\ K_\zeta - J_D\Omega^2 + eRS_D\Omega^2 & C_\zeta\Omega & 0 & 0 \\ -C_\zeta\Omega & K_\zeta - J_D\Omega^2 + eRS_D\Omega^2 & 0 & 0 \\ 0 & 0 & K_y & 0 \\ 0 & 3J_D(V_{0,eq} - v_i)\gamma(2V_{0,eq} - 2v_i + R\theta_p\Omega)/(8R^3) & 0 & K_y \end{bmatrix}$$

$$\mathbf{F}_{\mathrm{B}} = \begin{bmatrix} -J_D\gamma\Omega/(6R) \\ 0 \\ 0 \\ -J_D\gamma(3V_{0,eq} - 3v_i + R\theta_p\Omega)/(6R^2) \\ 0 \\ 0 \\ -3J_D\gamma\Omega/(4R^2) \\ 0 \end{bmatrix} \tag{A.15}$$

B

Linearised BHawC model: equations of motion in the inertial frame

The equations of motion in global coordinates of a wind turbine dynamic system linearised about a periodic steady state are expressed as:

$$\mathbf{M}(t)\ddot{\mathbf{q}} + \mathbf{C}(t)\dot{\mathbf{q}} + \mathbf{K}(t)\mathbf{q} = \mathbf{F}(t)\mathbf{u} \tag{B.1}$$

where $\mathbf{q}$ is the vector of the system positions and orientations described in the global frame, $\mathbf{u}$ is the system input, $\mathbf{F}$ is the external forcing vector, and $\mathbf{M}$, $\mathbf{C}$, and $\mathbf{K}$ are the T-periodic tangent system mass, damping and stiffness matrices, respectively, which are composed by the structural matrices and the steady aerodynamic matrices as

$$\mathbf{M} = \mathbf{M}_\mathrm{s} + \mathbf{M}_\mathrm{a}, \quad \mathbf{C} = \mathbf{C}_\mathrm{s} + \mathbf{C}_\mathrm{a}, \quad \mathbf{K} = \mathbf{K}_\mathrm{s} + \mathbf{K}_\mathrm{a} \tag{B.2}$$

where the subscripts 's' and 'a' denote the structural and aerodynamic matrices, respectively.

The Coleman transformation approach is used to get the equations of motion expressed in the inertial frame. However, to apply the Coleman transformation matrix, the degrees of freedom on each blade must be identical [32]. Thus, the transformation is split into two steps: (1) transforming the global coordinates into the substructure frame and (2) transforming the substructure coordinates into the inertial frame.

B.1. Transformation into substructure coordinates

The equations of motion in the global frame in Eq. (B.1) are first transformed into substructure coordinates $\mathbf{q}_\mathrm{T}$ as

$$\mathbf{q} = \mathbf{T}\mathbf{q}_\mathrm{T} \tag{B.3a}$$
$$\dot{\mathbf{q}} = \dot{\mathbf{T}}\mathbf{q}_\mathrm{T} + \mathbf{T}\dot{\mathbf{q}}_\mathrm{T} \tag{B.3b}$$
$$\ddot{\mathbf{q}} = \ddot{\mathbf{T}}\mathbf{q}_\mathrm{T} + 2\dot{\mathbf{T}}\dot{\mathbf{q}} + \mathbf{T}\ddot{\mathbf{q}}_\mathrm{T} \tag{B.3c}$$

where $\mathbf{T}$ is a T-periodic block diagonal matrix which includes the identity matrix $\mathbf{I}_{N_\mathrm{s}}$ sized by the number of degrees of freedom of the tower, nacelle, and drivetrain, $\mathbf{T}_\mathrm{r}$ transforming the degrees of freedom on the shaft and hub into a hub centre frame, and $\mathbf{T}_{\mathrm{b}j}$ transforming the degrees of freedom on blade

number $j = 1, 2, 3$ into a local frame for blade j [32]:

$$\mathbf{T} = \mathbf{diag}\left(\mathbf{I}_{N_s}, \mathbf{T}_{\mathrm{r}}, \mathbf{T}_{\mathrm{b}1}, \mathbf{T}_{\mathrm{b}2}, \mathbf{T}_{\mathrm{b}3}\right) . \tag{B.4}$$

Substituting the transformation in Eq. (B.3) into Eq. (B.1), and pre-multiplying by $\mathbf{T}^\top$, the equations of motion in substructure coordinates read

$$\mathbf{M}_{\mathrm{T}}\,\ddot{\mathbf{q}}_{\mathrm{T}} + \mathbf{C}_{\mathrm{T}}\,\dot{\mathbf{q}}_{\mathrm{T}} + \mathbf{K}_{\mathrm{T}}\,\mathbf{q}_{\mathrm{T}} = \mathbf{F}_{\mathrm{T}}\,\mathbf{u} \tag{B.5}$$

where the substructure transformed mass, damping/gyroscopic, and stiffness matrices are, respectively,

$$\mathbf{M}_{\mathrm{T}} = \mathbf{T}^\top\mathbf{M}\mathbf{T} \tag{B.6a}$$
$$\mathbf{C}_{\mathrm{T}} = \mathbf{T}^\top(\mathbf{C}\mathbf{T} + 2\mathbf{M}\dot{\mathbf{T}}) \tag{B.6b}$$
$$\mathbf{K}_{\mathrm{T}} = \mathbf{T}^\top(\mathbf{K}\mathbf{T} + \mathbf{C}\dot{\mathbf{T}} + \mathbf{M}\ddot{\mathbf{T}}) \tag{B.6c}$$
$$\mathbf{F}_{\mathrm{T}} = \mathbf{T}^\top\mathbf{F}\,. \tag{B.6d}$$

B.2. Transformation into the inertial frame

The system can be then transformed into the inertial frame, in which the coordinate vector is composed of the untransformed coordinates for tower, nacelle, and drivetrain $\mathbf{q}_{\mathrm{s}}$, the coordinates for shaft and hub $\boldsymbol{\zeta}_{\mathrm{r}}$ measured in a non-rotating frame aligned with the hub, and the multi-blade symmetric coordinates $\mathbf{a}_0$, cosine coordinates $\mathbf{a}_1$, and sine coordinates $\mathbf{b}_1$:

$$\boldsymbol{\zeta} = \left[\mathbf{q}_{\mathrm{s}}^\top\ \boldsymbol{\zeta}_{\mathrm{r}}^\top\ \mathbf{a}_0^\top\ \mathbf{a}_1^\top\ \mathbf{b}_1^\top\right]^\top \tag{B.7}$$

For simplicity, the inertial frame velocities are related to the coordinates vector and its derivatives as $\tilde{\boldsymbol{\zeta}} = \dot{\boldsymbol{\zeta}} + \bar{\boldsymbol{\omega}}\boldsymbol{\zeta}$, where $\bar{\boldsymbol{\omega}} = \mathbf{B}_{\mathrm{q}}^{-1}\,\dot{\mathbf{B}}_{\mathrm{q}}$ is a constant matrix relating the Coleman transformation matrix and its derivative. The transformation reads

$$\mathbf{q}_{\mathrm{T}} = \mathbf{B}_{\mathrm{q}}\boldsymbol{\zeta} \tag{B.8a}$$
$$\dot{\mathbf{q}}_{\mathrm{T}} = \dot{\mathbf{B}}_{\mathrm{q}}\boldsymbol{\zeta} + \mathbf{B}_{\mathrm{q}}\dot{\boldsymbol{\zeta}} = \mathbf{B}_{\mathrm{q}}\tilde{\boldsymbol{\zeta}} \tag{B.8b}$$
$$\ddot{\mathbf{q}}_{\mathrm{T}} = \ddot{\mathbf{B}}_{\mathrm{q}}\boldsymbol{\zeta} + 2\dot{\mathbf{B}}_{\mathrm{q}}\dot{\boldsymbol{\zeta}} + \mathbf{B}\ddot{\boldsymbol{\zeta}} = \mathbf{B}_{\mathrm{q}}(\dot{\tilde{\boldsymbol{\zeta}}} + \bar{\boldsymbol{\omega}}\tilde{\boldsymbol{\zeta}}) \tag{B.8c}$$

where the time-variant transformation matrix is a block diagonal matrix composed of the identity matrix $\mathbf{I}_{N_s}$, the simple rotational transformation matrix for the shaft and hub $\mathbf{B}_{\mathrm{r}}$, and the Coleman transformation $\mathbf{B}_{\mathrm{b}}$ for the blades, which introduces the multi-blade coordinates:

$$\mathbf{B}_{\mathrm{q}} = \mathbf{diag}\left(\mathbf{I}_{N_s}, \mathbf{B}_{\mathrm{r}}, \mathbf{B}_{\mathrm{b}}\right) \tag{B.9}$$

By substituting the transformation in Eq. (B.8) into Eq. (B.6), and also pre-multiplying by $\mathbf{B}_{\mathrm{q}}^{-1}$, the equations of motion in inertial coordinates read

$$\mathbf{B}_{\mathrm{q}}^{-1}\mathbf{M}_{\mathrm{T}}\mathbf{B}_{\mathrm{q}}\,\dot{\tilde{\boldsymbol{\zeta}}} + \mathbf{B}_{\mathrm{q}}^{-1}\left(\mathbf{C}_{\mathrm{T}}\mathbf{B}_{\mathrm{q}} + \mathbf{M}_{\mathrm{T}}\mathbf{B}_{\mathrm{q}}\bar{\boldsymbol{\omega}}\right)\tilde{\boldsymbol{\zeta}} + \mathbf{B}_{\mathrm{q}}^{-1}\mathbf{K}_{\mathrm{T}}\mathbf{B}_{\mathrm{q}}\,\boldsymbol{\zeta} = \mathbf{B}_{\mathrm{q}}^{-1}\mathbf{F}_{\mathrm{T}}\mathbf{u}_{\mathrm{B}} \tag{B.10}$$

or

$$\mathbf{M}_{\mathrm{B}}\,\dot{\tilde{\boldsymbol{\zeta}}} + (\mathbf{C}_{\mathrm{B}} + \mathbf{M}_{\mathrm{B}}\bar{\boldsymbol{\omega}})\,\tilde{\boldsymbol{\zeta}} + \mathbf{K}_{\mathrm{B}}\,\boldsymbol{\zeta} = \mathbf{F}_{\mathrm{B}}\mathbf{u}_{\mathrm{B}} \tag{B.11}$$

where the Coleman transformed mass, damping/gyroscopic, and stiffness matrices are, respectively,

$$\mathbf{M}_\mathrm{B} = \mathbf{B}_\mathrm{q}^{-1}\mathbf{T}^\top\mathbf{M}\mathbf{T}\mathbf{B}_\mathrm{q} \tag{B.12a}$$

$$\mathbf{C}_\mathrm{B} = \mathbf{B}_\mathrm{q}^{-1}\mathbf{T}^\top(\mathbf{C}\mathbf{T} + 2\mathbf{M}\dot{\mathbf{T}})\mathbf{B}_\mathrm{q} \tag{B.12b}$$

$$\mathbf{K}_\mathrm{B} = \mathbf{B}_\mathrm{q}^{-1}\mathbf{T}^\top(\mathbf{K}\mathbf{T} + \mathbf{C}\dot{\mathbf{T}} + \mathbf{M}\ddot{\mathbf{T}})\mathbf{B}_\mathrm{q} \tag{B.12c}$$

$$\mathbf{F}_\mathrm{B} = \mathbf{B}_\mathrm{q}^{-1}\mathbf{T}^\top\mathbf{F}\,. \tag{B.12d}$$

C

Validation of the state-space model

Two cases have been analysed to evaluate the validity of the implemented state-space system and its corresponding system, input, output, and feedforward matrices, **A**, **B**, **C**, and **D**, respectively. First, Appendix C.1 explains the validation of the input matrix by means of a finite difference approach. Second, Appendix C.2.1 presents the time-domain response of the loads to a ramping force input to validate the system matrix as well as the output matrix. Both the rotor and the external conditions are assumed to be isotropic; thus, the system is modelled as a linear time-invariant (LTI) system.

C.1. Finite difference checks

Finite difference checks have been done to ensure that the analytically-derived partial derivatives of the linear model are calculated properly. Thereby, the validity of the input matrix **B** in the state-space model is checked. The finite difference checks work as follows: the difference in a variable from the linear model is computed using a first-order finite-difference approximation. The values are then compared to the differences in the variable between two operating points in a BHawC simulation. For instance, a simulation is run at three neighbouring operating points (OPs), i.e. at wind speeds of 9.999, 10, and 10.001 m/s. Moreover, selecting as a variable the relative wind speed at the aerodynamic sections, the finite differences are obtained as:

$$\Delta \mathbf{W}_{\mathrm{A}}^{A} = \frac{\partial \mathbf{W}_{\mathrm{A}}^{A}}{\partial \mathbf{V}_{0}^{G}} \cdot \Delta \mathbf{V}_{0}^{G} = \mathbf{T}_{\mathrm{A}}\, \Delta \mathbf{V}_{0}^{G} \quad \text{for the linear model, and} \tag{C.1a}$$

$$\Delta \mathbf{W}_{\mathrm{A}}^{A} = \mathbf{W}_{\mathrm{A}}^{A}(\mathrm{OP}_{i+1}) - \mathbf{W}_{\mathrm{A}}^{A}(\mathrm{OP}_{i}) \quad \text{for the BHawC results.} \tag{C.1b}$$

The example above uses a forward differencing scheme. Thus, $\Delta \mathbf{V}_{0}^{G}$ represents the variation in free wind speed between operating points $i+1$ and i. This methodology can also be used using backward and central differencing schemes. Then, the deviation between the values in Eq. (C.1a) and Eq. (C.1b) is computed.

Following the same approach, the difference in aerodynamic loads (forces and moments) at each aerodynamic calculation point $\mathbf{f}_{\mathrm{A,aero}}^{A}$ can be computed, and, similarly for the aerodynamic loads at the structural nodes in the global frame of reference $\mathbf{f}_{\mathrm{E,aero}}^{G}$. Fig. C.1 displays the standard deviation of the difference in aerodynamic loads between the linear model and the results from BHawC as a function of the step in wind speed between operating points. The wind speed step between the OPs ranges from 10^{-9}m/s to 10^{-4}m/s.

The aerodynamic loads on the structural nodes in the global frame come from integrating the aerodynamic loads in the local aerodynamic frame and mapping them to the global coordinate system. Hence,

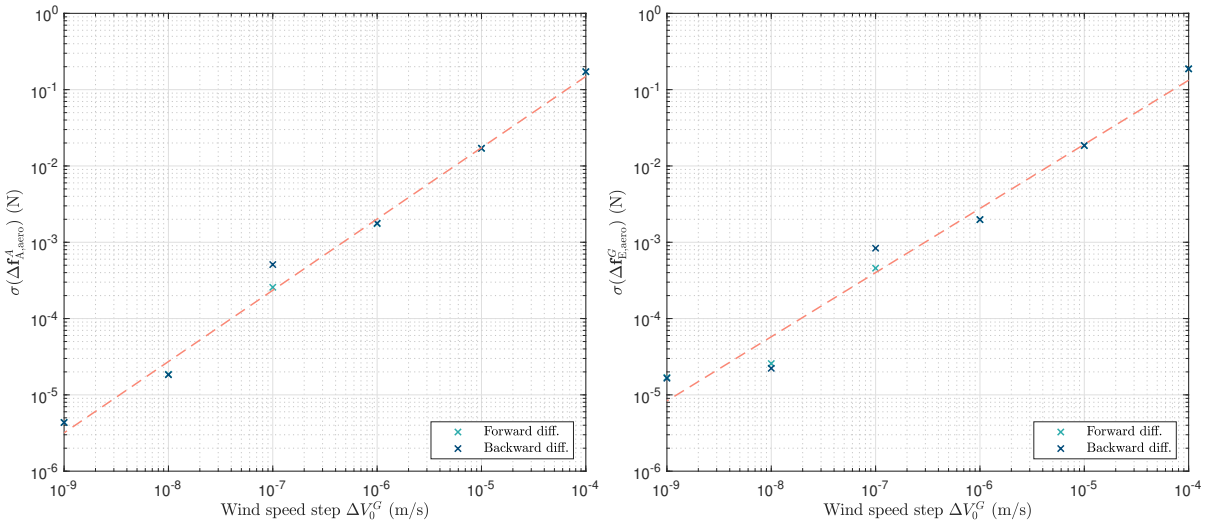

(a) SD of loads at the aerodynamic calculation points

(b) SD of loads at the global structural nodes

Figure C.1: Finite difference check: standard deviation of the difference in aerodynamic loads

the difference in aerodynamic loads is higher for the loads on the structural nodes $\mathbf{f}^G_{\mathrm{E,aero}}$. Moreover, the higher the step in wind speed, the larger the variation in the operating point, and the less accurate the linearised model. Hence, as expected, the standard deviation of the loads increases with the step in wind speed. Besides, both differencing methods —the forward and backward schemes— yield similar results.

C.2. Numerical results

This section is focused on presenting the dynamic response of the linear system subject to a ramping force input applied at the tower-top node. This allows to validate the output matrix of the state-space model.

C.2.1. Ramping force at the tower-top

The dynamic response of the wind turbine system using the linear state-space model is used to check the validity of the system matrix defined in Eq. (4.9a), as well as the output matrix in Eq. (4.24). Given that the system is assumed to be in isotropic conditions, the time-invariant mass, damping, and stiffness matrices are extracted from BHawC at a single azimuth angle.

On the other hand, an external force vector is applied at the tower-top node. The load is assumed to increase uniformly from 0 N until 10^4 N over the time interval from 10 s to 30 s. Outside this interval, the values are kept constant. The simulation time is 120 s, with a mean hub-height wind speed 27 m/s. The comparison is made for two loading scenarios: applying the external force in the lateral (x_G) and the longitudinal (y_G) directions. Both the tower-top node displacements and the tower-bottom loads of the linear model are analysed and compared against the simulation results from BHawC.

Displacements

The two loading cases are presented in Figs. C.2 to C.3, where the displacements and rotations of the tower-top node resulting from the time simulations of the linear model are shown and compared against time simulations from BHawC. Recall that the nodal displacements consist of three translational degrees of freedom, ξ_x, ξ_y, and ξ_z, respectively, as well as three rotational degrees of freedom denoted by θ_x, θ_y, and θ_z, respectively. Overall, the linear system captures the dynamics of the nonlinear model, and it computes the initial steady-state value of the system correctly.

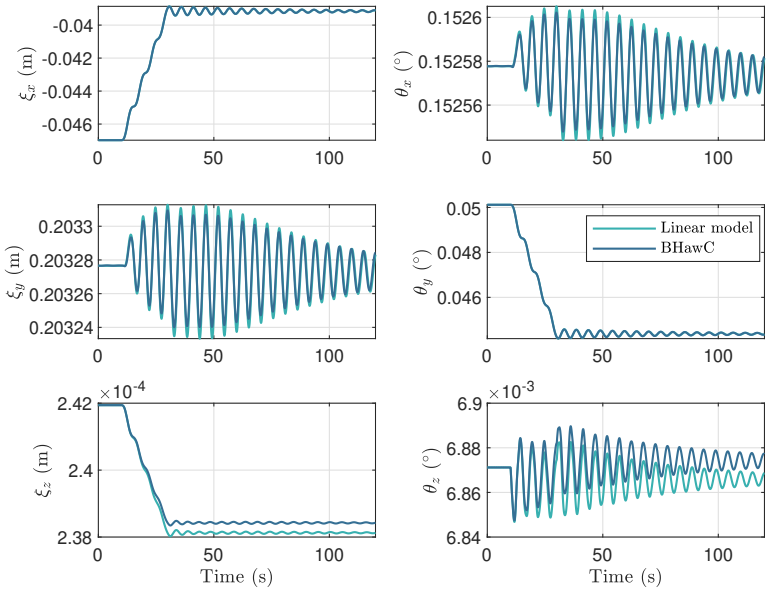

Figure C.2: Response of tower-top displacements under an external ramping force applied in the lateral direction. Comparison between the linear model and BHawC

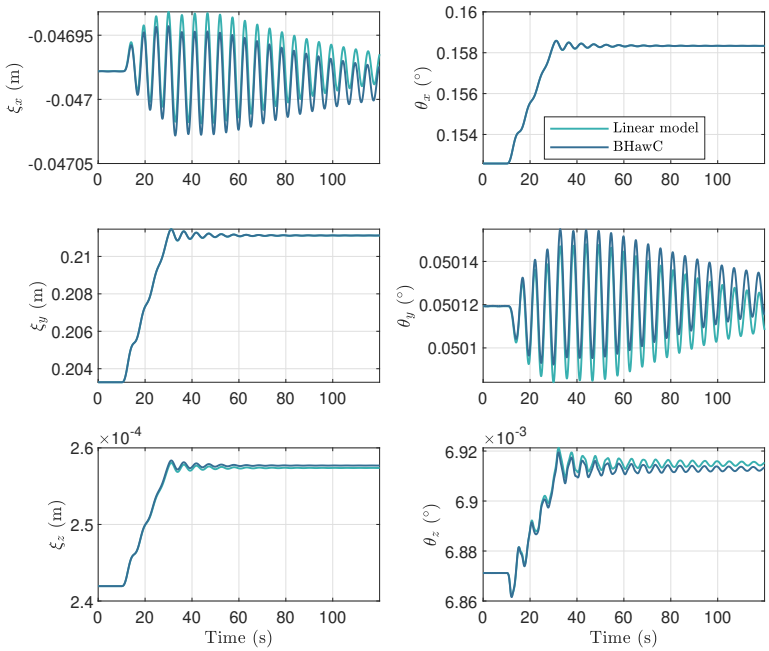

Figure C.3: Response of tower-top displacements under an external ramping force applied in the longitudinal direction. Comparison between the linear model and BHawC

Before applying the external force, the initial steady-state value of the linear model can be seen, which fully matches that of the BHawC results. Imposing the load on the tower-top node causes the node degrees of freedom to vary. As expected, if the load is applied in the lateral (x_G) direction, the motion is driven by the side-side displacement ξ_x, coupled to θ_y. Contrarily, if it is applied along the longitudinal (y_G) direction, the tower-top is dominated by the fore-aft displacement ξ_y, coupled to θ_x. The smallest displacement is the vertical translation ξ_z for both study cases. Then, once the maximum load of 10 kN is reached, the system remains excited by the final loading value. The structural and aerodynamic dampings cause the oscillations to dampen, and eventually, a new steady state is reached. In general, the linearised BHawC model is in good agreement with the nonlinear BHawC code. However, a slight difference in the amplitude of the oscillations is present, and the final steady-state of some degrees of

freedom differs to some degree.

On the other hand, the statistics between the response of the linear model and the BHawC time simulation are compared through the root-mean-square error (RMSE) normalised with the range (maximum value minus minimum value) in the response. In general, both responses show good agreement with RMSEs under 5%. For the case where the force is applied along the lateral direction (x_G-axis), the highest differences belong to the vertical translation ξ_z and the rotation about the z_G-axis θ_z, respectively. For the case where the force is imparted in the longitudinal direction (y_G-axis), the DOF with the highest variation amongst models is again the vertical translation ξ_z.

Internal loads

The dynamic response of the internal loads of the linear model is compared to the BHawC time simulation to check the validity of the state-space model's output matrix **C**. The vector of internal loads consists of three forces and three moments. The forces correspond to the internal forces in the lateral, longitudinal, and vertical directions, f_x, f_y and f_z, respectively. The moments are the fore-aft, side-side, and torsional moments, m_x, m_y and m_z, respectively. The loads are normalised with the dominant loads. Specifically, the tower-base forces are normalised with the longitudinal force f_y and the moments with the fore-aft moment m_x.

Again, the external force considered is a ramping force applied at the tower-top node during the time interval from 10 s to 30 s and remains constant at 10 kN after this interval. Figs. C.4 to C.5 displays the loads at the tower bottom for a wind turbine subject to the external ramping force mentioned above. Similarly, the initial steady-state can be seen, as well as the load variation during the period in which the ramping force is applied. Once the external force is kept constant at its maximum value, the oscillations dampen out toward the final steady-state value. Fig. C.4 shows the tower-base loads for the case where the force is applied in the lateral direction (x_G). As seen, the moment that varies the most throughout the simulation is the side-side bending moment m_y. That is an expected behaviour as it is coupled to the force in the lateral direction f_x. Moreover, Fig. C.5 illustrated the loads at the tower-bottom for the scenario in which the force is applied in the longitudinal direction (y_G). Here, as expected, the force that varies most is the longitudinal force f_y, which is coupled to the fore-aft moment m_x. Although presenting some variations in the amplitudes of the oscillation, the responses of the linear model show a good agreement to the BHawC nonlinear code.

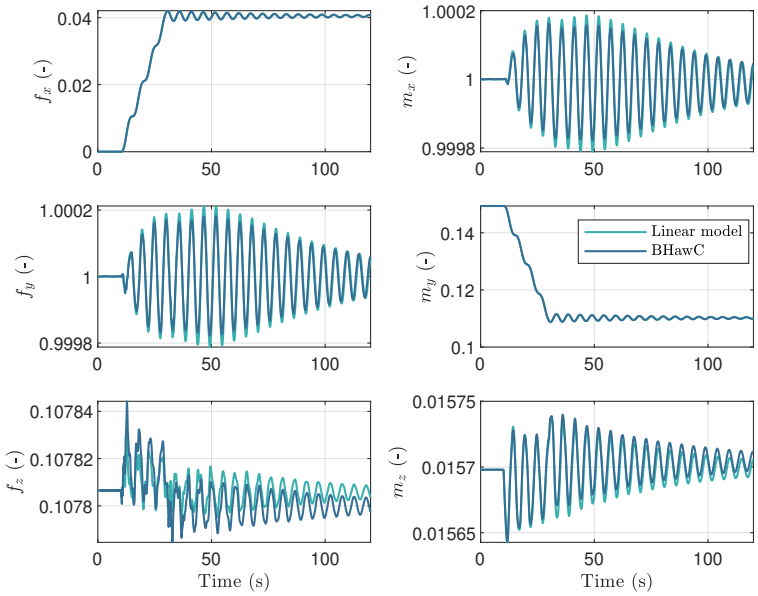

Figure C.4: Response of tower-bottom loads under an external ramping force applied in the lateral direction. Comparison between the linear model and BHawC

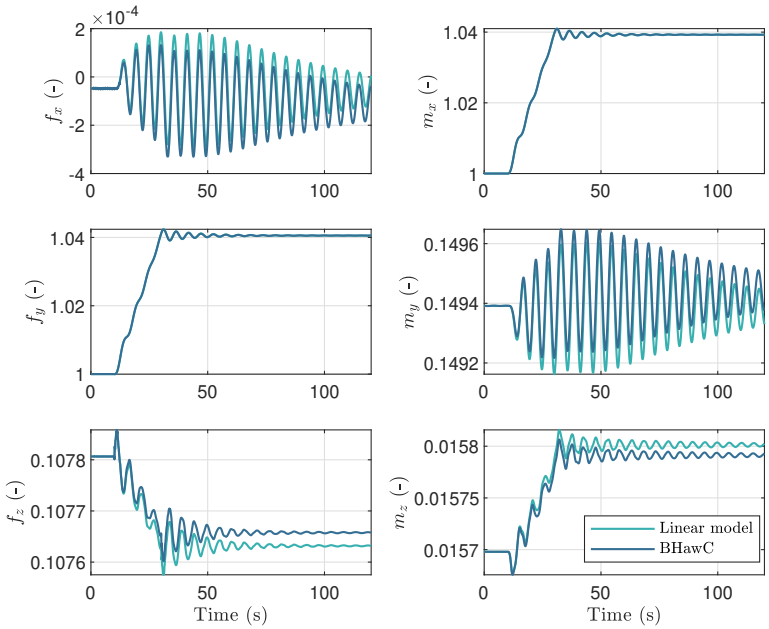

Figure C.5: Response of tower-bottom loads under an external ramping force applied in the longitudinal direction. Comparison between the linear model and BHawC

Furthermore, a static analysis is used to verify the results in the simulations. That is, the difference in the imposed ramped external load at the tower-top node is used to get the variation in the displacements of the wind turbine system. For all cases, the results are in good agreement.

D

Response to a wind step: tower-top displacements

This appendix focuses on comparing the dynamic response of the linear model and the BHawC code when subject to a step in wind speed. The analysis uses the same cases as those in Section 5.4.2, but instead, it studies the tower-top displacements of the turbine. Accordingly, the linear model is assembled at each operating point and transformed into a linear time-invariant (LTI) system. Thence, the rotor and external conditions are assumed to be isotropic. The wind input to the system is a rectangular step of 0.1 m/s. The step acts 10 s after the simulation start and has a duration of 1 s, after which it steps back to its original value. The wind inflow is considered to be aligned with the rotor axial direction. Considering the wind input mentioned above, the system is simulated at three working points: 5 m/s (low wind speed), 10 m/s (mid wind speed), and 27 m/s (high wind speed). Figs. D.1 to D.3 contain the tower-top displacements of the simulations of the linearised BHawC model compared to the dynamic behaviour of the BHawC nonlinear code.

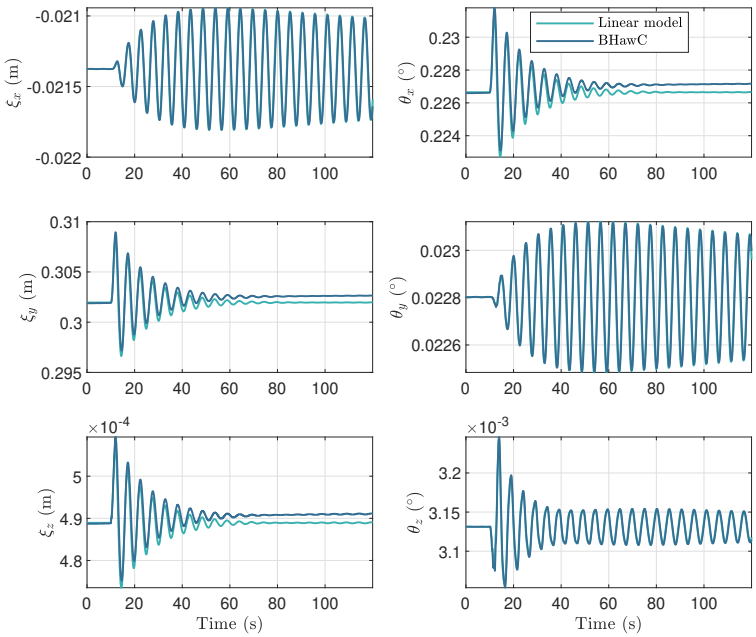

Figure D.1: Response of the tower-top displacements under a rectangular wind step at 5 m/s hub-height wind speed. Comparison between the linear model and BHawC

Initially, the steady-state value of the linear model response is seen to match that of the BHawC. Then,

ten seconds into the simulation, the wind turbine is excited with the step in the wind. As consequence, the degrees of freedom begin to oscillate about the steady-state solution. One second later, the wind turbine is no longer excited, and the responses of the displacements begin to decay due to the structural and the aerodynamic dampings. Eventually, the displacements return to their steady-state value. Overall, the response linearised model is in good agreement with the time series of the nonlinear system. Therefore, it is capable of capturing dynamic behaviour of the wind turbine in the vicinity of each operating point. At low wind speeds, however, the final steady-state value of some DOFs of the linear model slightly differs from that in the BHawC simulations (see Fig. D.1).

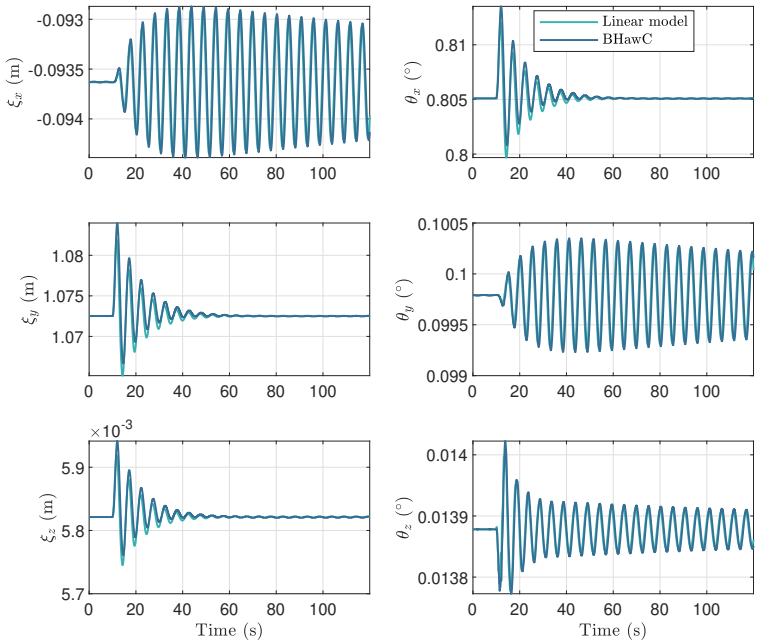

Figure D.2: Response of the tower-top displacements under a rectangular wind step at 10 m/s hub-height wind speed. Comparison between the linear model and BHawC

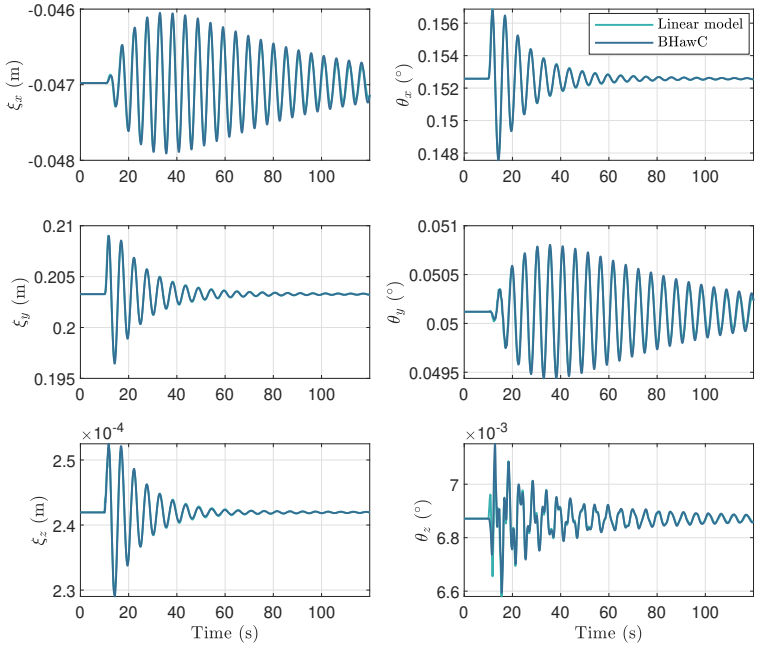

Figure D.3: Response of the tower-top displacements under a rectangular wind step at 27 m/s hub-height wind speed. Comparison between the linear model and BHawC

Besides, as seen in Figs. D.1 to D.3, the motion is dominated by the fore-aft displacements ξ_y, which is coupled to θ_x, the rotation about the x_G-axis. This is due to the wind being applied along the rotor axis. As expected, the translation in the vertical direction ξ_z and the torsional rotation θ_z are the smallest displacements. Finally, at low wind speeds, i.e., Fig. D.1, the aerodynamic loads exerted on the system are lower to those at mid wind speeds, for instance Fig. D.2. Therefore, the displacements are lower. For high wind speed, for example the case in Fig. D.3, where the wind speed is well above rated conditions, the blades are pitched to maintain the same torque while not causing any structural damage on the turbine. Consequently, the aerodynamic loads on the system are lower to those in the mid-speed range, and so are the deflections of the tower-top node.

Finally, the statistics of the response of the three study cases are checked using the root-mean-square error (RMSE) normalised with the range (maximum minus minimum) of the response. For all cases, the difference is highest for the lateral displacement and the side-side rotation. For the simulation at 5 m/s, the normalised RMSE is of 4% for all degrees of freedom, and 12% for the DOFs related to the tower side-side motion. For the 10 m/s case, the RMSE is under 6% for all displacements. Last, for the simulation using a 27 m/s wind inflow, the error of the tower-top displacements is around 1%, except for the side-side motion DOFs, where it is approximately 3%.